INFORMATION TO USERS

This manuscript has been reproduced from the microfilm master. UMI films the text directly from the original or copy submitted. Thus, some thesis and dissertation copies are in typewriter face, while others may be from any type of computer printer.

The quality of this reproduction is dependent upon the quality of the copy submitted. Broken or indistinct print, colored or poor quality illustrations and photographs, print bleedthrough, substandard margins, and improper alignment can adversely affect reproduction.

In the unlikely event that the author did not send UMI a complete manuscript and there are missing pages, these will be noted. Also, if unauthorized copyright material had to be removed, a note will indicate the deletion.

Oversize materials (e.g., maps, drawings, charts) are reproduced by sectioning the original, beginning at the upper left-hand corner and continuing from left to right in equal sections with small overlaps. Each original is also photographed in one exposure and is included in reduced form at the back of the book.

Photographs included in the original manuscript have been reproduced xerographically in this copy. Higher quality 6" x 9" black and white photographic prints are available for any photographs or illustrations appearing in this copy for an additional charge. Contact UMI directly to order.

UMI

A Bell & Howell Information Company
300 North Zeeb Road, Ann Arbor MI 48106-1346 USA
313/761-4700 800/521-0600

THE UNIVERSITY OF OKLAHOMA

GRADUATE COLLEGE

THREE-DIMENSIONAL FINITE ELEMENT MODELING OF TWO-PHASE FLUID FLOW IN DEFORMABLE NATURALLY FRACTURED RESERVOIRS

A DISSERTATION

SUBMITTED TO THE GRADUATE FACULTY

in partial fulfillment of the requirements for the

degree of

DOCTOR OF PHILOSOPHY

By

FANHONG MENG

Norman, Oklahoma

1998

THREE-DIMENSIONAL FINITE ELEMENT MODELING OF TWO-PHASE FLUID FLOW IN DEFORMABLE NATURALLY FRACTURED RESERVOIRS

A DISSERTATION APPROVED

FOR THE SCHOOL OF PETROLEUM AND GEOLOGICAL

ENGINEERING

BY

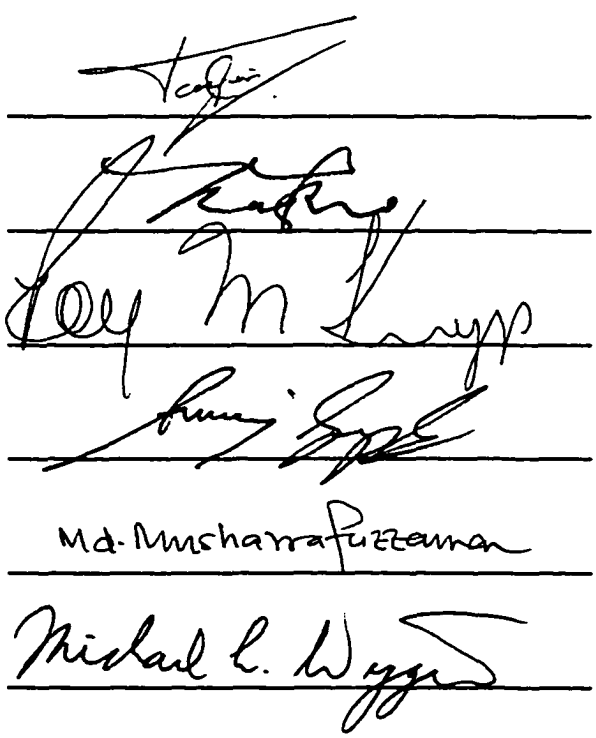

Dedicated to my family and friends ...

Acknowledgments

A dissertation is never the work of a lonely hunter. In my case, I have been so blessed with the support, collaboration and encouragement from so many special people.

My wholehearted thanks first go to my advisor, Dr. Jean-Claude Roegiers. His academic advice, guidance, encouragement, financial support, and close reading of innumerable drafts of the dissertation have been invaluable. Furthermore, his enthusiasm and devotion to rock mechanics, his scientific rigor, and his commitment to excellence have constantly led me to strive for the best. I have to say he is the best advisor I have ever had and can ever expect to have.

I deeply appreciate Dr. Mao Bai for his help, guidance, and suggestions in conducting the research work for this dissertation. My gratitude also goes to Dr. Musharraf Zaman for his professional and technical help in my research work. Innumerable research meetings and countless discussions also led 22 journal/conference papers or technical reports. Moreover, they read my research papers and my dissertation with excruciating scrutiny and helped me to clear any conceptual confusion and avoid even typo errors.

I also thank other members of my advisory committee, Dr. Anuj Gupta, Dr. Michael Wiggins and Dr. Roy Knapp, for their advice and help. It is from them

that I learned several subjects in petroleum engineering which I had lacked but which were essential for my dissertation and future career.

I also want to give my thanks to all my groupmates, especially Dr. Huaxing Zhang, Dr. Mazen Kanj, Dr. Mian Chen, Mauro Bloch and Zhengying Shu, for so many intellectual, interesting and personal exchanges from which I learned so much.

My appreciation goes to the help of all the members of the Rock Mechanics Institute at The University of Oklahoma with special thanks to Ms. Carla Cates, Mr. Don Cruickshank, Dr. Thurman E. Scott, Dr. Younane Abousleiman and Ms. Leslie Flenniken. I am very grateful to them for keeping RMI such a pleasant work environment and for making these years such a constructive and wonderful experience for me.

My profound gratitude goes to my family for sharing each bit of trouble and happiness in my life. The understanding, encouragement and support always came from my mother and father. I want to thank my brother for taking part of my responsibility to take care of our parents and comfort them when they needed it most. Actually as a doctor and researcher working in the medical school of the University of Washington, he may contribute more to our society for his studies on AIDS and cancer. The support and love from my family have been a main inspiration for me to accomplish the research work at The University of Oklahoma. This dissertation is dedicated to them.

Contents

List of Figures

List of Tables

Abstract

In many engineering problems, such as those in petroleum and geotechnical engineering, reservoir rocks have to be modeled as porous materials saturated with fluids. In order to accurately predict the behaviors of the reservoir and fluid flow, the solid-phase deformations and fluid-phase flow must be fully-coupled in the numerical calculation. Understanding and quantifying two-phase flow in fractured porous media is important for mathematical modeling and numerical simulation of petroleum reservoirs, geothermal reservoirs, coal-beds exploited for methane and nuclear waste repositories. Both the need for abundant energy and the demand for a clean environment have motivated many studies of two-phase flow in fractured reservoirs. In this dissertation, a mathematical model for two-phase fluid flow in a deforming fractured reservoir has been developed.

The naturally fractured reservoir is treated as a double-porosity medium consisting of the primary rock matrix system, which contains large amount of fluids but has lower permeability, and the fracture system which represents a small volume of fluid but due to its higher permeability transmits a large portion of fluid through the porous media. For the two-phase fluids, not only do both fluids flow through the rock matrix and the fractures, but also the effects of the capillary pressures, saturations and the variation of relative permeability need to be taken into account.

The numerical model is based on the rigorous conservation equations of momentum and mass, in which the solid deformations of the fractured porous media are lumped while the fluid pressures of the wetting and non-wetting phases are evaluated separately but linked through mass interchange terms for the two interactive media, i.e., matrix and fractures. The mathematical formulation describes a fully coupled governing equation system which consists of the equilibrium equations for the rock deformations and the continuity equations for two immiscible fluids flowing in a fractured porous medium.

Following the theoretical work is the construction of the numerical schemes. The numerous unknowns are resolved through the finite element technique, which enables the solutions to be obtained in the general three-dimensional space domains and integration in time domains. In this model, material properties are represented by the defined eight-node block elements, which form a mesh that is discretized by the user to fit the shape of the object to be modeled. This non-linear system of equations in the finite element model is solved using the direct iteration method, in which each iteration is controlled by the error analyses of the unknowns. And the elements of the coefficient matrices of the highly non-linear system are updated during each iteration in terms of the independent variables.

The developed theoretical formulation and numerical model are validated against several cases where the analytical solutions or other model results are readily available. The performance of the numerical code is tested first by a couple of decoupled cases: elasticity and steady-state flow. The analytical solution for a single-phase single-porosity traditional consolidation problem is then used to verify the numerical algorithm for coupled poroelastic systems. Finally a fully coupled two-phase flow and solid deformation problem is presented to compare results from both the developed model and the finite difference model. The results from this case indicate

the validity and capability of the model.

Several applications including traditional consolation problems and simulation of rock sample behavior in the laboratory are presented to illustrate additional performance and capability of the model. Parametric studies, such as fracture spacing and the ratio between the fracture permeability and the rock matrix permeability, allow better understanding of the developed model and the physical characteristics in the studied problem. A example problem is presented to demonstrate the significant different results from both the single-porosity and dual-porosity approaches. For simulating the rock sample characteristics, a series of studies have been carried out which include single-phase and two-phase fluid flow in both single-porosity and dual-porosity approaches.

In comparison with other existing models of two-phase flow and solid deformation in fractured porous media, the present study offers more precise definition for the interactive response between the matrix and the fractures in view of flow. In addition, the comprehensive coverage of the influential mechanisms in the present analysis is secured by complying with the rigorous theoretical derivations, rather than formulating the governing equations based on a phenomenological fashion, as shown in some other current models.

The developed numerical model can be a powerful tool to solve different problems in petroleum engineering, such as purely elasticity, steady-state flow, coupled problems of single-porosity single-phase, single-porosity two-phase, dual-porosity single-phase and dual-porosity two-phase. Also it can be used to simulate difficult problems, for example water-flooding, reservoir evaluation, borehole stability and reservoir subsidence.

Chapter 1

Introduction

Two-phase flow through fractures occurs in many subsurface flow systems that are of engineering interest in the context of energy resources recovery (petroleum, natural gas, geothermal water and steam) and environmental protection areas (chemical contamination in groundwater aquifers, partially saturated zones).

Experience with two-phase flow has been considerably more extensive in the petroleum engineering field than in the field of groundwater hydrology. Although both fields have a common basis in the physics of immiscible fluids, they address different sets of problems. For example, interest in fractured petroleum reservoirs commonly focuses on prediction of oil displacement from matrix blocks under various recovery plans. Predicted pressure changes in each fluid phase are key variables in characterizing reservoir performance. In geothermal systems, the phases of interest are steam and water, and an important area of concern is the generation and migration of steam with a decline in the reservoir pressure. In environmental applications, an important issue concerns the redistribution of an organic solvent in a water-saturated medium that initially contains none of this phase. In this case the interest is in the spatial extent and distribution of solvent in the subsurface (Committee on fracture characterization and fluid flow, 1996).

Understanding the fluid flow behavior is particularly essential for the successful

development of a naturally fractured reservoir. It is estimated that such formations contain a substantial amount of oil. Because of the usually low primary production from these reservoirs and the increasing scarceness of new oil fields, the application of enhanced oil recovery processes in naturally fractured reservoirs is now receiving a greater attention. Yet, fluid flow phenomena in such reservoirs are not adequately understood; and considerably more research needs to be done in this area.

Numerical simulation is recognized as a valuable tool for reservoir engineering studies. Simulation enables one to forecast field performance under a variety of production schemes. An oil-field can only be produced one time; and once the production scheme is selected, it is often irreversible. The advantage of reservoir simulation lies in the fact that the simulation model can be run many times at relatively low cost, allowing engineers to experiment with several sets of input data; i.e. the models can easily be "exercised". Observation of modeling results helps engineers choose the best set of well locations and production schemes.

Simulation of two-phase flow in a naturally fractured petroleum reservoir is normally carried out by using the concept of dual continua, also called "dual-porosity". Finite element, finite difference, boundary element and analytical methods have been employed to solve the equations resulting from the dual-porosity approach.

Special attention should be given to the reservoir deformation or subsidence problems. Numerous field studies related to reservoir compaction and subsidence problems have been reported in the literature, examples of which are the Wilmington Oil field, Long Beach, California (Allen, 1968); the oil fields along the Bolivar Coast of Lake Maracaibo, Venezuela (Merle *et al.*, 1976); the Groningen gas field, The Netherlands (Schoonbeek, 1976) and the Ekofisk Field in the North Sea (Marius, 1990).

In petroleum engineering, rocks have to be modeled as porous media saturated

with pore fluids, such as oil and water. The analyses of the fully coupled systems of the stress-fluid-flow in the naturally fractured reservoir have been studied for many years.

1.1 Objectives of the Research

The major purpose of this dissertation is to study the behavior of two-phase fluid flow through deformable naturally fractured reservoirs. Based on the objectives, the following goals are set:

1. The dual-porosity concept is applied in this study for the naturally fractured reservoirs. The fractured rock has two degrees of porosity, one corresponding to the fractures (fissures) and the other corresponding to the rock pores. The reservoir system is viewed as a poroelastic skeleton infiltrated by a two-state fluid, one flowing through the fractures and the other flowing through the pores.

2. The necessary mathematical formulations for describing the two-phase fluid flow and reservoir deformations are proposed. The fluid flow and reservoir deformation effects are fully coupled through this study, which means one process influences the other and the overall response can not be predicted by considering each process independently. The mathematical derivations of the two immiscible and compressible fluids flowing in a deformable fractured saturated reservoir consist of the equilibrium equation for rock displacements and stresses, and the continuity equations for four fluid pressures in both rock matrix and fissure, respectively. Those balance equations have taken into account the effects of capillarity, saturation and the variation of relative permeability.

3. A three-dimensional computer program is developed based on the derived formulations to simulate the coupled immiscible two-phase fluids flow in a deformable naturally fractured reservoir. The finite element method is used not only for solving the fully coupled systems but also for incorporating different boundary conditions and irregular reservoir shapes and heterogeneous reservoir properties.

4. The two-phase flow problem in deformable fractured reservoir is simulated using the proposed model. Also this model offers the ability to study other kinds of fluid flow problems; for example, elasticity, steady-state flow, single-porosity single-phase flow, single-porosity two-phase flow, and dual-porosity single-phase flow. The finite element code is validated through comparison with analytical solutions for pure elasticity problems, consolidation problems. And also the two-phase simulation results are compared between this model and a finite difference model.

1.2 Problem Definition

1.2.1 Naturally Fractured Reservoirs

Fracture is a term used for all types of generic discontinuities. Folding, faulting and subsidence of sediments over geologic time cause fracturing. Natural fractures affect all phases of the petroleum reservoir life from the accumulation of oil to the techniques used to manage oil production. The existence of fractures in oil reservoirs was known as early as the 1860's. However, in the last thirty or forty years a significant interest in the effect of fractures on oil production has developed. This interest was sparked by the discovery of the giant fields in the Middle East and the Spraberry trend of West Texas. The interest aroused by these discoveries made the industry more aware of the presence and effects of fractures in other reservoirs

(Kazemi and Gilman, 1993).

Naturally fractured reservoirs compose a wide variety of rock mineralogy (carbonate, diatomite, granite, schist, sandstone, shale and coal), porosity and permeability. Carbonates include limestone, dolomite and chalk. Fractured limestones are prevalent in the giant and prolific fields of the Middle East. Fractured dolomites are exemplified by the San Andres formation in many West Texas fields, and fractured chalks are found in Texas (Austin Chalk), the North Sea (Ekofisk) and other parts of the world (Kazemi and Gilman, 1993).

1.2.2 Two-Phase Flow

In this dissertation, the term *two-phase flow* means that two immiscible fluids, such as oil and water, coexist and flow in the available pore space of a porous medium.

This problem has been examined for several decades in an effort to enhance hydrocarbon recovery from fractured reservoirs and to assist in understanding where petroleum reservoirs are likely to be located. Many petroleum reservoirs are situated in fractured porous formations (Pruess and Tsang, 1990). In these reservoirs, two- and three-phase flow of oil, water and gas occurs naturally and in response to production and injection operations. Many natural gas reservoirs with two-phase flow of gas and water are located in tight rocks with predominant fracture permeability. A different kind of two-phase flow, namely, water/vapor flow with strong phase change and latent heat effects, occurs in geothermal reservoirs and in hydrothermal convection systems. Most of these systems are found in fractured rocks with low matrix permeability. Strong two-phase flow effects of water/vapor and water/noncondensible gas are expected near geologic repositories for heat-generating or corroding radioactive wastes. Two-phase flow in fractures also occurs at many industrial and waste disposal sites where organic fluids have been spilled and are infiltrating fractured rock as nonaqueous liquids (Pruess and Tsang, 1990).

1.2.3 Reservoir Compaction

The term *compaction* is used to describe the reduction of sediment volume as a consequence of fluid extraction. In a very simplified view, a sedimentary rock can be seen as being composed of grains and open spaces, called pores, filled with some fluid (water, oil or gas). When this rock is under stress, the total stress applied is supported by the grains (effective stress) and the pore fluid (pore pressure). The study of fluid flow in deformable-saturated porous media as a coupled flow-deformation phenomenon started with the work of Terzaghi (1943) who developed and used a one-dimensional consolidation model. Since then, Biot (1941) has extended the consolidation theory into a more general three-dimensional case, based on a linear stress-strain constitutive relationship and Darcy's flow law.

1.3 Literature Review

Simulation of fluid flow and multiphase flow in fractured porous media is a problem of importance in a number of disciplines including groundwater hydrology, petroleum engineering, soil, geotechnical and geothermal reservoir engineering. Predicting the behavior of multiphase flow in naturally fractured reservoirs has presented a challenge for petroleum reservoir engineers for many years.

1.3.1 Naturally Fractured Reservoirs

For solving fractured reservoir problems, there are two distinctly different approaches. The dual-porosity model approach characterizes a fractured rock mass as a statistically homogeneous medium consisting of a combination of fractures and porous rock matrix (Evans, 1981). The probability of finding a fracture at any point in the system is the same as finding one at any other point. The discrete model approach, however, attempts to model the actual geometry of both the fractures and

the porous rock matrix (Evans, 1981). Thus, it is necessary to determine from the field the geometry, locations, orientation, aperture variations and fluid-mechanical properties of each fracture, and to incorporate this information into the mathematical model. This review will be focused on the dual-porosity approach which will be used in this study.

For the dual-porosity approach, the naturally fractured reservoirs can often be classified as a system of two physical domains. The primary rock matrix which contains large amount of fluids has a rather low permeability; and the fracture which constitutes a small volume but has the ability to transmit a large portion of flow through the porous medium. As a result, researchers tend to conceptualize the naturally fractured reservoir as a double-porosity medium: one porosity represents the matrix blocks and the second represents that of the fractures and vugs.

Barenblatt *et al.* (1960) established the mathematical foundation of flow behavior in dual-porosity rocks. He considered the reservoir as two overlapping continua — matrix and fractures. Flow between the matrix and the fractures was accounted for by the case of source functions.

Later, Warren and Root (1963) developed a radial model for well transient testing purposes (Figure 1.1). According to them, the double-porosity medium had two classes of porosity. The primary porosity was controlled by deposition and lithification. The void systems of sands, sandstones and limestones were typical of this class. The secondary porosity, on the other hand, was controlled by fracturing and jointing. Vugs, joints and fissures which occur in formations such as shale, siltstone, schist, limestone or dolomite were typical of this class of porosity.

In Warren and Root's model, the matrix rock containing the primary porosity was homogeneous and isotropic and was contained within a systematic array of identical, rectangular blocks. These blocks provided flow to the fractures which, in turn,

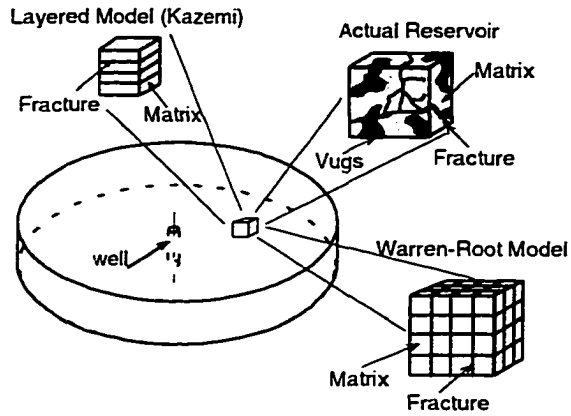

Figure 1.1: Naturally fractured medium (after Kazemi, 1969).

transported the fluid to the well. Superimposed on this system was an orthogonal system of continuous, uniform fractures which were oriented such that each fracture was parallel to one of the principal axes of permeability. Fluid flow in the reservoir occurred through the fractures, which were anisotropic, with local exchange of fluids between the fracture system and matrix blocks, but flow communication between matrix blocks did not occur.

Odeh (1965) attempted to generalize the concept of Warren and Root to accommodate a fractured reservoir in which the pattern of fractures was not known. In his paper, the matrix blocks acted like sources which continuously feed the fractures. The net fluid movement toward the wellbore occurred only in the fractures and the fractures' flow capacity and the degree of fracturing of the reservoir were uniform.

Warren and Root, and Odeh used these conceptual models to develop analytical solutions. These solutions were subsequently extended by Kazemi *et al.* (1969a).

In the same year Kazemi (1969b) presented a "layer cake" model wherein the porous blocks and fractured matrix each occupied a different layer (Figure 1.1). Of significance in this model formulation was the recognition that porous medium flow

was not only orthogonal to the fractures but responded as a continuum over the entire model. As a result of this conceptualization, two mass balance equations appeared: one for the fractures and one for the porous blocks. The equations describing the layer cake model of Kazemi were solved numerically. Kazemi's model differed from Warren and Root's model in that the reservoir consisted of a set of uniformly spaced horizontal matrix layers with a set of horizontal fractures as spacers. The fractures were arranged horizontally, whereby the fracture flow converged radially towards the wellbore.

Theories presented by Aifantis (1977, 1980), Khaled *et al.* (1984) and Wilson and Aifantis (1982) provided a suitable framework in which the flow-deformation behavior of dual-porosity media could be fully coupled. Barenblatt's equations can be recovered from Aifantis' equations as a special case when the rock is assumed to be rigid. Aifantis' theory first provided an alternative derivation of his fissured rock equations through a proper extension of Biot's classical model of flow in single porosity media; and, secondly, developed a finite element methodology for the numerical solution of the relevant equations. The derivation of the governing equations is done by viewing the system as an elastic skeleton infiltrated by a two-state fluid, one flowing through the fissures and the other flowing through the pores. Constitutive assumptions were made for both the fluid strains and total stress. In conformity with the classical theory of Biot, the basic postulates are the equilibrium equation for the total stress and a two-state Darcy's law specifying the flow process in the two types of pores. Under assumptions of solid isotropy, small strains, slight fluid compressibility, absence of macroscopic viscosity and complete saturation, five second-order linear partial differential equations for five unknowns (three solid displacements and two fluid pressures) are derived.

A constitutive model was presented by Elsworth and Bai (1992) to define the

linear poroelastic response of fissured media and determine the influence of dual-porosity effects. In their model, a stress-strain relationship and two equations representing conservation of mass in the porous and fractured material are required. Later, a series of papers were published to study the behavior of dual-porosity media (Bai *et al.*, 1993; Bai *et al.*, 1994; Bai and Meng, 1994; Bai and Roegiers, 1994; Bai *et al.*, 1995; Bai and Roegiers, 1995; Bai *et al.*, 1995).

Lewis and Sukirman (1993a, 1993b), Ghafouri and Lewis (1996) and Lewis and Ghafouri (1997) have developed a model to study the fractured porous media via the dual-porosity concept. In their model, the imposed external loads and /or well production both create a pressure gradient between the fluid within the matrix pores and the fluid in the adjacent fractures. The fluid within the matrix is squeezed out into the fissured continuum due to the produced gradient. Hence, flow towards the producing well takes place through the fissured network. In their model, the fractured porous media are divided into two overlapping but distinct continua, the first represents flow and deformations in the porous matrix while the second represents flow in the fissures. Some assumptions in their model are questionable: within the first continuum, the fluid flow is assumed to be coupled with the matrix deformations only. It means that only pressure in the matrix affects the equilibrium equation; and that pressure in the fissures has no influence. Also the compressibility of the fissure is ignored in their assumptions.

1.3.2 Simulation of Fluid Flow in Fractured Reservoirs

Models that simulate two-phase flow in fractured rock systems arise in petroleum reservoir engineering, in the analysis and development of some geothermal systems and in contaminant hydrogeology. Many papers on single- and two-phase flow in naturally fractured porous media have appeared in the literature and were reviewed in the previous Section.

Mattax and Kyte (1962) were the pioneers on the two-phase flow problem. Their paper gave insight into the mechanism of oil displacement from matrix blocks in a fractured porous rock. They focused on oil recovery by water imbibition from matrix blocks in water-drive reservoirs. From experimental data they developed an empirical oil-recovery correlation in which "*the time required to recover a given fraction of oil from a matrix block is proportional to the square of the distance between fractures* ".

Braester (1972) was also among the first to develop analytical solutions to the multiphase flow in fractured media problems. His conceptual model was similar to that of Barenblatt *et al.* (1960), but his mathematical formulation was different. The source function in his model described the connection between the fractures and the blocks was defined in terms of the potential gradient in the fractures, the capillary pressure difference between the liquid in the fractures and the matrix blocks, and the density difference between liquid phases.

Bossie-Codreanu *et al.* (1985) reported that the first attempt to apply the dual-porosity approach to simulate multiphase flow in fractured reservoirs was presented by Reiss *et al.* (1973). In their approach a conventional three-dimensional three-phase model was used to simulate the fracture behavior.

Another early paper describing a two-phase water-oil flow model was published by Kazemi *et al.* (1975). This model employed a three-dimensional finite-difference formulation to solve the equations. Their model accounted for imbibition, gravity effects, relative mobility and variations in reservoir properties. Their model formulation generated a conservation equation for the blocks and one for the fractures. The two equations were coupled by assuming the matrix flux to the fractures to be proportional to the pressure difference between matrix and fracture. This assumption, which has been called the "pseudo steady-state" or "lumped-parameter"

assumption, was inherent in the early formulation of Barenblatt *et al.* (1960) and used by nearly all subsequent researchers during that period.

In the years since the above work was published, a number of more sophisticated models were developed. Rossen (1977) presented the simulation of naturally fractured reservoir with semi-implicit source terms. The model treated only the flow in the fracture system while considering the rock matrix blocks as source terms. The source terms were functions of the rock matrix and the fluid properties, with fracture saturations and pressures defining the boundary conditions. Matrix blocks surrounded by gas were assumed not to transfer water from the matrix rock to the fracture; and matrix blocks surrounded by water were assumed not to transfer gas from the matrix rock to the fracture.

Duguid and Lee (1977) studied the flow of a single-phase fluid through fractured porous media. In their development, the fractured porous medium was treated as an elastic incompressible solid containing two different porosities. The primary porosity was considered isotropic and the second porosity, associated with the fractures, was anisotropic. The fluid was considered slightly compressible and the fluid velocity in both the primary pores and the fractures was assumed small. This latter assumption allowed the nonlinear portion of the acceleration term in the equation of motion to be neglected. Two sets of governing equations were required to describe flow in fractured porous media, one for each type of porosity. These two sets of equations were coupled by the flow interaction terms between fluid in the primary pores and fluid in the fracture. The finite-element Galerkin method was used to solve this coupled system of equations for transient flow of water in a confined leaky aquifer. Duguid and Lee's work was significant in that it attempted to model simultaneously the flow in both the matrix rock and the fractures, and in their recognition that acceleration terms might have an effect on the equation of motion in the fracture.

Swann (1976, 1978) and Williams (1977) also studied reservoir performance in fractured media by using models developed along the theories of Barenblatt *et al.* (1960) and Warren and Root (1963). In Swann's first paper, he focused on relating the fractured reservoir properties to the well test plots, as opposed to describing the flow phenomena occurring in the rock matrix blocks and the fractures. In his second paper, he presented an analytical theory that describes waterflooding in fractured reservoirs.

One of the most sophisticated multiphase models was presented by Thomas *et al.* (1983). In their paper, the development of a three-dimensional, three-phase model for simulating water, oil and gas flow in a naturally fractured reservoir was described. The reservoir was assumed to be comprised of a continuous fracture system filled with discontinuous matrix blocks. Therefore, flow in the reservoir occurred through the fracture system with local transfer of fluids between the fractures and the matrix blocks; but there was no communication between the matrix blocks. As a result, the governing equations were derived from three fracture flow equations, one for each phase, coupled with three matrix-fracture flow terms. The mathematical formulation was implicit in pressure, water saturation and gas saturation or saturation pressure for both the fracture flow and the matrix-fracture flow. A geometrical factor was used in the matrix-fracture flow terms to account for the surface area of the matrix blocks per unit volume and a characteristic length associated with the terms. Hysteresis on relative permeability and capillary pressures as well as the variation of the gas-oil interfacial tension were incorporated into the model. Several examples were given to demonstrate the utility of their simulation model.

For cases where significant fluid flow occurs between matrix blocks, the dual-porosity model has been extended to what are known as dual-permeability models. The fracture network and matrix blocks were viewed as two superimposed continua,

with both the fractures and the matrix forming continuous flow paths across the reservoir. A "dual-permeability" concept was proposed by Hill and Thomas (1985). Their model differed from the dual-porosity model by the addition of interblock matrix flow terms. If these additional terms were set to zero, the dual-porosity formulation was recovered. One needs to realize that dual-permeability models require much greater computing time than the dual-porosity models. Gilman and Kazemi (1988) used the dual-permeability idealization to develop an efficient algorithm to account accurately for gravity effects both in the fracture and the matrix. They also accounted for viscous displacements in matrix blocks caused by pressure gradient in the fracture network.

The presentation by Gilman (1986) was notable inasmuch as it introduced explicitly the concept of using a numerical solution within the matrix blocks to determine the fluid transfer rate to the fractures. A similar strategy was introduced by Wu and Pruess (1988). They reported a grid refinement scheme to calculate more accurately fluid movement and heat transfer in the matrix as a function of time. An integrated finite-difference model to simulate oil recovery in a fractured medium was formed.

1.3.3 Coupling of Fluid Flow and Rock Deformations

During the last 40 years, many established oil companies and also individual researchers have conducted extensive investigations into the problem of reservoir compaction and its surface subsidence. The remarkable success of their modeling procedures in predicting such a complex deformation behaviour mainly resulted from soil consolidation theory developments which began in the early 20's. The study of flow of fluids in deformable, saturated, porous media as a coupled flow-deformation phenomenon started with the work of Terzaghi (1943) who developed and used a one-dimensional consolidation model. His consolidation theory has been one of the major incentives for the development of soil mechanics. In petroleum engineering,

many authors have observed the relationship between soil consolidation theory and the occurrence of reservoir compaction problems that can induce a considerable amount of subsidence at the surface (Lewis and Sukirman, 1993a; Finol and Ali, 1975). From field observations, it is obvious that reservoir compaction is due to the increased effective stress caused by pore pressure changes during the production of hydrocarbons from the reservoir.

The fundamental work of Biot (1941, 1955) on the general theory of consolidation provided the constitutive stress-strain relationships on which the analysis of stress and fluid flow in deformable porous elastic media was based. Solutions for fully coupled and non-linear behavior of consolidation were quite numerous (Zienkiewicz, 1977; Noorishad *et al.*, 1982; Khaled *et al.*, 1984; Ghafouri and Lewis, 1996). The double-porosity model together with the poroelasticity theory were applied widely to problems of consolidation, surface subsidence, evaluation of the stress, pressure and failure fields around boreholes (Detournay and Cheng, 1988; Elsworth and Bai; 1992; Bai and Meng, 1994; Bai *et al.*, 1995). Also a lot of attempts have been made in simulating multiphase flow in a deforming porous medium (Li *et al.*, 1990; Schrefler and Zhan, 1993; Lewis and Sukirman, 1993a, 1993b).

The paper presented by Li *et al.* (1990) gives the theory of two-phase fluid flow in a porous medium. They adopt a continuum approach, in which a representative element volume around any mathematical point considered in the domain always contains the solid and two-phase fluid flow, and the classical microscopic mass balance law of continuum mechanics will hold for each phase. Based on the generalized Biot theory, their model takes into account the effects of matrix and fluid compressibilities, interphase mass exchange and capillary. The full mathematical model results from two non-linear mass balance equations for the two fluid phases and one non-linear equilibrium equation for the total mixture, subjected to Darcy's law for

multiphase flow and the constraint defining capillary pressure between both fluids.

A lot of papers have been found recently studying the fully coupled effect of multiphase fluid flow with solid deformation (Li and Zienkiewicz, 1992; Sun *et al.*, 1997; Li and Fan, 1997; Chin and Prevost, 1997; Gawin *et al.*, 1997; Klubertanz *et al.*, 1997). The only paper which considered multiphase flow through deformable fractured porous media is given by Lewis and Ghafouri (1997). Their model is based on the theory of double-porosity and accounts for the significant influence of coupling between fluid flow and solid deformations. A Galerkin-based finite element method was applied to discretize the governing equations both in space and time domains. The final set of equations represented a highly non-linear system as the elements of the coefficient matrices were updated during each iteration in terms of the independent variables. As discussed before, some of their assumptions are not reasonable. Also their formulations are given from phenomenon, not from the theory. In such case, some parts in their equations are questionable.

Based on the literature review, it is found that to date, fewer of the existing models have been utilized to specifically study the combined effect of two-phase flow in a deformable saturated reservoirs. Two-phase flow in fractured reservoirs is considered in many papers, but the reservoir is treated as a rigid solid. Some published papers take into account the coupling effect between the multiphase flow and deformations of the reservoir, but the reservoir is considered as an homogeneous porous media. Although many models are used to simulate fluid flow in deformable fractured reservoirs, the fluid is chosen as a single phase instead of multiphase. Thus, the work in this dissertation provides the detailed fundamental theory and the numerical solutions for the coupled effect of two-phase flow in a deformable fractured reservoirs.

When using the dual-porosity method, it should be noted this approach is lim-

ited and only meaningful if the size of elements (in the finite element method) or gridblocks (in the finite difference method) is less than that of the matrix block (Mattax and Dalton, 1990).

1.4 Outline of the Dissertation

Chapter 1 covers the general introduction laying out the objectives for this dissertation and defining the problem. A critical literature review of numerical modeling for the multiphase fluid flow and fully coupled rock-fluid system in naturally fractured media is included.

Chapter 2 derives the appropriate expressions for two-phase fluid flow in fractured porous media using the dual-porosity concept. For this fully coupled system, four equations for the fluid flow aspect and three equations for the solid are developed. Those equations consider the effects of capillary pressure, relative permeability and saturation changes.

Chapter 3 contains the details of the numerical implementation. The numerous unknowns are solved through the finite element technique, which enables the solutions to be derived in general three-dimensional domains. The considerations of poroelasticity, the variations of density and porosity , and the influence of capillary pressure, relative permeability and saturation are also explained.

Chapter 4 focuses on the validation of the numerical algorithm. The theoretical formulations and numerical solutions are validated against pure elasticity, steady-state flow and consolidation cases where the analytical solutions are readily available. Also the two-phase flow results are compared between this model and the finite difference method.

Chapter 5 investigates the parametric influence. Through the parametric changes, the model allows to study the behaviors of pure elasticity, steady state flow, single-

porosity single-phase flow, single-porosity two-phase flow, dual-porosity single-phase flow and dual-porosity two-phase flow. In addition, the parameter studies give better understanding of the model and physical behaviors of the examined problem.

Chapter 6 includes the application of the numerical model. The single-phase and two-phase flow characteristics of the rock sample and flow behaviors are numerically simulated. Through the horizontal injection and vertical injection simulations in both single-porosity and dual-porosity approaches, the use of the model, the solid deformation characteristics and fluid flow behaviors can be better understood.

Finally in Chapter 7, conclusions and recommendations for future studies are given.

Chapter 2

Theoretical Formulations

2.1 Introduction

The basic mechanism of fluid flow in fractured porous media may be explained as follows: the applied external loads and/or well production both create a pressure gradient between the fluid within the matrix pores and the fluid in the fractures. The fluid within the matrix is squeezed out into the fractured medium due to this gradient. Subsequently, flow towards the producing well takes place through the fissured network. In this dissertation, the naturally fractured reservoir is considered as two overlapping continua, one representing the porous matrix while the other representing the deformable fractures (fissures). Based on the dual-porosity concept, the derivations of the seven governing equations for two-phase flow in a deformable naturally fractured reservoir include the equilibrium and the continuity equations. These balance equations need also to take into account the effects of capillarity and the variation of relative permeability and saturation.

The following characteristics and assumptions are made:

1. The reservoir is treated as a double porosity medium. One porosity is associated with the primary rock matrix and the second porosity is associated with the fractures;

2. The rock is a poroelastic compressible solid subject to small deformations. However, other constitutive laws for the rock behavior may also be utilized;

3. Fluid velocities in both the primary rock pores and the fractures are assumed to be small. In such case, Darcy's law is valid;

4. The analysis is related to a macroscopic level which contains a representative sample of rock matrix and fracture geometry;

5. The fluid pressures, saturations, porosities, permeabilities and other properties of both the porous media and the fluids are considered separately;

6. The two-phase fluid flow within each continuum is independent of the flow in the other continuum and any coupling between the fluid flow in the porous matrix and the fracture is controlled only through a interchange term which is assumed to be in quasi-steady state;

7. The rock matrix and fracture systems are assumed to be fully saturated; and,

8. In the following mathematical formulations, subscripts 1 and 2 always refer to the rock matrix and fractured systems; while subscripts o and w stand for oil and water phases, respectively. The stress is defined as tension positive whereas the pressure is compressive positive.

2.2 Preliminary Calculations and Relationships

The main objective in this simulation is to determine the reservoir displacements, the two-phase fluid pressures and saturations for both rock matrix and fracture systems within any given point of the reservoir domain. As will be seen later, the coefficients of the determined non-linear partial differential equations, in addition

to being functions of the independent variables, are also functions of the dependent variables. Those coefficients account for the effects of reservoir heterogeneity, relative permeability, rock and fluid compressibility factors and capillary pressures. These parameters are either pressure- or saturation-dependent. Therefore, all the existing parameters must be converted to an appropriate form before being able to adequately formulate the equations.

2.2.1 Porosities and Saturations

Consider a representative elementary volume in a domain containing a sufficient mixture of rock pores, fracture matrix, and water and oil phases. Pore spaces are represented by porosities, i.e. ϕ_1 for the rock matrix and ϕ_2 for the fracture matrix part. The volume fraction which constitutes rock is, therefore, given by $(1-\phi_1-\phi_2)$. Hence, the volume fraction occupied by the fluid is $(\phi_1+\phi_2)$.

The total volume of the medium is:

$$V = V_s + V_1 + V_2 \tag{2.1}$$

where V represents the total volume, and the subscripts $s, 1$ and 2 of the remaining volume terms denote fluid in the solid, fluid in the pore spaces, and fluid in the fractures, respectively. Porosities are defined for each of the components of the medium as:

$$\phi_s = \frac{V_s}{V}; \qquad \phi_1 = \frac{V_1}{V}; \qquad \phi_2 = \frac{V_2}{V} \tag{2.2}$$

Introducing the time differential operator as:

$$\frac{D}{Dt} = \frac{\partial}{\partial t} + u_{si}\frac{\partial}{\partial x_i} \tag{2.3}$$

where u_{si} is the solid velocity. Applying Equation (2.3) allows the flexibility of switching between the *Lagrangian* and the *Eulerian* coordinate systems; the former being a moving coordinate system.

Computing the derivatives of matrix and fracture porosities with respect to time give:

$$\begin{cases} \dfrac{D\phi_1}{Dt} = \dfrac{1}{V}\left(\dfrac{DV_1}{Dt} - \phi_1 \dfrac{DV}{Dt}\right) \\ \dfrac{D\phi_2}{Dt} = \dfrac{1}{V}\left(\dfrac{DV_2}{Dt} - \phi_2 \dfrac{DV}{Dt}\right) \end{cases} \tag{2.4}$$

The fraction of pore space occupied by each fluid is referred to as the *saturations*. It is assumed that the pore volume is completely filled up with a combination of immiscible fluids. Therefore, the sum of the fluid phase saturations must equal to unity for both matrix and fracture systems, i.e.,

$$\begin{cases} S_{1o} + S_{1w} = 1 \\ S_{2o} + S_{2w} = 1 \end{cases} \tag{2.5}$$

where again, S_{1o}, S_{1w} are the saturations for oil and water phases in the matrix, and S_{2o}, S_{2w} are the equivalent saturations for the fractures, respectively.

2.2.2 Fluid Pressure

In a dual-porosity system, there are four fluid pressures. P_{1o}, P_{2o} are the oil pressures in the matrix and the fracture systems; and P_{1w}, P_{2w} are the water pressures in the matrix and the fracture systems, respectively.

The average pressures can be weighted by the saturations for both matrix and fracture systems as (Lewis *et al.*, 1993a):

$$\begin{cases} P_1 = S_{1o}P_{1o} + S_{1w}P_{1w} \\ P_2 = S_{2o}P_{2o} + S_{2w}P_{2w} \end{cases} \tag{2.6}$$

Even though rock tends to be more water-wet than oil-wet, it can be further assumed that both water and oil phases are in contact with the solid. In the evaluation of solid deformations in the dual-porosity poroelastic media, the traditional methods would consider that the influence of pore pressures is assessed with respect to the individual medium, while the solid deformations due to the volumetric strain

are either neglected in the case of the fractures (Wilson and Aifantis, 1982); or separate deformations are distinguished for the matrix and for the fractures (Elsworth and Bai, 1992).

Differentiating Equation (2.6) with respect to time, one obtains:

$$\begin{cases} \dfrac{\partial P_1}{\partial t} = S_{1o}\dfrac{\partial P_{1o}}{\partial t} + P_{1o}\dfrac{\partial S_{1o}}{\partial t} + S_{1w}\dfrac{\partial P_{1w}}{\partial t} + P_{1w}\dfrac{\partial S_{1w}}{\partial t} \\ \dfrac{\partial P_2}{\partial t} = S_{2o}\dfrac{\partial P_{2o}}{\partial t} + P_{2o}\dfrac{\partial S_{2o}}{\partial t} + S_{2w}\dfrac{\partial P_{2w}}{\partial t} + P_{2w}\dfrac{\partial S_{2w}}{\partial t} \end{cases} \tag{2.7}$$

2.2.3 Capillary Pressures

Capillary pressure plays a major role in defining the initial distribution of fluids in a reservoir and can have a significant influence on the fluid phase pressure variations and fluid movement.

For a given rock, the water/oil capillary pressures depend not only on the saturation but also on the direction of saturation changes. When the displacing fluid is the wetting phase (e.g., water displacing oil), the saturation change is in the imbibition cycle. When the displacing fluid is the non-wetting phase (e.g., oil displacing water), the saturation change is in the drainage cycle. Figure 2.1. Although it is possible to formulate a model that accounts for the hysteresis resulting from the change of direction of flow, in most situations the directions of flow can be predicted and only one set of capillary pressure curves is required.

In a fully-saturated oil reservoir, the fluid pressure values at any point are related by their capillary pressure relationships. In general, *capillary pressure* is defined as the difference between the non-wetting and the wetting phase pressures, i.e.,

$$P_c = P_{non-wetting} - P_{wetting} \tag{2.8}$$

Therefore, for water-wet oil reservoirs, the following expressions are used:

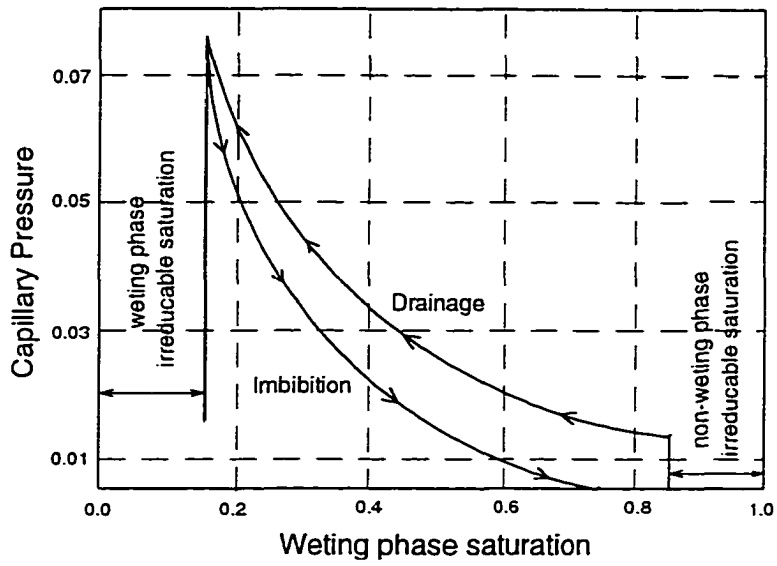

Figure 2.1: Capillary pressure with saturation

For matrix oil-water system,

$$P_{1c} = P_{1o} - P_{1w} \tag{2.9}$$

For fracture oil-water system,

$$P_{2c} = P_{2o} - P_{2w} \tag{2.10}$$

As shown in Figure 2.2, the capillary pressure in the fracture declines rapidly with increasing water saturation (Kazemi *et al.*, 1975). This sets up a pressure differential between the rock matrix and the fractures, causing oil to flow to the fracture and water to flow to the matrix, which is the *imbibition effect*. In some papers, for the fractured network system, the capillary effect has been ignored or has little influence (Lewis, 1993a).

The capillary pressure and water saturation relationship are generally known from laboratory experiments.

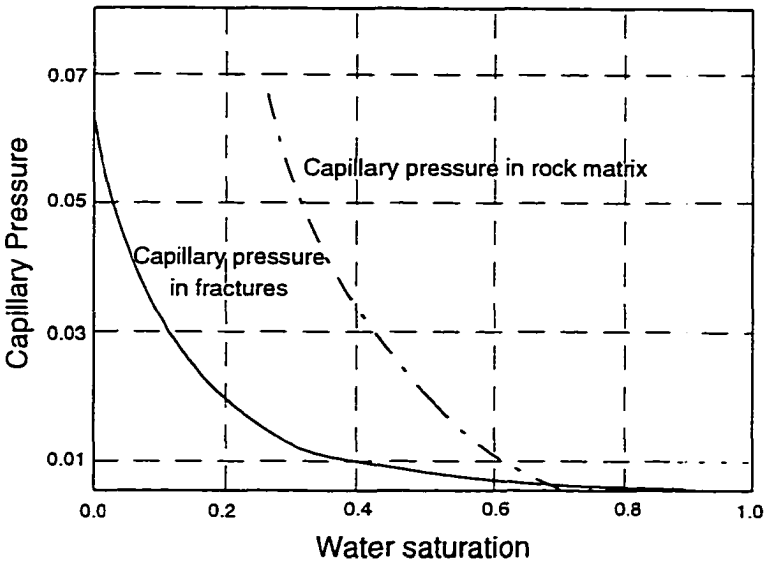

Figure 2.2: Capillary pressures in a fractured reservoir with imbibition

2.2.4 Relative Permeability

Relative permeability relationships are influenced by the history of the rock/fluid system, such as pore geometry, wettability, fluid distribution and saturation history. Both the endpoint values and the shapes of relative permeability functions influence calculated reservoir simulation results, such as fluid pressures and saturations. The basic shapes of the relative permeability curves for the principal rock types in a reservoir are usually defined by laboratory tests on representative core samples.

Figure 2.3 shows a typical oil reservoir relative permeability curve.

2.3 Immiscible Two-Phase Flow Continuity Equations

2.3.1 Mass Conservation Equations

Consider the mass of a representative elementary volume V in a porous medium. Since this volume is composed of fluid and solid, the governing equations for the

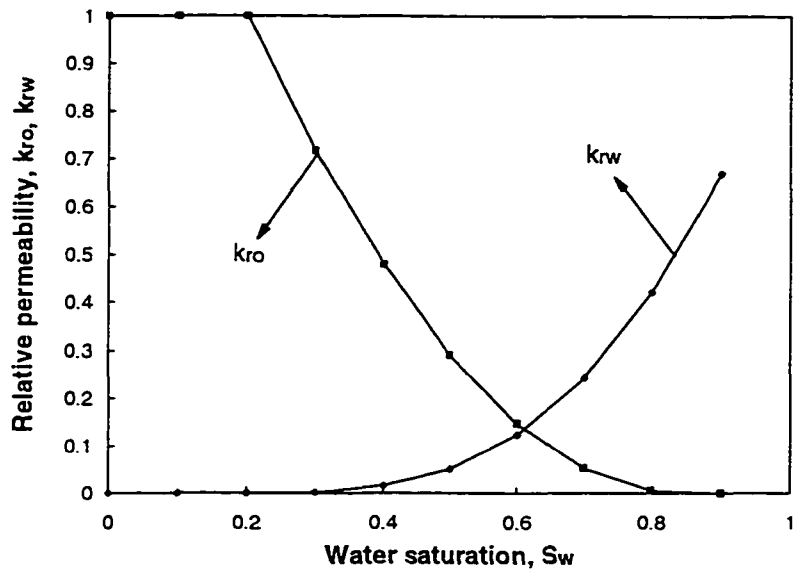

Figure 2.3: Water saturation with relative permeability

conservation of masses of fluid and solid will be derived separately.

The mass of the solid component of the medium can be expressed as the volume fraction of the porous solid, $V_s = (1-\phi)\,V$, times the density of the solid, ρ_s, where ϕ is the sum of matrix and fracture porosities, $\phi = \phi_1 + \phi_2$ (Duguid and Lee, 1977).

For a lumped solid deformation system of the dual-porosity medium, the mass conservation of the solid constituent requires that (Li *et al.*, 1990):

$$\frac{DM_s}{Dt} = \frac{D}{Dt}\int_v (1-\phi)\rho_s dv = \int_v \left[\frac{\partial\,(1-\phi)\,\rho_s}{\partial t} + \frac{\partial\,(1-\phi)\,\rho_s u_{si}}{\partial x_i}\right] dv = 0 \qquad (2.11)$$

It should be noted that Equation (2.11) may contain the discrete porous medium. If continuum mechanism is assumed to prevail, Equation (2.11) can be simplified as:

$$\frac{\partial\,(1-\phi)\,\rho_s}{\partial t} + \frac{\partial\,(1-\phi)\,\rho_s u_{si}}{\partial x_i} = 0 \qquad (2.12)$$

Similarly, the mass conservation equations for the water and oil phases in both rock matrix and fracture systems are as follows:

$$\begin{cases} \dfrac{\partial \phi_1 S_{1w} \rho_{1w}}{\partial t} + \dfrac{\partial \phi_1 S_{1w} \rho_{1w} U_{1wi}}{\partial x_i} - \Gamma_w = 0 \\ \dfrac{\partial \phi_1 S_{1o} \rho_{1o}}{\partial t} + \dfrac{\partial \phi_1 S_{1o} \rho_{1o} U_{1oi}}{\partial x_i} - \Gamma_o = 0 \\ \dfrac{\partial \phi_2 S_{2w} \rho_{2w}}{\partial t} + \dfrac{\partial \phi_2 S_{2w} \rho_{2w} U_{2wi}}{\partial x_i} + \Gamma_w = 0 \\ \dfrac{\partial \phi_2 S_{2o} \rho_{2o}}{\partial t} + \dfrac{\partial \phi_2 S_{2o} \rho_{2o} U_{2oi}}{\partial x_i} + \Gamma_o = 0 \end{cases} \tag{2.13}$$

where $U_{1wi}, U_{1oi}, U_{2wi}$ and U_{2oi} are the intrinsic phase velocities for both fluid phases in the matrix and in the fracture system; $\rho_{1w}, \rho_{1o}, \rho_{2w}$ and ρ_{2o} are the densities of the water and oil phases in the matrix and the fractures; Γ_w and Γ_o are the rate of fluid mass (water and oil) transferred between the porous blocks and the fractures per unit bulk volume of the medium. The interchange flux between the matrix and fractures can be expressed as a function of both time and space. Adopting the simplified assumption of quasi-steady state flux, suggested by Barenblatt *et al.* (1960) and Warren and Root (1963), the following relationship can be written:

$$\Gamma_\pi = \frac{k_1 \rho_{1\pi}}{\mu_{1\pi}} k_{1r\pi} \Psi \left(P_{1\pi} - P_{2\pi} \right) \tag{2.14}$$

where π stands for oil or water phases; the factor Ψ is defined as (Warren and Root, 1963):

$$\Psi = \frac{4n(n+2)}{s^2} \tag{2.15}$$

where $n = 1, 2, 3$ is the number of normal sets of fissures; and s is the average porous block dimension; or, in other words, the average fissure spacing.

Darcy velocities for both fluid phases are defined as:

$$\begin{cases} u_{1wi} = \phi_1 S_{1w} \left(U_{1wi} - u_{si} \right) \\ u_{1oi} = \phi_1 S_{1o} \left(U_{1oi} - u_{si} \right) \\ u_{2wi} = \phi_2 S_{2w} \left(U_{2wi} - u_{si} \right) \\ u_{2oi} = \phi_2 S_{2o} \left(U_{2oi} - u_{si} \right) \end{cases} \tag{2.16}$$

or,

$$u_{\eta\pi i} = \phi_\eta S_{\eta\pi} \left(U_{\eta\pi i} - u_{si} \right) \tag{2.17}$$

where the subscript $\eta = 1, 2$ stands for the rock matrix and fracture systems, and $\pi = o, w$ for the oil and water phases, respectively.

Substituting the first equation in Equation (2.16) into the first Equation of (2.13), expanding the derivatives of Equation (2.12) and the first equation of Equation (2.13), and considering $(*)_{,i}$ to be equal to $\dfrac{\partial(*)}{\partial x_i}$, one ends up with the following expressions:

$$-\phi_2 \frac{\partial \rho_s}{\partial t} - \rho_s \frac{\partial \phi_2}{\partial t} - \phi_1 \frac{\partial \rho_s}{\partial t} - \rho_s \frac{\partial \phi_1}{\partial t} + \frac{\partial \rho_s}{\partial t} - \phi_2 \rho_s u_{si,i} - \phi_1 \rho_s u_{si,i}$$

$$- u_{si} \rho_s \phi_{2,i} - u_{si} \phi_2 \rho_{s,i} - u_{si} \rho_s \phi_{1,i} - u_{si} \phi_1 \rho_{s,i} + \rho_s u_{si,i} + u_{si} \rho_{s,i} = 0 \tag{2.18}$$

$$\phi_1 S_{1w} \frac{\partial \rho_{1w}}{\partial t} + \phi_1 \rho_{1w} \frac{\partial S_{1w}}{\partial t} + S_{1w} \rho_{1w} \frac{\partial \phi_1}{\partial t} + \phi_1 S_{1w} \rho_{1w} u_{si,i} + \phi_1 \rho_{1w} u_{si} S_{1w,i}$$

$$+ \phi_1 S_{1w} u_{si} \rho_{1w,i} + S_{1w} \rho_{1w} u_{si} \phi_{1,i} + \rho_{1w} u_{1wi,i} + u_{1wi} \rho_{1w,i} - \Gamma_w = 0 \tag{2.19}$$

or,

$$-\phi_2 \left(\frac{\partial \rho_s}{\partial t} + u_{si} \rho_{s,i} \right) - \rho_s \left(\frac{\partial \phi_2}{\partial t} + u_{si} \phi_{2,i} \right) - \phi_1 \left(\frac{\partial \rho_s}{\partial t} + u_{si} \rho_{s,i} \right)$$

$$- \rho_s \left(\frac{\partial \phi_1}{\partial t} + u_{si} \phi_{1,i} \right) + \left(\frac{\partial \rho_s}{\partial t} + u_{si} \rho_{s,i} \right) + (1 - \phi_1 - \phi_2) \rho_s u_{si,i} = 0 \tag{2.20}$$

$$\phi_1 S_{1w} \left(\frac{\partial \rho_{1w}}{\partial t} + u_{si} \rho_{1w,i} \right) + \phi_1 \rho_{1w} \left(\frac{\partial S_{1w}}{\partial t} + u_{si} S_{1w,i} \right) + \rho_{1w} u_{1wi,i}$$

$$+ S_{1w} \rho_{1w} \left(\frac{\partial \phi_1}{\partial t} + u_{si} \phi_{1,i} \right) + \phi_1 S_{1w} \rho_{1w} u_{si,i} + u_{1wi} \rho_{1w,i} - \Gamma_w = 0 \tag{2.21}$$

Considering Equation (2.3), the previous equations become:

$$-\phi_2 \frac{D\rho_s}{Dt} - \rho_s \frac{D\phi_2}{Dt} - \phi_1 \frac{D\rho_s}{Dt}$$

$$- \rho_s \frac{D\phi_1}{Dt} + \frac{D\rho_s}{Dt} + (1 - \phi_1 - \phi_2) \rho_s u_{si,i} = 0 \tag{2.22}$$

$$\phi_1 S_{1w} \frac{D\rho_{1w}}{Dt} + \phi_1 \rho_{1w} \frac{DS_{1w}}{Dt} + S_{1w} \rho_{1w} \frac{D\phi_1}{Dt}$$

$$+\phi_1 S_{1w}\rho_{1w}u_{si,i} + \rho_{1w}u_{1wi,i} + u_{1wi}\rho_{1w,i} - \Gamma_w = 0 \tag{2.23}$$

From Equation (2.22), the following expression can be obtained:

$$\frac{D\phi_1}{Dt} = -\frac{\phi_2}{\rho_s}\frac{D\rho_s}{Dt} - \frac{D\phi_2}{Dt} - \frac{\phi_1}{\rho_s}\frac{D\rho_s}{Dt} + \frac{1}{\rho_s}\frac{D\rho_s}{Dt} + (1-\phi_1-\phi_2)\,u_{si,i} \tag{2.24}$$

Substituting Equation (2.24) into Equation (2.23), one gets:

$$\phi_1 S_{1w}\frac{D\rho_{1w}}{Dt} + \phi_1\rho_{1w}\frac{DS_{1w}}{Dt} + (1-\phi_1-\phi_2)\,\frac{S_{1w}\rho_{1w}}{\rho_s}\frac{D\rho_s}{Dt} + \rho_{1w}u_{1wi,i}$$

$$+(1-\phi_2)S_{1w}\rho_{1w}u_{si,i} - S_{1w}\rho_{1w}\frac{D\phi_2}{Dt} + u_{1wi}\rho_{1w,i} - \Gamma_w = 0 \tag{2.25}$$

However, an equation relating the change in fracture porosity to the change in fluid pressures is required. Deriving Equation (2.1) with respect to time, one obtains (Peter and Geogre, 1983):

$$\frac{DV}{Dt} = \frac{DV_s}{Dt} + \frac{DV_1}{Dt} + \frac{DV_2}{Dt} \tag{2.26}$$

Combining Equations (2.4) and (2.26) gives:

$$\frac{D\phi_2}{Dt} = \frac{1}{V}\left[(1-\phi_2)\frac{DV_2}{Dt} - \phi_2\frac{DV_1}{Dt} - \phi_2\frac{DV_s}{Dt}\right] \tag{2.27}$$

Considering the mass conservation equations for each phase and for both rock matrix and fracture systems in differential form, i.e.

$$\begin{cases} \dfrac{D(\rho_s V_s)}{Dt} = 0 \\ \dfrac{D(\rho_{1w} V_{1w})}{Dt} = 0 \\ \dfrac{D(\rho_{1o} V_{1o})}{Dt} = 0 \\ \dfrac{D(\rho_{2w} V_{2w})}{Dt} = 0 \\ \dfrac{D(\rho_{2o} V_{2o})}{Dt} = 0 \end{cases} \tag{2.28}$$

where V_{1w}, V_{1o}, V_{2w} and V_{2o} are the volumes of the water and oil fluid in the matrix and the fractures, respectively.

The relationship between changes in pressure and volume is given through the concept of compressibility, $C = -\frac{1}{V}\frac{dV}{dP}$; or stiffness, $K = \frac{1}{C}$. From the definitions of compressibility of fluid and porosity, the following relationships for different systems can be written:

1. rock matrix:

$$\frac{DV_1}{V_1 Dt} = -\frac{DP_1}{K_1 Dt} = -\frac{D(S_{1o}P_{1o} + S_{1w}P_{1w})}{K_1 Dt} \tag{2.29}$$

2. fractures:

$$\frac{1}{V_2}\frac{DV_2}{Dt} = -\frac{1}{K_2}\frac{DP_2}{Dt} = -\frac{1}{K_2}\frac{D(S_{2o}P_{2o} + S_{2w}P_{2w})}{Dt} \tag{2.30}$$

where K_1 and K_2 are the fluid bulk moduli of rock matrix and fractures, defined as: $K_1 = S_{1w}K_{1w} + S_{1o}K_{1o}$ and $K_2 = S_{2w}K_{2w} + S_{2o}K_{2o}$ (Matthews and Russell, 1967): K_{1w}, K_{1o}, K_{2w} and K_{2o} are the water and oil fluid bulk moduli in the matrix and the fracture systems.

3. water in rock matrix:

$$\frac{1}{\rho_{1w}}\frac{D\rho_{1w}}{Dt} = -\frac{1}{V_{1w}}\frac{DV_{1w}}{Dt} = \frac{1}{K_{1w}}\frac{DP_{1w}}{Dt} \tag{2.31}$$

4. oil in rock matrix:

$$\frac{1}{\rho_{1o}}\frac{D\rho_{1o}}{Dt} = -\frac{1}{V_{1o}}\frac{DV_{1o}}{Dt} = \frac{1}{K_{1o}}\frac{DP_{1o}}{Dt} \tag{2.32}$$

5. water in fractures:

$$\frac{1}{\rho_{2w}}\frac{D\rho_{2w}}{Dt} = -\frac{1}{V_{2w}}\frac{DV_{2w}}{Dt} = \frac{1}{K_{2w}}\frac{DP_{2w}}{Dt} \tag{2.33}$$

6. oil in fractures:

$$\frac{1}{\rho_{2o}}\frac{D\rho_{2o}}{Dt} = -\frac{1}{V_{2o}}\frac{DV_{2o}}{Dt} = \frac{1}{K_{2o}}\frac{DP_{2o}}{Dt} \tag{2.34}$$

7. solid:

$$\frac{1}{\rho_s}\frac{D\rho_s}{Dt} = -\frac{1}{V_s}\frac{DV_s}{Dt} = \frac{1}{K_s}\frac{DP_1}{Dt} + \frac{1}{K_n s}\frac{DP_2}{Dt} - \frac{\sigma'_{ii}(1-\alpha_3)}{3(1-\phi)K_t} \tag{2.35}$$

where,

$$\sigma'_{ii} = 3K_t\left(u_{si,i} + \frac{DP_1}{K_s Dt} + \frac{1}{K_n s}\frac{DP_2}{Dt}\right) \tag{2.36}$$

and with $K_t = K_s(1-\alpha_1)$, $K_t = K_n s(1-\alpha_2)$: α_1 is Biot's constant: K_t, K_s and K_n are the bulk moduli of the solid skeleton, moduli of the grains and fracture normal stiffness, respectively: s is the fracture spacing. The derivations of Equations (2.35) and (2.36) will be found in Appendix A, then Equation (2.35) becomes:

$$\frac{1}{\rho_s}\frac{D\rho_s}{Dt} = -\frac{1}{V_s}\frac{DV_s}{Dt} = \frac{\left[\frac{(\alpha_3-\phi)}{K_s}\frac{DP_1}{Dt} + \frac{(\alpha_3-\phi)}{K_n s}\frac{DP_2}{Dt} - (1-\alpha_3)\,u_{si,i}\right]}{(1-\phi)} \tag{2.37}$$

where $\alpha_3 = \dfrac{\alpha_1\alpha_2}{\alpha_1+\alpha_2}$. Rearranging Equations (2.29)-(2.34) and (2.37), gives:

$$\begin{cases}
\dfrac{DV_1}{Dt} = -\dfrac{\phi_1 V}{(S_{1w}K_{1w} + S_{1o}K_{1o})}\dfrac{DP_1}{Dt} \\
\dfrac{DV_2}{Dt} = -\dfrac{\phi_2 V}{(S_{2w}K_{2w} + S_{2o}K_{2o})}\dfrac{DP_2}{Dt} \\
\dfrac{D\rho_{1w}}{Dt} = \dfrac{\rho_{1w}}{K_{1w}}\dfrac{DP_{1w}}{Dt} \\
\dfrac{D\rho_{1o}}{Dt} = \dfrac{\rho_{1o}}{K_{1o}}\dfrac{DP_{1o}}{Dt} \\
\dfrac{D\rho_{2w}}{Dt} = \dfrac{\rho_{2w}}{K_{2w}}\dfrac{DP_{2w}}{Dt} \\
\dfrac{D\rho_{2o}}{Dt} = \dfrac{\rho_{2o}}{K_{2o}}\dfrac{DP_{2o}}{Dt} \\
\dfrac{D\rho_s}{Dt} = \dfrac{\rho_s\left[\frac{(\alpha_3-\phi)}{K_s}\frac{DP_1}{Dt} + \frac{(\alpha_3-\phi)}{K_n s}\frac{DP_2}{Dt} - (1-\alpha_3)\,u_{si,i}\right]}{(1-\phi_1-\phi_2)} \\
\dfrac{DV_s}{Dt} = -V\left[\dfrac{(\alpha_3-\phi)}{K_s}\dfrac{DP_1}{Dt} + \dfrac{(\alpha_3-\phi)}{K_n s}\dfrac{DP_2}{Dt} - (1-\alpha_3)\,u_{si,i}\right]
\end{cases} \tag{2.38}$$

Substituting Equations (2.27) and (2.38) into Equation (2.25), it follows that:

$$\phi_1 S_{1w}\frac{\rho_{1w}}{K_{1w}}\frac{DP_{1w}}{Dt}+S_{1w}\rho_{1w}\left[\frac{(\alpha_3-\phi)}{K_s}\frac{DP_1}{Dt}+\frac{(\alpha_3-\phi)}{K_n s}\frac{DP_2}{Dt}-(1-\alpha_3)\,u_{si.i}\right]$$

$$-S_{1w}\rho_{1w}\left\{-\frac{(1-\phi_2)\phi_2}{(S_{2w}K_{2w}+S_{2o}K_{2o})}\frac{DP_2}{Dt}+\frac{\phi_2\phi_1}{(S_{1w}K_{1w}+S_{1o}K_{1o})}\frac{DP_1}{Dt}\right.$$

$$\left.+\phi_2\left[\frac{(\alpha_3-\phi)}{K_s}\frac{DP_1}{Dt}+\frac{(\alpha_3-\phi)}{K_n s}\frac{DP_2}{Dt}-(1-\alpha_3)\,u_{si.i}\right]\right\}+\phi_1\rho_{1w}\frac{DS_{1w}}{Dt}$$

$$+(1-\phi_2)S_{1w}\rho_{1w}u_{si.i}+\rho_{1w}u_{1wi.i}+u_{1wi}\rho_{1w.i}-\Gamma_w=0 \qquad (2.39)$$

To obtain the final form of the flow equation in an amenable form, neglecting the convective terms[1], i.e. $\frac{D(*)}{Dt}=\frac{d(*)}{dt}$, and combining Equations (2.7) and (2.39) with Darcy's law, results in:

$$u_{\eta\pi i}=-\frac{k_\eta}{\mu_{\eta\pi}}k_{r\eta\pi}\left(P_{\eta\pi.i}+\rho_{\eta\pi}gh\right) \qquad (2.40)$$

where subscript η stand for the rock matrix and fracture systems, while subscript π are the oil and water fluid phases; k_η are the intrinsic permeabilities in the matrix and fracture systems; $k_{r\eta\pi}$ are the relative permeabilities and $\mu_{\eta\pi}$ are the viscosities of the oil and water phases in the matrix and fracture, respectively; g is the gravitational acceleration and h is the height above a reference level. Then the governing flow equation for the water phase in the matrix can be written as the follow form:

$$\phi_1 S_{1w}\frac{\rho_{1w}}{K_{1w}}\frac{dP_{1w}}{dt}+S_{1w}\rho_{1w}(1-\phi_2)\left[\frac{(\alpha_3-\phi_1-\phi_2)}{K_s}\left(S_{1o}\frac{\partial P_{1o}}{\partial t}+P_{1o}\frac{\partial S_{1o}}{\partial t}\right.\right.$$

$$\left.+S_{1w}\frac{\partial P_{1w}}{\partial t}+P_{1w}\frac{\partial S_{1w}}{\partial t}\right)+\frac{(\alpha_3-\phi_1-\phi_2)}{K_n s}\left(S_{2o}\frac{\partial P_{2o}}{\partial t}+P_{2o}\frac{\partial S_{2o}}{\partial t}\right.$$

$$\left.\left.+S_{2w}\frac{\partial P_{2w}}{\partial t}+P_{2w}\frac{\partial S_{2w}}{\partial t}\right)\right]+\frac{S_{1w}\rho_{1w}(1-\phi_2)\phi_2}{(S_{2w}K_{2w}+S_{2o}K_{2o})}\left(S_{2o}\frac{\partial P_{2o}}{\partial t}+P_{2o}\frac{\partial S_{2o}}{\partial t}\right.$$

$$\left.+S_{2w}\frac{\partial P_{2w}}{\partial t}+P_{2w}\frac{\partial S_{2w}}{\partial t}\right)-\frac{S_{1w}\rho_{1w}\phi_2\phi_1}{(S_{1w}K_{1w}+S_{1o}K_{1o})}\left(S_{1o}\frac{\partial P_{1o}}{\partial t}+P_{1o}\frac{\partial S_{1o}}{\partial t}\right.$$

[1] With small solid velocity, and variable distributions in space not change dramatically, the convective terms may be neglected.

$$+S_{1w}\frac{\partial P_{1w}}{\partial t}+P_{1w}\frac{\partial S_{1w}}{\partial t}\Bigg)-\frac{\rho_{1w}k_1}{\mu_{1w}}k_{r1w}\left(P_{1w,i}+\rho_{1w}gh\right)_{,i}+\phi_1\rho_{1w}\frac{dS_{1w}}{dt}$$

$$+(1-\phi_2)\alpha_3 S_{1w}\rho_{1w}u_{si,i}-\frac{\rho_{1w}k_1}{\mu_{1w}}k_{r1w}\Psi\left(P_{1w}-P_{2w}\right)+Q_{1w}=0 \qquad (2.41)$$

The conservation of mass for water and oil in the matrix and in the fissures may be generally expressed as:

$$\phi_\eta S_{\eta\pi}\frac{\rho_{\eta\pi}}{K_{\eta\pi}}\frac{dP_{\eta\pi}}{dt}+S_{\eta\pi}\rho_{\eta\pi}\left(1-\phi_\xi\right)\Bigg[\frac{\left(\alpha_3-\phi_\eta-\phi_\xi\right)}{K_s}\Bigg(S_{\eta\varpi}\frac{\partial P_{\eta\varpi}}{\partial t}+P_{\eta\varpi}\frac{\partial S_{\eta\varpi}}{\partial t}$$

$$+S_{\eta\pi}\frac{\partial P_{\eta\pi}}{\partial t}+P_{\eta\pi}\frac{\partial S_{\eta\pi}}{\partial t}\Bigg)+\frac{\left(\alpha_3-\phi_\eta-\phi_\xi\right)}{K_n s}\Bigg(S_{\xi\varpi}\frac{\partial P_{\xi\varpi}}{\partial t}+P_{\xi\varpi}\frac{\partial S_{\xi\varpi}}{\partial t}$$

$$+S_{\xi\pi}\frac{\partial P_{\xi\pi}}{\partial t}+P_{\xi\pi}\frac{\partial S_{\xi\pi}}{\partial t}\Bigg)\Bigg]+\frac{S_{\eta\pi}\rho_{\eta\pi}(1-\phi_\xi)\phi_\xi}{\left(S_{\xi\pi}K_{\xi\pi}+S_{\xi\varpi}K_{\xi\varpi}\right)}\Bigg(S_{\xi\varpi}\frac{\partial P_{\xi\varpi}}{\partial t}+P_{\xi\varpi}\frac{\partial S_{\xi\varpi}}{\partial t}$$

$$+S_{\xi\pi}\frac{\partial P_{\xi\pi}}{\partial t}+P_{\xi\pi}\frac{\partial S_{\xi\pi}}{\partial t}\Bigg)-\frac{S_{\eta\pi}\rho_{\eta\pi}\phi_\xi\phi_\eta}{\left(S_{\eta\pi}K_{\eta\pi}+S_{\eta\varpi}K_{\eta\varpi}\right)}\Bigg(S_{\eta\varpi}\frac{\partial P_{\eta\varpi}}{\partial t}+P_{\eta\varpi}\frac{\partial S_{\eta\varpi}}{\partial t}$$

$$S_{\eta\pi}\frac{\partial P_{\eta\pi}}{\partial t}+P_{\eta\pi}\frac{\partial S_{\eta\pi}}{\partial t}\Bigg)-\frac{\rho_{\eta\pi}k_\eta}{\mu_{\eta\pi}}k_{r\eta\pi}\left(P_{\eta\pi,i}+\rho_{\eta\pi}gh\right)_{,i}+\phi_\eta\rho_{\eta\pi}\frac{dS_{\eta\pi}}{dt}$$

$$+(1-\phi_\xi)\alpha_3 S_{\eta\pi}\rho_{\eta\pi}u_{si,i}-(-1)^\eta\frac{\rho_{1\pi}k_1}{\mu_{1\pi}}k_{r1\pi}\Psi\left(P_{1\pi}-P_{2\pi}\right)+Q_{\eta\pi}=0 \qquad (2.42)$$

where $\eta\neq\xi=1,2$ for the rock matrix and fissures; $\pi\neq\varpi=w,o$ for water and oil phases, respectively. The injection and production of water and oil in the matrix and fracture systems are taken into account by introducing appropriate nodal source terms, i.e. Q_{1w}, Q_{1o}, Q_{2w} and Q_{2o}, respectively.

2.3.2 Variation of Fluid Densities and Porosities

The fluid densities in the fluid flow equations can be expressed in terms of fluid pressures. Equation (2.38) shows these relationships. Also these equations can be written as:

$$\frac{d\rho_{\eta\pi}}{\rho_{\eta\pi}}=\frac{dP_{\eta\pi}}{K_{\eta\pi}} \qquad (2.43)$$

Integrating both sides of the above equation; and considering the initial fluid densities, $\rho^0_{\eta\pi}$, and initial fluid pressures, $P^0_{\eta\pi}$, one obtains:

$$\rho_{\eta\pi} = \rho^0_{\eta\pi} \exp\left[\frac{1}{K_{\eta\pi}}\left(P_{\eta\pi} - P^0_{\eta\pi}\right)\right] \tag{2.44}$$

The changes of rock matrix and fracture porosities can be determined at each timestep by solving Equations (2.24) and (2.25) in an explicit manner. Neglecting the convective terms and regrouping Equation (2.25) gives:

$$\frac{d\phi_2}{dt} = \frac{\phi_1}{\rho_{1w}}\frac{d\rho_{1w}}{dt} + \frac{\phi_1}{S_{1w}}\frac{dS_{1w}}{dt} + \frac{(\alpha_3 - \phi_1 - \phi_2)}{K_s}\frac{dP_1}{dt} + \frac{u_{1wi,i}}{S_{1w}}$$
$$+\frac{(\alpha_3 - \phi_1 - \phi_2)}{K_n s}\frac{dP_2}{dt} + (\alpha_3 - \phi_2)u_{si,i} + \frac{u_{1wi}\rho_{1w,i}}{S_{1w}\rho_{1w}} - \frac{\Gamma_w}{S_{1w}\rho_{1w}} \tag{2.45}$$

The above equation is discretized in time as:

$$\frac{\phi_2^{n+1} - \phi_2^n}{\Delta t} = \frac{\phi_1^n}{\rho_{1w}^n}\frac{\rho_{1w}^{n+1} - \rho_{1w}^n}{\Delta t} + \frac{\phi_1^n}{S_{1w}^n}\frac{S_{1w}^{n+1} - S_{1w}^n}{\Delta t} + (\alpha_3 - \phi_2^n)u_{si,i}^n + \frac{u_{1wi}^n \rho_{1w,i}^n}{S_{1w}^n \rho_{1w}^n}$$
$$+\frac{(\alpha_3 - \phi^n)}{K_s}\frac{P_1^{n+1} - P_1^n}{\Delta t} + \frac{(\alpha_3 - \phi^n)}{K_n s}\frac{P_2^{n+1} - P_2^n}{\Delta t} + \frac{u_{1wi,i}^n}{S_{1w}^n} - \frac{\Gamma_w^n}{S_{1w}^n \rho_{1w}^n} \tag{2.46}$$

All the terms are known at time n and the terms in right-hand side of equation at time $n+1$ are also known. In such case, the porosity ϕ_2^{n+1} can be obtained. Following the same reasoning, ϕ_1^{n+1} can also be determined as:

$$\frac{\phi_1^{n+1} - \phi_1^n}{\Delta t} = \frac{(\alpha_3 - \phi^n)}{K_s}\frac{P_1^{n+1} - P_1^n}{\Delta t} + \frac{(\alpha_3 - \phi^n)}{K_n s}\frac{P_2^{n+1} - P_2^n}{\Delta t}$$
$$-\frac{\phi_2^{n+1} - \phi_2^n}{\Delta t} + (1 - \phi_1^n - \phi_2^n)\, u_{si,i}^n \tag{2.47}$$

2.4 Rock Deformations

2.4.1 Constitutive Relationships

The relationships between changes in total stresses (σ_{ij}) and intergranular stresses σ'_{ij} are given by (Terzaghi, 1943):

$$\sigma_{ij} = \sigma'_{ij} - \alpha_1 \delta_{ij} P_1 - \alpha_2 \delta_{ij} P_2 \tag{2.48}$$

where subscripts 1 and 2 refer to the rock matrix and the fractured systems: σ'_{ij} represents the effective stresses, α_1 and α_2 are the pore pressure ratio factors, which can be evaluated approximately as: $\alpha_1 = 1 - \frac{K_t}{K_s}$, $\alpha_2 = 1 - \frac{K_t}{K_n s}$, where K_n is the fissure normal stiffness and s is the fissure spacing; δ_{ij} is the *Kronecker delta*, which by definition is such that: $\delta_{ij} = 1$, when $i = j$ and $\delta_{ij} = 0$ when $i \neq j$.

The linear constitutive relationships for the system are defined as:

$$\sigma'_{ij} = D_{ijkl}\varepsilon_{kl} \tag{2.49}$$

And the inverse relation recovered from Equation (2.49) is:

$$\varepsilon_{ij} = C_{ijkl}\sigma'_{kl} \tag{2.50}$$

where D_{ijkl} is the elasticity matrices, C_{ijkl} is the compliance matrices for the system, respectively. Those matrices will be defined subsequently.

Substituting Equation (2.48) into Equation (2.50) gives:

$$\varepsilon_{ij} = C_{ijkl}\sigma_{kl} + C_{ijkl}\alpha_1\delta_{kl}P_1 + C_{ijkl}\alpha_2\delta_{kl}P_2 \tag{2.51}$$

or,

$$\sigma_{ij} = D_{ijkl}(\varepsilon_{kl} - C_{klmn}\alpha_1\delta_{mn}P_1 - C_{klmn}\alpha_2\delta_{mn}P_2) \tag{2.52}$$

The elasticity matrix D_{ijkl} can be defined explicitly, in a three-dimensional geometry for an isotropic medium, as:

$$\left[\ D_{ijkl}\ \right] = (C_{ijkl})^{-1} =$$

$$= \frac{1}{|\ D_{ijkl}\ |} \begin{bmatrix} d_{11} & d_{12} & d_{13} & 0 & 0 & 0 \\ d_{21} & d_{22} & d_{23} & 0 & 0 & 0 \\ d_{31} & d_{32} & d_{33} & 0 & 0 & 0 \\ 0 & 0 & 0 & d_{44} & 0 & 0 \\ 0 & 0 & 0 & 0 & d_{55} & 0 \\ 0 & 0 & 0 & 0 & 0 & d_{66} \end{bmatrix} \tag{2.53}$$

where. the compliance matrices are as follows:

$$C_{ijkl} = \frac{1}{E}\begin{bmatrix} 1 & -\nu & -\nu & 0 & 0 & 0 \\ -\nu & 1 & -\nu & 0 & 0 & 0 \\ -\nu & -\nu & 1 & 0 & 0 & 0 \\ 0 & 0 & 0 & 2(1+\nu) & 0 & 0 \\ 0 & 0 & 0 & 0 & 2(1+\nu) & 0 \\ 0 & 0 & 0 & 0 & 0 & 2(1+\nu) \end{bmatrix} \tag{2.54}$$

and.

$$\mid D_{ijkl} \mid = \left[\frac{2(1+\nu)}{E}\right]^3 \left(\frac{1}{E^3} - \frac{3\nu^2}{E^3} - \frac{2\nu^3}{E^3}\right) \tag{2.55}$$

$$d_{11} = d_{22} = d_{33} = \left[\frac{2(1+\nu)}{E}\right]^3 \left(\frac{1}{E^2} - \frac{\nu^2}{E^2}\right) \tag{2.56}$$

$$d_{12} = d_{21} = d_{13} = d_{31} = d_{23} = d_{32} = \left[\frac{2(1+\nu)}{E}\right]^3 \left(\frac{\nu}{E^2} + \frac{\nu^2}{E^2}\right) \tag{2.57}$$

$$d_{44} = d_{55} = d_{66} = \left[\frac{2(1+\nu)}{E}\right]^2 \left(\frac{1}{E^3} - \frac{3\nu^2}{E^3} - \frac{2\nu^3}{E^3}\right) \tag{2.58}$$

where E is the elastic modulus. ν is Poisson's ratio.

2.4.2 Equilibrium Equations

The equilibrium equation of motion for a solid may be written as:

$$\sigma_{ij,j} + F_i = 0 \tag{2.59}$$

where F_i is the vector of body tractions. The strain-displacement relationship is defined as:

$$\varepsilon_{ij} = \frac{1}{2}\left(u_{i,j} + u_{j,i}\right) \tag{2.60}$$

Inserting Equation (2.52) into Equation (2.59), the expanded equilibrium equation can be expressed as:

$$\left(D_{ijkl}\varepsilon_{kl} - D_{ijkl}C_{klmn}\alpha_1\delta_{mn}P_1 - D_{ijkl}C_{klmn}\alpha_2\delta_{mn}P_2\right)_{,j} + F_i = 0 \tag{2.61}$$

The stage is now set for a description of the general numerical solution of these fully coupled equations and of particular finite element formulations which have been

incorporated into the computer programs. The *finite element method* is applied to discretize the governing equations both in the space and time domains. How to solve this highly non-linear system, how to choose unknowns and how to update the coefficient matrices during each iteration in terms of the independent variables are also presented in the next Chapter.

Chapter 3

Numerical Implementation

In general two types of approaches can be used to obtain solutions to a mathematical model: *analytical methods* and *numerical methods*. When using analytical methods one seeks to obtain a functional representation for the solution of the partial differential equations. If the analytical solution can be obtained, the accuracy is perfect and can be used to study reservoir behavior, to interpret data from laboratory and field experiments, and to verify the accuracy of solutions obtained by numerical methods. The principal limitation of analytical methods is that solutions can only be obtained by imposing severely restrictive assumptions about the reservoir properties, boundary conditions, or initial conditions. In most field situations, however, the assumptions required to obtain solutions using analytical methods are not satisfactory.

3.1 Numerical Methods

Numerical methods do not require the restrictive assumptions used in analytical methods. Several types of numerical methods have been used to solve fluid flow problems, the two principal ones being the *finite difference method* and the *finite element method*. Although the word "method" is singular, these terms actually refer to two rather large groups of numerical procedures.

3.1.1 Finite Difference Method

The finite difference method was first applied to problems of fluid flow in the mid-60's (Bruce *et al.*, 1953; Freeze and Whitherspoon, 1966; Pinder and Bredehoeft, 1968; Gambolati *et al.*, 1973; Zaman et al., 1991 and Trescott and Larson, 1977). The method has a number of advantages that contribute to its continued widespread use and popularity:

1. For simple problems (e.g., one-dimensional, steady-state flow in an isotropic and homogeneous reservoirs) the mathematical formulation and computer implementation are easily understood by those without advanced training in mathematics or computer programming;

2. Good textbooks are available to help the beginner;

3. Efficient numerical algorithms have been developed for implementing the finite difference method on computers;

4. Well-documented computer programs for solving flow problems are widely available at little or no cost;

5. The accuracy of solutions to steady-state and transient flow problems is generally quite good; and,

6. Several case histories have been published that describe successful applications of the method.

Unfortunately the finite difference method also has disadvantages:

1. The method works best for rectangular or prismatic reservoirs of uniform composition;

2. It is difficult to incorporate irregular or curved reservoir boundaries, anisotropic and heterogeneous reservoir properties; and,

3. The accuracy of the solutions to fluid flow problems is lower than can be obtained by the finite element method (Istok, 1989). One of the important reasons, for example, is that the boundary conditions can not be satisfied exactly.

3.1.2 Finite Element Method

The finite element method was first used to solve groundwater flow problems in the early 70's (Price *et al.*, 1968; Javandel and Witherspoon, 1968; Zienkiewicz and Parekh, 1970; Pinder and Frind, 1972; Gupta and Tanji, 1976; Neuman and Witherspoon, 1970; Duguid and Abel, 1974, Lewis and Schrefler, 1987). The method has several advantages:

1. Irregular or curved reservoir boundaries can be approximated using elements with straight sides or matched exactly using elements with curved boundaries. The method, therefore, is not limited to "nice" shapes with easily defined boundaries;

2. The anisotropic and heterogeneous reservoir properties can be easily incorporated. This allows the method to be applied to reservoirs composed of several materials;

3. The size of the elements can be varied. This property allows the element grid to be expanded or refined as the need exists;

4. The accuracy of solutions to fluid flow and solid deformation problems is very good (exact in some cases); and,

5. Solutions to the transient and solid deformation problems are generally more accurate than solutions obtained by the finite difference method (Istok, 1989).

The principal disadvantages of the finite element method for solving problems are:

1. For simple problems, the finite element method requires a greater amount of mathematical and computer programming sophistication than does the finite difference method (although this disadvantage disappears for more complicated problems); and,

2. There are fewer well-documented computer programs and case histories available for the finite element method than for the finite difference method.

In this dissertation, the finite element method will be used and the program structure will be based on Zienkiewicz's book (1977).

3.2 Finite Element Discretization

3.2.1 Problem Domain

The first step in the solution of the coupled fluid flow and solid deformations problem by the finite element method is to discretize the problem domain. This is done by replacing the problem domain with a collection of *nodes* and *elements* referred to as the *finite element mesh* (Figure 3.1). Elements may be of any size and the size and shape of each element in the mesh can be different. In this dissertation, the elements with six-, seven-, or eight-nodes are chosen for the three-dimensional problem as shown in Figure 3.2. The values of the material properties are usually assumed to be constant within each element but are allowed to vary from one element to the next.

When preparing the finite element mesh it is important to know that the precision of the solution obtained and the level of computational effort required to obtain a solution will be determined to a great extent by the number of nodes in the mesh. A coarse mesh has a smaller number of nodes and will give a lower precision than a fine mesh. However, the larger the number of nodes in the mesh, the greater will be the required computational effort and cost.

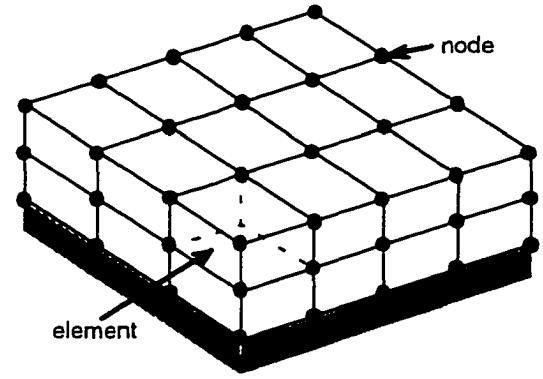

Figure 3.1: Discretization of three-dimensional problem domains

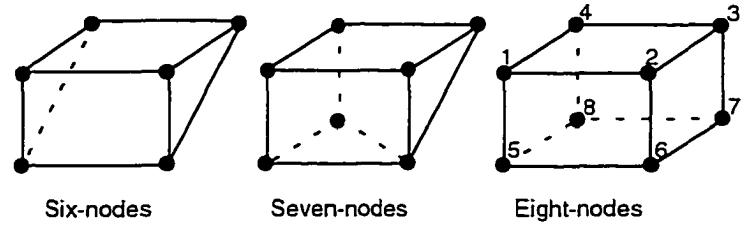

Figure 3.2: Three-dimensional elements

3.2.2 Weighted Residuals Method

The second step in the finite element method is to derive an *integral formulation* for the governing coupled equations. This integral formulation leads to a system of

algebraic equations that can be solved for values of the field variable at each node in the mesh. Several methods can be used to derive the integral formulation for a particular differential equation. The *method of weighted residuals* is a more general approach that is widely used in fluid flow and solid deformation modeling (Istok, 1989).

In the method of weighted residuals, an *approximate solution* to the boundary or initial value problem is defined. When this approximate solution is substituted into the governing differential equations, an error or residual occurs at each point in the problem domain. Then the weighted average of the residuals for each node in the finite element mesh is forced to equal zero.

Consider a differential equation of the form:

$$L\left[\Phi\left(x,y,z\right)\right] - F\left(x,y,z\right) = 0 \tag{3.1}$$

where L is the differential operator; Φ is the field variable, and F is a known function. An approximate solution, $\widehat{\Phi}$, is defined as:

$$\widehat{\Phi}\left(x,y,z\right) = \sum_{i=1}^{m} N_i\left(x,y,z\right)\Phi_i \tag{3.2}$$

where N_i are *interpolation functions* or *shape functions*; Φ_i are the unknown values at the nodes; and m is the number of nodes in the mesh. When the approximate solution is substituted into Equation (3.1), the differential equation is no longer satisfied exactly and has the following residual term:

$$L\left[\widehat{\Phi}\left(x,y,z\right)\right] - F\left(x,y,z\right) = R\left(x,y,z\right) = 0 \tag{3.3}$$

where R is the residual or error due to the approximate solution. The residual varies from point to point within the problem domain. At some point it may be large and at other points it may be small.

In the method of weighted residuals, the weighted residuals at the nodes are forced to be equal to zero, i.e.

$$\int_{\Omega} W(x,y,z)\, R(x,y,z)\, d\Omega = 0 \tag{3.4}$$

where $W(x,y,z)$ is a weighting function and Ω represents the problem domain. Substituting Equation (3.3) into Equation (3.4) gives:

$$\iiint_{\Omega} W(x,y,z) \left\{ L\left[\widehat{\Phi}(x,y,z)\right] - F(x,y,z) \right\} d\Omega = 0 \tag{3.5}$$

In this dissertation, *Galerkin's Method* is used for the weighting function. In *Galerkin's Method* the weighting function for a node is identical to the interpolation function (shape function) used to define the approximate solution $\widehat{\Phi}$.

3.2.3 Shape Function

In the finite element method, the shape function, N_i, is used to obtain the expressions for the variation of the unknown variables within an element in terms of the nodal values. Let $\Phi(x,y,z)$ = unknown function, then one can write:

$$\{\Phi(x,y,z)\} = [\mathbf{N}]\{\Phi(x,y,z)_i\} = [N_1 N_2 \cdots N_n] \begin{Bmatrix} \Phi_1 \\ \Phi_2 \\ \vdots \\ \Phi_n \end{Bmatrix} \tag{3.6}$$

The element, N_i, of this matrix must be such that it takes on a value of unity when evaluated at the geometric coordinates of the i^{th} selected node and has zero value at all the other remaining selected nodes. Figure 3.3 shows linear shape functions for one-dimensional elements with two nodes. It should also be noted that the shape function, N_i, must satisfy the following conditions (Zienkiewicz, 1977):

1. The number of shape functions, N_i, must be equal to the number of nodal values of the element at the selected nodes;

2. Continuity must be provided at nodes and also at element interfaces:

3. The shape function must provide completeness for rigid body displacements and satisfy the constant strain criterion: and.

4. The shape function must possess derivatives to the highest order appearing in the variational functional or the differential equation for the problem.

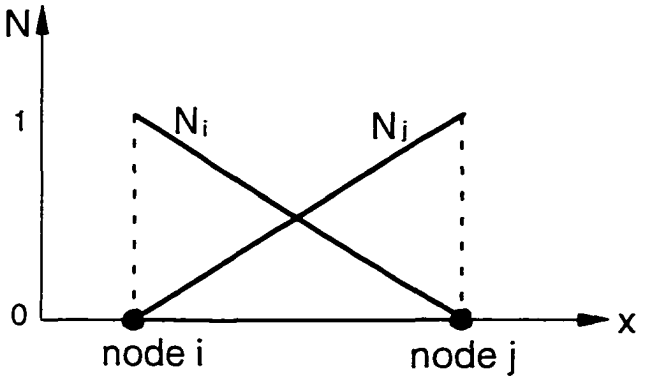

Figure 3.3: Linear shape function for 1-D element with two nodes.

For the three-dimensional eight-noded rectangular prism element (Figure 3.2). the shape functions have the following form:

$$N_i = \frac{1}{8}(1+\xi\xi_i)(1+\eta\eta_i)(1+\zeta\zeta_i) \qquad i = 1, 2, ..., 8 \qquad (3.7)$$

where (ξ, η, ζ) are the element normalized coordinate system. The equations used to transform the element geometry from the system coordinates, (x, y, z), to the element normalized coordinates, (ξ, η, ζ), are:

$$\begin{cases} \xi = \dfrac{x - x_c}{a} \\ \eta = \dfrac{y - y_c}{b} \\ \zeta = \dfrac{z - z_c}{c} \end{cases} \qquad (3.8)$$

where (x_c, y_c, z_c) are the global coordinates of the center of gravity of the three-dimensional rectangular prism element, which has dimensions $2a$ (parallel to x-axis)$\times 2b$ (parallel to y-axis)$\times 2c$ (parallel to z-axis).

The partial derivatives of the shape functions are given by:

$$\begin{Bmatrix} \frac{\partial N_i}{\partial \xi} \\ \frac{\partial N_i}{\partial \eta} \\ \frac{\partial N_i}{\partial \zeta} \end{Bmatrix} = \begin{bmatrix} \frac{\partial x}{\partial \xi} & \frac{\partial y}{\partial \xi} & \frac{\partial z}{\partial \xi} \\ \frac{\partial x}{\partial \eta} & \frac{\partial y}{\partial \eta} & \frac{\partial z}{\partial \eta} \\ \frac{\partial x}{\partial \zeta} & \frac{\partial y}{\partial \zeta} & \frac{\partial z}{\partial \zeta} \end{bmatrix} \begin{Bmatrix} \frac{\partial N_i}{\partial x} \\ \frac{\partial N_i}{\partial y} \\ \frac{\partial N_i}{\partial z} \end{Bmatrix} = [J] \begin{Bmatrix} \frac{\partial N_i}{\partial x} \\ \frac{\partial N_i}{\partial y} \\ \frac{\partial N_i}{\partial z} \end{Bmatrix} \tag{3.9}$$

where $[J]$ is called the *Jacobian matrix* and can be found explicitly in terms of the element local coordinates, (ξ, η, ζ), and the element nodal coordinates, (x, y, z), i.e.

$$[J] = \begin{bmatrix} \frac{\partial x}{\partial \xi} & \frac{\partial y}{\partial \xi} & \frac{\partial z}{\partial \xi} \\ \frac{\partial x}{\partial \eta} & \frac{\partial y}{\partial \eta} & \frac{\partial z}{\partial \eta} \\ \frac{\partial x}{\partial \zeta} & \frac{\partial y}{\partial \zeta} & \frac{\partial z}{\partial \zeta} \end{bmatrix} = \begin{bmatrix} \sum \frac{\partial N_i}{\partial \xi} x_i & \sum \frac{\partial N_i}{\partial \xi} y_i & \sum \frac{\partial N_i}{\partial \xi} z_i \\ \sum \frac{\partial N_i}{\partial \eta} x_i & \sum \frac{\partial N_i}{\partial \eta} y_i & \sum \frac{\partial N_i}{\partial \eta} z_i \\ \sum \frac{\partial N_i}{\partial \zeta} x_i & \sum \frac{\partial N_i}{\partial \zeta} y_i & \sum \frac{\partial N_i}{\partial \zeta} z_i \end{bmatrix} =$$

$$= \begin{bmatrix} \frac{\partial N_1}{\partial \xi} & \frac{\partial N_2}{\partial \xi} & \cdots \\ \frac{\partial N_1}{\partial \eta} & \frac{\partial N_2}{\partial \eta} & \cdots \\ \frac{\partial N_1}{\partial \zeta} & \frac{\partial N_2}{\partial \zeta} & \cdots \end{bmatrix} \begin{bmatrix} x_1 & y_1 & z_1 \\ x_2 & y_2 & z_2 \\ \vdots & \vdots & \vdots \end{bmatrix} \tag{3.10}$$

Equation (3.9) can be rewritten as:

$$\begin{Bmatrix} \frac{\partial N_i}{\partial x} \\ \frac{\partial N_i}{\partial y} \\ \frac{\partial N_i}{\partial z} \end{Bmatrix} = [J]^{-1} \begin{Bmatrix} \frac{\partial N_i}{\partial \xi} \\ \frac{\partial N_i}{\partial \eta} \\ \frac{\partial N_i}{\partial \zeta} \end{Bmatrix} \tag{3.11}$$

3.2.4 Nodal Unknowns and Discretization of the Equations

The finite element discretization of the equilibrium and flow equations may be expressed in terms of the nodal displacements, $\mathbf{u}$, nodal water fluid pressures, and nodal water saturations. Two ways can be chosen to select the nodal unknowns:

1. Nodal displacements, nodal water and oil pressures, i.e. $\mathbf{u}$, P_{1w}, P_{2w}, P_{1o} and P_{2o}; and,

2. Nodal displacements, nodal water pressures and water saturations, i.e. $\mathbf{u}$, P_{1w}, P_{2w}, S_{1w} and S_{2w}.

Other variables like S_{1w}, S_{2w}, S_{1o} and S_{2o} in case 1, and P_{1o}, P_{2o}, S_{1o} and S_{2o} in case 2 can be replaced by P_{1w}, P_{2w}, P_{1o} and P_{2o} for case 1, and P_{1w}, P_{2w}, S_{1w} and S_{2w} for case 2, respectively. The replacement considers both the capillary pressure and saturation relations, defined in Equations (2.5), (2.9) and (2.10). The nodal unknowns in case 1 are discussed in detail through this work.

Defining all quantities in term of nodal variables as follows:

$$\partial\boldsymbol{\varepsilon} = \mathbf{B}\partial\mathbf{u}, \quad \partial\mathbf{P}_{1w} = \mathbf{N}\partial\mathbf{P}_{1w}, \quad \partial\mathbf{P}_{1o} = \mathbf{N}\partial\mathbf{P}_{1o},$$

$$\partial\mathbf{P}_{2w} = \mathbf{N}\partial\mathbf{P}_{2w}, \quad \partial\mathbf{P}_{2o} = \mathbf{N}\partial\mathbf{P}_{2o} \tag{3.12}$$

where $\mathbf{N}$ is the vector of the shape function defined in Equation (3.7): $\mathbf{B}$ is the strain displacement matrix, defined as:

$$[B_i] = \begin{bmatrix} \frac{\partial N_i}{\partial x} & 0 & 0 \\ 0 & \frac{\partial N_i}{\partial y} & 0 \\ 0 & 0 & \frac{\partial N_i}{\partial z} \\ \frac{\partial N_i}{\partial y} & \frac{\partial N_i}{\partial x} & 0 \\ 0 & \frac{\partial N_i}{\partial z} & \frac{\partial N_i}{\partial y} \\ \frac{\partial N_i}{\partial z} & 0 & \frac{\partial N_i}{\partial x} \end{bmatrix} \qquad i = 1, 2, \ldots 8 \tag{3.13}$$

As far as the equilibrium equation is concerned, its most general form is given as:

$$\int_v \mathbf{B}^{\mathbf{T}} \partial\boldsymbol{\sigma} dV - \partial\mathbf{f} = 0 \tag{3.14}$$

where $\partial\mathbf{f}$ is an incremental vector of applied boundary tractions, and the integration is completed over the volume of the domain (dV).

Considering substituting Equations (2.52) and (3.12) into Equation (3.14), dividing by ∂t, one obtains:

$$\int_v \mathbf{B}^{\mathbf{T}} \mathbf{D}_{ijkl} \mathbf{B} dV \frac{\partial \mathbf{u}}{\partial t} - \int_v \mathbf{B}^{\mathbf{T}} \alpha_1 \mathbf{m} \mathbf{N} dV \frac{\partial \mathbf{P}_1}{\partial t} - \int_v \mathbf{B}^{\mathbf{T}} \alpha_2 \mathbf{m} \mathbf{N} dV \frac{\partial \mathbf{P}_2}{\partial t} = \frac{\partial \mathbf{f}}{\partial t} \tag{3.15}$$

where the vector $\mathbf{m}$ is $[1, 1, 1, 0, 0, 0]^T$.

Incorporating Equation (2.7) into Equation (3.15) gives the equilibrium equation the following form:

$$\int_v \mathbf{B}^{\mathbf{T}} \mathbf{D}_{ijkl} \mathbf{B} \frac{\partial \mathbf{u}}{\partial t} dV - \int_v \mathbf{B}^{\mathbf{T}} \alpha_1 \mathbf{m} \mathbf{N} \left(S_{1o} \frac{\partial P_{1o}}{\partial t} + P_{1o} \frac{\partial S_{1o}}{\partial t} + S_{1w} \frac{\partial P_{1w}}{\partial t} + P_{1w} \frac{\partial S_{1w}}{\partial t} \right) dV - \int_v \mathbf{B}^{\mathbf{T}} \alpha_2 \mathbf{m} \mathbf{N} \left(S_{2o} \frac{\partial P_{2o}}{\partial t} \right.$$

$$+P_{2o}\frac{\partial S_{2o}}{\partial t}+S_{2w}\frac{\partial P_{2w}}{\partial t}+P_{2w}\frac{\partial S_{2w}}{\partial t}\Bigg)dV=\frac{\partial \mathbf{f}}{\partial t} \tag{3.16}$$

In Equation (3.16), the saturation derivative terms can be replaced by Equations (2.5), (2.9) and (2.10):

$$\int_v \mathbf{B^T}\mathbf{D}_{ijkl}\mathbf{B}\frac{\partial \mathbf{u}}{\partial t}dV-\int_v \mathbf{B^T}\alpha_1\mathbf{m}\mathbf{N}\Bigg(S_{1o}\frac{\partial P_{1o}}{\partial t}-P_{1o}\frac{\partial S_{1w}}{\partial P_{1c}}\frac{\partial P_{1c}}{\partial t}$$

$$+S_{1w}\frac{\partial P_{1w}}{\partial t}+P_{1w}\frac{\partial S_{1w}}{\partial P_{1c}}\frac{\partial P_{1c}}{\partial t}\Bigg)dV-\int_v \mathbf{B^T}\alpha_2\mathbf{m}\mathbf{N}\Bigg(S_{2o}\frac{\partial P_{2o}}{\partial t}$$

$$-P_{2o}\frac{\partial S_{2w}}{\partial P_{2c}}\frac{\partial P_{2c}}{\partial t}+S_{2w}\frac{\partial P_{2w}}{\partial t}+P_{2w}\frac{\partial S_{2w}}{\partial t}\Bigg)dV=\frac{\partial \mathbf{f}}{\partial t} \tag{3.17}$$

or,

$$\mathbf{K}_1\dot{\mathbf{u}}+\mathbf{L}_{1w}\dot{\mathbf{P}}_{1w}+\mathbf{L}_{2w}\dot{\mathbf{P}}_{2w}+\mathbf{L}_{1o}\dot{\mathbf{P}}_{1o}+\mathbf{L}_{2o}\dot{\mathbf{P}}_{2o}-\dot{\mathbf{f}}=0 \tag{3.18}$$

where a superscript dot identifies the time derivative. A detailed explanation of the coefficients are given in Appendix B.

For four flow equations in matrix and fracture media, Galerkin's principle was also used to obtain the discretized forms of Equation (2.42).

For the rock matrix and for the case of water phase, Equation (2.42) is combined with Equations (3.12), (2.5), (2.6), (2.7), (2.9) and (2.10) to generate the following equation:

$$-\int_v \nabla\mathbf{N}^T\frac{\rho_{1w}k_1}{\mu_{1w}}k_{r1w}\nabla\mathbf{N}\left(P_{1w}+\rho_{1w}gh\right)dV+\int_v \mathbf{N}^T\phi_1 S_{1w}\frac{\rho_{1w}}{K_{1w}}$$

$$\times\mathbf{N}\frac{dP_{1w}}{dt}dV+\int_v \mathbf{N}^T S_{1w}\rho_{1w}\left(1-\phi_2\right)\mathbf{N}\Bigg\{\frac{(\alpha_3-\phi_1-\phi_2)}{K_s}$$

$$\times\left[S_{1w}\frac{\partial \mathbf{P}_{1w}}{\partial t}-P_{1c}\frac{\partial S_{1w}}{\partial P_{1c}}\left(\frac{\partial P_{1o}}{\partial t}-\frac{\partial P_{1w}}{\partial t}\right)+\left(1-S_{1w}\right)\frac{\partial P_{1o}}{\partial t}\right]$$

$$+\frac{(\alpha_3-\phi_1-\phi_2)}{K_n s}\times\left[S_{2w}\frac{\partial P_{2w}}{\partial t}-P_{2c}\frac{\partial S_{2w}}{\partial P_{2c}}\left(\frac{\partial P_{2o}}{\partial t}-\frac{\partial P_{2w}}{\partial t}\right)\right.$$

$$\left.+\left(1-S_{2w}\right)\frac{\partial P_{2o}}{\partial t}\right]\Bigg\}dV+\int_v \mathbf{N}^T\frac{S_{1w}\rho_{1w}(1-\phi_2)\phi_2}{(S_{2w}K_{2w}+S_{2o}K_{2o})}\mathbf{N}$$

$$\times \left[S_{2w} \frac{\partial P_{2w}}{\partial t} - P_{2c} \frac{\partial S_{2w}}{\partial P_{2c}} \left(\frac{\partial P_{2o}}{\partial t} - \frac{\partial P_{2w}}{\partial t} \right) + (1 - S_{2w}) \frac{\partial P_{2o}}{\partial t} \right] dV$$

$$+ \int_v \mathbf{N}^T \phi_1 \rho_{1w} \mathbf{N} \frac{dS_{1w}}{dP_{1c}} \left(\frac{\partial P_{1o}}{\partial t} - \frac{\partial P_{1w}}{\partial t} \right) dV$$

$$- \int_v \mathbf{N}^T \frac{S_{1w} \rho_{1w} \phi_2 \phi_1}{(S_{1w} K_{1w} + S_{1o} K_{1o})} \mathbf{N} \left[-P_{1c} \frac{\partial S_{1w}}{\partial P_{1c}} \left(\frac{\partial P_{1o}}{\partial t} - \frac{\partial P_{1w}}{\partial t} \right) \right.$$

$$\left. + S_{1w} \frac{\partial P_{1w}}{\partial t} + (1 - S_{1w}) \frac{\partial P_{1o}}{\partial t} \right] dV - \int_v \mathbf{N}^T \frac{\rho_{1w} k_1}{\mu_{1w}} k_{r1w}$$

$$\times \Psi \mathbf{N} (P_{1w} - P_{2w}) \, dV + \int_v \mathbf{N}^T \mathbf{m}^T (1 - \phi_2) S_{1w} \rho_{1w} \alpha_3 \mathbf{B} \frac{\partial \mathbf{u}}{\partial t} dV + \mathbf{Q}_{1w} = 0 \qquad (3.19)$$

The integration of the equation listed above usually requires the use of numerical techniques, and a standard method is that of *Gaussian quadrature*, where the integrands are evaluated at specific points of the element and boundary surfaces and then weighted and summed (Zienkiewicz, 1977).

Equation (3.19) may be written as:

$$\mathbf{K}_{1w} \dot{\mathbf{u}} + (\mathbf{W}_{1w} + \mathbf{E}_w) \times \mathbf{P}_{1w} - \mathbf{E}_w \mathbf{P}_{2w} + \mathbf{W}_{11} \dot{\mathbf{P}}_{1w}$$

$$+ \mathbf{W}_{12} \dot{\mathbf{P}}_{1o} + \mathbf{W}_{13} \dot{\mathbf{P}}_{2w} + \mathbf{W}_{14} \dot{\mathbf{P}}_{2o} = -\mathbf{Q}_{1w} \qquad (3.20)$$

Repeating the same process for other conditions in Equation (2.42), the following discretized forms can be obtained:

Matrix oil phase:

$$\mathbf{K}_{1o} \dot{\mathbf{u}} + (\mathbf{W}_{1o} + \mathbf{E}_o) \times \mathbf{P}_{1o} - \mathbf{E}_o \mathbf{P}_{2o} + \mathbf{W}_{21} \dot{\mathbf{P}}_{1w}$$

$$+ \mathbf{W}_{22} \dot{\mathbf{P}}_{1o} + \mathbf{W}_{23} \dot{\mathbf{P}}_{2w} + \mathbf{W}_{24} \dot{\mathbf{P}}_{2o} = -\mathbf{Q}_{1o} \qquad (3.21)$$

Fracture water phase:

$$\mathbf{K}_{2w} \dot{\mathbf{u}} + (\mathbf{W}_{2w} + \mathbf{E}_w) \times \mathbf{P}_{2w} - \mathbf{E}_w \mathbf{P}_{1w} + \mathbf{W}_{31} \dot{\mathbf{P}}_{1w}$$

$$+ \mathbf{W}_{32} \dot{\mathbf{P}}_{1o} + \mathbf{W}_{33} \dot{\mathbf{P}}_{2w} + \mathbf{W}_{34} \dot{\mathbf{P}}_{2o} = -\mathbf{Q}_{2w} \qquad (3.22)$$

Fracture oil phase:

$$\mathbf{K}_{2o}\dot{\mathbf{u}}+(\mathbf{W}_{2o}+\mathbf{E}_o)\times\mathbf{P}_{2o}-\mathbf{E}_o\mathbf{P}_{1o}+\mathbf{W}_{41}\dot{\mathbf{P}}_{1w}$$

$$+\mathbf{W}_{42}\dot{\mathbf{P}}_{1o}+\mathbf{W}_{43}\dot{\mathbf{P}}_{2w}+\mathbf{W}_{44}\dot{\mathbf{P}}_{2o}=-\mathbf{Q}_{2o} \tag{3.23}$$

A detailed explanation of the above coefficients are listed in Appendix B. Equations (3.20)-(3.23) represent a set of differential equations in time and are most conveniently represented in matrix form as:

$$\begin{bmatrix} 0 & 0 & 0 & 0 & 0 \\ 0 & \mathbf{W}_{1w}+\mathbf{E}_w & 0 & -\mathbf{E}_w & 0 \\ 0 & 0 & \mathbf{W}_{1o}+\mathbf{E}_o & 0 & -\mathbf{E}_o \\ 0 & -\mathbf{E}_w & 0 & \mathbf{W}_{2w}+\mathbf{E}_w & 0 \\ 0 & 0 & -\mathbf{E}_o & 0 & \mathbf{W}_{2o}+\mathbf{E}_o \end{bmatrix} \begin{bmatrix} \mathbf{u} \\ \mathbf{P}_{1w} \\ \mathbf{P}_{1o} \\ \mathbf{P}_{2w} \\ \mathbf{P}_{2o} \end{bmatrix} +$$

$$+\begin{bmatrix} \mathbf{K}_1 & \mathbf{L}_{1w} & \mathbf{L}_{1o} & \mathbf{L}_{2w} & \mathbf{L}_{2o} \\ \mathbf{K}_{1w} & \mathbf{W}_{11} & \mathbf{W}_{12} & \mathbf{W}_{13} & \mathbf{W}_{14} \\ \mathbf{K}_{1o} & \mathbf{W}_{21} & \mathbf{W}_{22} & \mathbf{W}_{23} & \mathbf{W}_{24} \\ \mathbf{K}_{2w} & \mathbf{W}_{31} & \mathbf{W}_{32} & \mathbf{W}_{33} & \mathbf{W}_{34} \\ \mathbf{K}_{2o} & \mathbf{W}_{41} & \mathbf{W}_{42} & \mathbf{W}_{43} & \mathbf{W}_{44} \end{bmatrix} \frac{d}{dt} \begin{bmatrix} \mathbf{u} \\ \mathbf{P}_{1w} \\ \mathbf{P}_{1o} \\ \mathbf{P}_{2w} \\ \mathbf{P}_{2o} \end{bmatrix} = \begin{bmatrix} \frac{df}{dt} \\ -\mathbf{Q}_{1w} \\ -\mathbf{Q}_{1o} \\ -\mathbf{Q}_{2w} \\ -\mathbf{Q}_{2o} \end{bmatrix} \tag{3.24}$$

Since the discretization in space has been carried out, Equation (3.24) now represents a set of differential equations in time. The values of $\mathbf{u}$, P_{1w}, P_{1o}, P_{2w} and P_{2o} at different values in time may be obtained by means of appropriate time-stepping algorithms.

3.2.5 Discretization in Time

Those coupled equations need to be rearranged prior to finding the solution in time. All terms on the right-hand side are known. The matrix relation may be integrated in time by using any convenient representation of the time derivatives. Using a fully

implicit scheme, such that:

$$\begin{cases} \dot{\mathbf{u}}^{t+\Delta t} = \dfrac{1}{\Delta t}\left(\mathbf{u}^{t+\Delta t} - \mathbf{u}^{t}\right) \\ \dot{\mathbf{P}}_{1w}^{t+\Delta t} = \dfrac{1}{\Delta t}\left(\mathbf{P}_{1w}^{t+\Delta t} - \mathbf{P}_{1w}^{t}\right) \\ \dot{\mathbf{P}}_{2w}^{t+\Delta t} = \dfrac{1}{\Delta t}\left(\mathbf{P}_{2w}^{t+\Delta t} - \mathbf{P}_{2w}^{t}\right) \\ \dot{\mathbf{P}}_{1o}^{t+\Delta t} = \dfrac{1}{\Delta t}\left(\mathbf{P}_{1o}^{t+\Delta t} - \mathbf{P}_{1o}^{t}\right) \\ \dot{\mathbf{P}}_{2o}^{t+\Delta t} = \dfrac{1}{\Delta t}\left(\mathbf{P}_{2o}^{t+\Delta t} - \mathbf{P}_{2o}^{t}\right) \end{cases} \tag{3.25}$$

and substituting Equation (3.25) into Equation (3.24) gives:

$$\frac{1}{\Delta t}\begin{bmatrix} \mathbf{K}_1 & \mathbf{L}_{1w} & \mathbf{L}_{1o} \\ \mathbf{K}_{1w} & (\mathbf{W}_{1w}+\mathbf{E}_w)\,\Delta t + \mathbf{W}_{11} & \mathbf{W}_{12} \\ \mathbf{K}_{1o} & \mathbf{W}_{21} & (\mathbf{W}_{1o}+\mathbf{E}_o)\,\Delta t + \mathbf{W}_{22} \\ \mathbf{K}_{2w} & -\mathbf{E}_w\Delta t + \mathbf{W}_{31} & \mathbf{W}_{32} \\ \mathbf{K}_{2o} & \mathbf{W}_{41} & -\mathbf{E}_o\Delta t + \mathbf{W}_{42} \end{bmatrix}$$

$$\begin{bmatrix} \mathbf{L}_{2w} & \mathbf{L}_{2o} \\ -\mathbf{E}_w\Delta t + \mathbf{W}_{13} & \mathbf{W}_{14} \\ \mathbf{W}_{23} & -\mathbf{E}_o\Delta t + \mathbf{W}_{24} \\ (\mathbf{W}_{2w}+\mathbf{E}_w)\,\Delta t + \mathbf{W}_{33} & \mathbf{W}_{34} \\ \mathbf{W}_{43} & (\mathbf{W}_{2o}+\mathbf{E}_o)\,\Delta t + \mathbf{W}_{44} \end{bmatrix} \begin{bmatrix} \mathbf{u} \\ \mathbf{P}_{1w} \\ \mathbf{P}_{1o} \\ \mathbf{P}_{2w} \\ \mathbf{P}_{2o} \end{bmatrix}^{t+\Delta t}$$

$$= \frac{1}{\Delta t}\begin{bmatrix} \mathbf{K}_1 & \mathbf{L}_{1w} & \mathbf{L}_{1o} & \mathbf{L}_{2w} & \mathbf{L}_{2o} \\ \mathbf{K}_{1w} & \mathbf{W}_{11} & \mathbf{W}_{12} & \mathbf{W}_{13} & \mathbf{W}_{14} \\ \mathbf{K}_{1o} & \mathbf{W}_{21} & \mathbf{W}_{22} & \mathbf{W}_{23} & \mathbf{W}_{24} \\ \mathbf{K}_{2w} & \mathbf{W}_{31} & \mathbf{W}_{32} & \mathbf{W}_{33} & \mathbf{W}_{34} \\ \mathbf{K}_{2o} & \mathbf{W}_{41} & \mathbf{W}_{42} & \mathbf{W}_{43} & \mathbf{W}_{44} \end{bmatrix} \begin{bmatrix} \mathbf{u} \\ \mathbf{P}_{1w} \\ \mathbf{P}_{1o} \\ \mathbf{P}_{2w} \\ \mathbf{P}_{2o} \end{bmatrix}^{t} + \begin{bmatrix} \dfrac{df}{dt} \\ -\mathbf{Q}_{1w} \\ -\mathbf{Q}_{1o} \\ -\mathbf{Q}_{2w} \\ -\mathbf{Q}_{2o} \end{bmatrix}^{t+\Delta t} \tag{3.26}$$

Equation (3.26) is formed for all internal nodes of the problem domain and those boundary nodes where the pore pressure values and/or displacements are not prescribed. The number of equations is thus equal to the number of unknown variables.

The complete set of equations may be used in the time-stepping procedure outlined above to determine the values of $\mathbf{u}$, P_{1w}, P_{1o}, P_{2w} and P_{2o} at any point in time relative to their initial values (Lewis and Schrefler, 1987).

3.2.6 Boundary and Initial Conditions

The partial differential equation that governs the model generally will have an infinite amount of solutions, and in order to select from this family of functions the one that describes a particular physical system, it is necessary to impose additional conditions on the solution. These additional conditions, boundary and initial conditions, serve to further characterize the system being modeled.

Two different types of boundary conditions are usually applied: firstly, by specifying the values of pressure and displacement or *Dirichlet's boundary condition* as:

$$\begin{cases} P_{\eta\pi} = P_{\eta\pi b} \\ \mathbf{u} = \mathbf{u}_b \end{cases} \tag{3.27}$$

or, secondly, by prescribing the flow rate and loading force or *Neumann's boundary condition*:

$$\begin{cases} q_{\eta\pi} = q_{\eta\pi b} \\ F = F_b \end{cases} \tag{3.28}$$

where again $\eta = 1, 2$ represents the matrix or the fracture systems; and $\pi = w, o$ represents the water or oil phases, respectively. The values $q_{\eta\pi b}$, $P_{\eta\pi b}$ are the prescribed flow and pressure values at the boundary, respectively; $\mathbf{u}_b$, F_b are the displacements and loading forces on the boundary. In the special case of a closed boundary, also known as an "impermeable" or "no-flow boundary", the flux should be equal to zero, *i.e.* $q_{\eta\pi b} = 0$.

Normally, the initial conditions of a reservoir system can be defined by specifying the initial distribution of fluid pressure within the reservoir and/or its saturation, depending on the unknowns used in the formulation and the updating procedure. In this work, the initial conditions for the three-dimensional reservoir system can

be defined as follows:

$$\begin{cases} \mathbf{u}^0(x,y,z) = \mathbf{u}^i(x,y,z) \\ P^0_{1w}(x,y,z) = P^i_{1w}(x,y,z) \\ P^0_{1o}(x,y,z) = P^i_{1o}(x,y,z) \\ P^0_{2w}(x,y,z) = P^i_{2w}(x,y,z) \\ P^0_{2o}(x,y,z) = P^i_{2o}(x,y,z) \end{cases} \tag{3.29}$$

where P^0_{1w}, P^0_{1o}, P^0_{2w} and P^0_{2o} are the water and oil pressures in the rock matrix and fracture for node (x,y,z) at time zero; P^i_{1w}, P^i_{1o}, P^i_{2w} and P^i_{2o} are the initial water and oil pressures in the rock matrix and fracture systems, respectively. $\mathbf{u}^0$ and $\mathbf{u}^i$ are the displacement values at time zero and the initial displacement values. Also, the initial capillary pressures and relative permeabilities in rock matrix and fracture systems should be defined. The initial saturations may be determined through the relationship with the initial capillary pressures.

3.2.7 Evaluation of Coefficients

Equation (3.26) represents a fully coupled and highly non-linear system which requires a simultaneous solution. The coefficients of the non-linear partial differential equations, in addition to being functions of the independent variables, are also functions of the dependent variables.

For the present system of equations, the coefficients account for the effects of reservoir heterogeneity, relative permeability, rock and fluid compressibility factors, and capillary pressure. These parameters are either pressure- or saturation-dependent. How one can obtain the solutions when the coefficients depend on these solutions will now be discussed.

First, these coefficients may be evaluated from the pressures or saturations of the previous timestep. This approach implies that these coefficients do not change rapidly from one timestep to the next one. This would be true if pressures and

saturations are also not changing rapidly. That is, the pressures and saturations are averaged in time between the last timestep values and the current values. Then, the coefficients are evaluated from the $P^{n+1/2}$ values, whereas the parameters such as k_{r1w}, k_{r2w}, k_{r1o} and k_{r2o} are evaluated from the $S_{1w}^{n+1/2}$, $S_{2w}^{n+1/2}$, $S_{1o}^{n+1/2}$ and $S_{2o}^{n+1/2}$ values. The current values of pressures or saturations may be computed from the following formulae given by Settari and Aziz (1975), and Aziz and Settari (1979):

$$U^{n+1} = U^n + \frac{\Delta t^{n+1}}{\Delta t^n}(U^n - U^{n-1}) \tag{3.30}$$

Whereas, the average values in time may be obtained from:

$$U^{n+1/2} = \frac{U^{n+1} + U^n}{2} \tag{3.31}$$

Second, for an iterative method, these coefficients are evaluated from the most current pressures or saturations of the last iteration within the same timestep. This also means that iterative procedures are performed within each timestep to obtain the final solutions since all the coefficients are dependent on the unknowns (Aziz and Settari, 1979). The non-linear parameters were updated within each iteration level by using the most recent calculations of fluid pressures. The new values of fluid saturation were obtained from the saturation-capillary curves using the most recent calculation of capillary pressures. In this study, the second method is used.

Equation (3.26) must provide a stable solution to be of any practical use. In this study, the stability of the final solution is monitored by applying a convergence criterion, which is based on the maximum relative unknown changes since the last iteration, i.e.

$$\left\| \frac{U_i^{k+1} - U_i^k}{U_i^k} \right\| \leq \epsilon \tag{3.32}$$

where U_i is the unknowns, e.g., $\mathbf{u}$, P_{1w}, P_{1o}, P_{2w} and P_{2o}, at node i; $(k+1)$ and k are the new and old iteration levels, respectively;

ϵ is the convergence limit value, which is chosen according to the requirement of the solution accuracy; the smaller its value, the longer the calculation time. In this dissertation, the value of ϵ is taken as 0.05, which implies that the relative error between two iterations is limited to 5%.

3.3 Computational Procedure

Equation (3.26) forms the required system of seven partial differential equations for two-phase flow in deformable fractured reservoir. Examination of these equations reveals that there are fifteen unknowns, namely, u_x, u_y, u_z, P_{1w}, P_{2w}, P_{1o}, P_{2o}, k_{r1w}, k_{r1o}, k_{r2w}, k_{r2o}, S_{1w}, S_{1o}, S_{2w}, and S_{2o}. Thus, eight auxiliary equations are required to obtain a general solution. These auxiliary equations are merely two sets of constitutive relations. The first set consists of the following relations:

$$\begin{cases} k_{r1w} = f(S_{1w}); \quad k_{r1o} = f(S_{1w}, S_{1o}) \\ k_{r2w} = f(S_{2w}); \quad k_{r2o} = f(S_{2w}, S_{2o}) \\ S_{1o} + S_{1w} = 1.0 : \quad S_{2o} + S_{2w} = 1.0 \end{cases} \tag{3.33}$$

The second set consists of the relations between capillary pressures and saturations. These relations may be written in the form:

$$\begin{cases} P_{1c} = P_{1o} - P_{1w} = f(S_{1o}, S_{1w}) \\ P_{2c} = P_{2o} - P_{2w} = f(S_{2o}, S_{2w}) \end{cases} \tag{3.34}$$

The iterative steps to solve this problem are thus as follows:

(1) Start from time $t = t_0$, inputting data from the given initial values of pressures, saturations, relatively permeabilities and capillary pressures;

(2) Calculate the non-linear coefficient terms in Equation (3.26). Note that all non-linear parameters were updated within each iteration level by using the most recent calculations of fluid pressures;

(3) Solve for the unknowns, $\mathbf{u}$, P_{1w}, P_{1o}, P_{2w} and P_{2o}, at each *Gaussian* points;

(4) Calculate new oil saturations from saturation-capillary relation, find capillary pressures, and from fluid saturations get relatively permeabilities;

(5) Repeat steps (2)-(4) until the convergence condition $\left\| \frac{U_i^{k+1} - U_i^k}{U_i^k} \right\| \leq \epsilon$ is satisfied at each nodal point; and,

(6) Go to next timestep and repeat steps (2)-(5).

Figure 3.4 shows a schematic process of the simultaneous solution procedure for solving a fully implicit formulation of Equation (3.26).

Following the model development, some validation cases are given in the next Chapter.

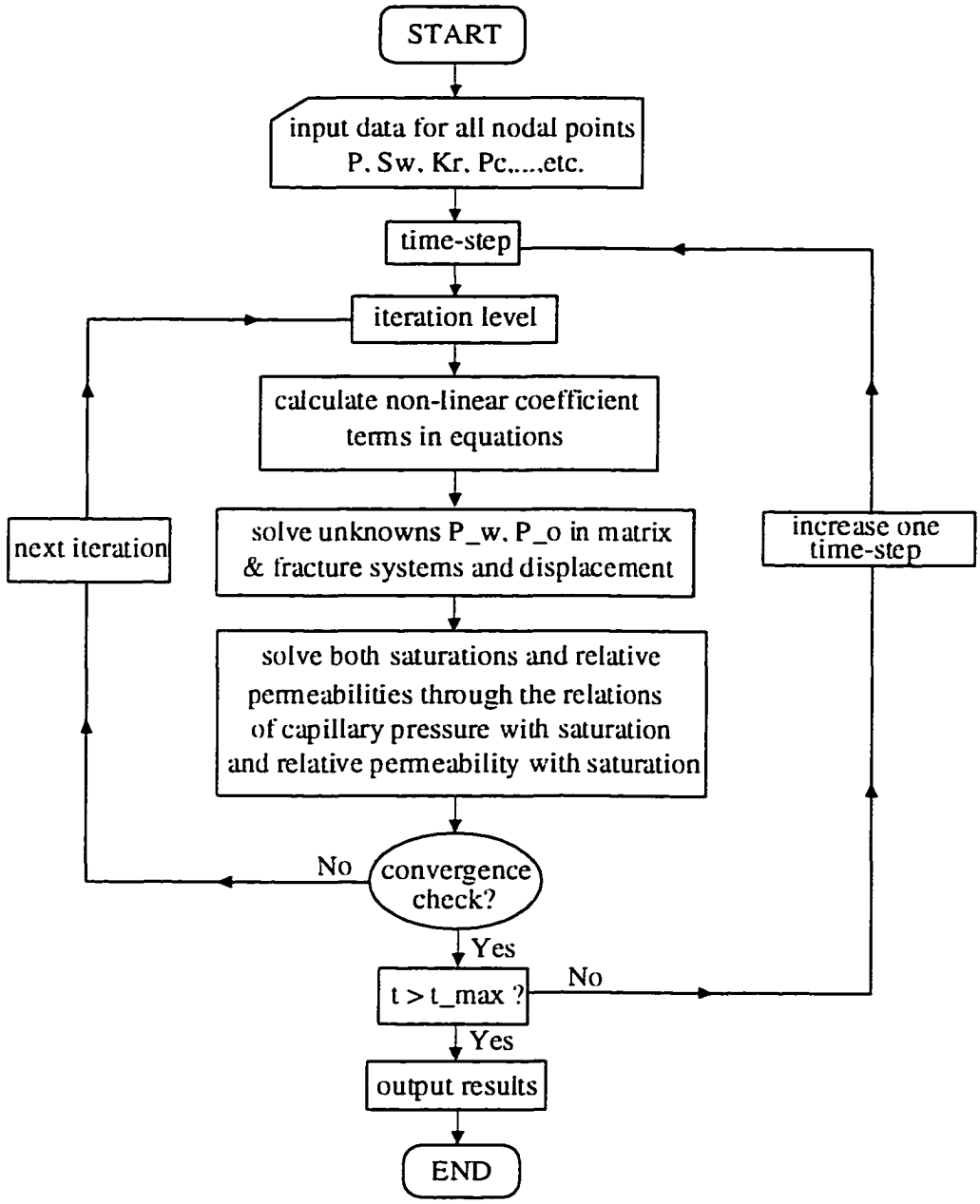

Figure 3.4: Schematic process of the solution procedure.

Chapter 4

Model Validation

The formulation presented in the foregoing Chapters is coded using the FORTRAN Language in three-dimensional space and in the time domain, using eight-noded rectangular elements. In order to validate the computer program, some analytical problems should be simulated. However, there are no suitable problems available in the open literature, and only a few simple analytical solutions and some hypothetical problems do exist. Some of the extreme limiting cases are validated.

Among those validation problems, elasticity and steady-state flow problems are the simple tests for the load-deformation and fluid flow cases; while the one-dimensional consolidation problem is the simplest problem for the coupled fluid-rock systems. Finally, the two-phase flow problem is given to illustrate the capabilities of the model and to validate this finite element model with a finite difference model.

4.1 Elasticity and Steady-State Flow

4.1.1 Elastic Problem

The elastic validation test is carried out by using different element mesh arrangements. The results from numerical elastic solutions are then evaluated by comparing them with the available analytical solutions. The purposes of those examples are to test the performance of the finite element program system, to understand the influ-

ence of different meshes and different element shapes, and to check the accuracy of the numerical solutions.

A cubical block is loaded vertically by a uniformly distributed load of $\sigma_z = 1$ MPa. The block has a Young's modulus $E = 100$ MPa and a Poisson's ratio $\nu = 0.2$ (Figure 4.1). The influence of irregular meshes is evaluated by considering two other cases shown in Figures 4.2 and 4.3 with the same boundary conditions as in Figure 4.1.

The analytical solutions of the strain components are calculated from the general stress-strain relations (Jaeger and Cook, 1979):

$$\varepsilon_{ij} = \frac{1+\nu}{E}\sigma_{ij} - \frac{\nu}{E}\sigma_{kk}\delta_{ij} \tag{4.1}$$

The analytical solutions of the nodal displacements may be obtained from:

$$\begin{cases} u_x = \int_0^x \varepsilon_{11} dx \\ u_y = \int_0^y \varepsilon_{22} dy \\ u_z = \int_0^z \varepsilon_{33} dz \end{cases} \tag{4.2}$$

where $(0, 0, 0)$ is a fixed boundary node.

The errors of the nodal displacements between the numerical and analytical solutions are defined as $\|\mathbf{u}_{numerical} - \mathbf{u}_{analytical}\|$. Three cases show the errors are equal to zero, which means an exact match between the analytical and numerical solutions was achieved.

The boundary conditions can be either forces or displacements according to the given problem. Generally, the displacements of the unknowns in the partial differential equations will be found through force boundary conditions. On the contrary, for the displacement boundary conditions, the solved reactions are the applied forces. Both conditions are tested in the elastic example.

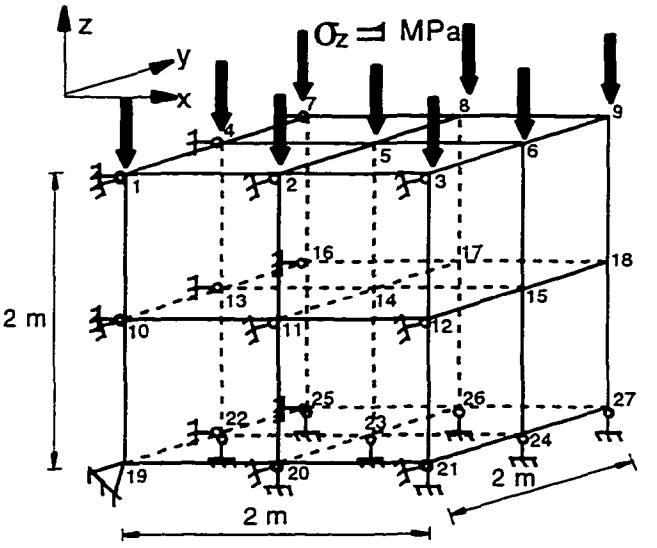

Figure 4.1: Finite element mesh and boundary conditions for elastic test 1.

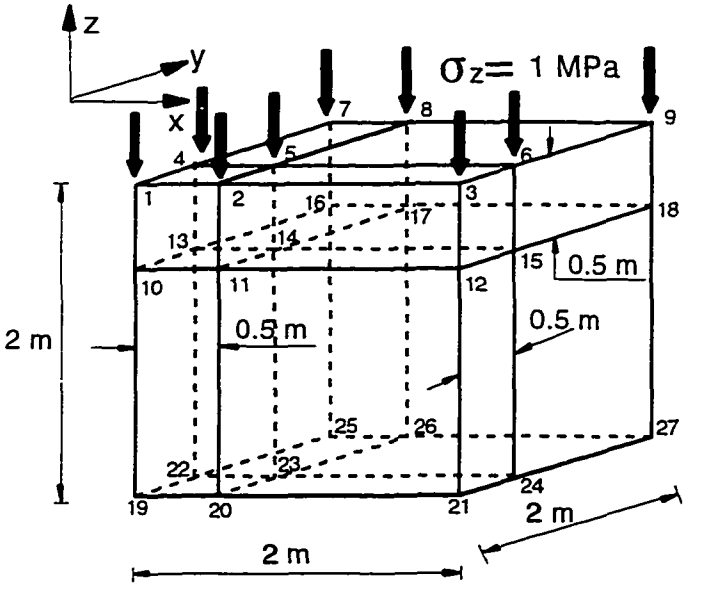

Figure 4.2: Irregular element mesh for elastic test 2.

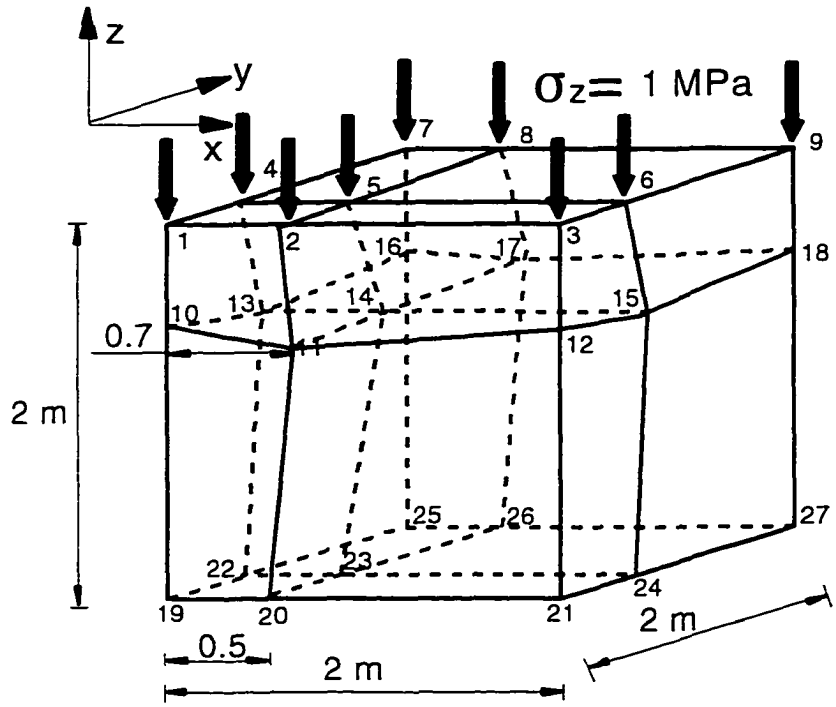

Figure 4.3: Irregular element mesh for elastic test 3.

4.1.2 Steady-state Flow

Single-phase steady-state confined flows of an incompressible fluid which obey Darcy's law, compose the simplest class of flows in a porous medium. Nevertheless, the investigation of this class of flows is important for both theory and practice.

The simplest type of flow is a parallel rectilinear flow between two drainage galleries with a constant pressure over each gallery. Figure 4.4 shows the flow is parallel to the vertical axis with flow boundary conditions at both top and bottom surfaces, and no flow through the sides of the column. From Equation (2.42), the one-dimensional form of the equation for steady-state flow is simply: $\frac{\partial}{\partial z}\left(\frac{k_z}{\mu}\frac{\partial P}{\partial z}\right) = 0$, where k_z is the permeability of the porous media in the vertical direction, μ is the viscosity of the fluid and P is the fluid pressure. In this case, the pressure is distributed linearly over the column; at the top ($z = 0$) $P = P_1$, and at bottom ($z = L$) $P = P_2$. Then it is easy to obtain the following relationship:

$$P = P_1 - \frac{P_1 - P_2}{L} \times z \tag{4.3}$$

Twenty elements are used in this test with $L = 10\ m$, $P_1 = 10.0\ MPa$, $P_2 = 2.0\ MPa$ and $\frac{k_z}{\mu} = 0.1\ m^4/(MN \cdot s)$. Table 4.1 shows the exact match of the pressure distributions along the column comparing numerical and analytical solutions.

4.2 One-dimensional Consolidation

One-dimensional consolidation is one of the most well-known examples of poroelasticity, and its analytical solution is available. The solid column displacements and the single-phase fluid flow are fully coupled in this problem. A cubic porous media column is subjected to a constant load F and confined on the sides and bottom by rigid, frictionless, impermeable walls. The boundary and loading conditions of the

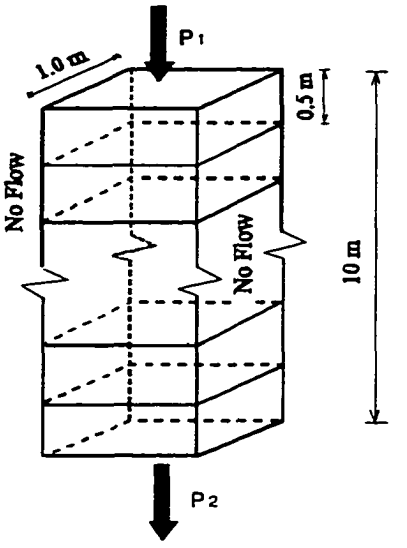

Figure 4.4: Steady-state flow test.

Table 4.1: Pressure distributions.

z (m)	Numerical	Analytical
0.0	10.0	10.0
1.0	9.20	9.20
2.0	8.40	8.40
3.0	7.60	7.60
4.0	6.80	6.80
5.0	6.00	6.00
6.0	5.20	5.20
7.0	4.40	4.40
8.0	3.60	3.60
9.0	2.80	2.80
10.0	2.00	2.00

column are depicted in Figure 4.5. The analytical solution for the pore pressure in this 1-D consolidation problem using the Biot's poroelasticity theory (Biot, 1941) is given by Detournay and Cheng (1993) as:

$$P(x,t) = P_u[1 - F(X,T)] \tag{4.4}$$

where.

$$F(X.T) = 1 - \sum_{m=1,3,\ldots}^{\infty} \frac{4}{m\pi} \sin\left(\frac{m\pi X}{2}\right) \exp(-m^2\pi^2 T) \tag{4.5}$$

and.

$$P_u = -\frac{B(1+\nu_u)}{3(1-2\nu_u)}\sigma_z \tag{4.6}$$

$$X = \frac{x}{L}, \qquad T = \frac{ct}{4L^2} \tag{4.7}$$

in which c is the material compressibility. B is Skempton coefficient's (Skempton. 1954). L is the column length. x and t are the coordinate and time. respectively: σ_z is the instantaneously applied force. and ν_u is the undrained Poisson's ratio.

At the top of the layer. the analytically derived settlement is given by:

$$u = \frac{\sigma_z L(1-2\nu_u)}{2G(1-\nu_u)}\left[1 + \frac{\nu_u - \nu}{(1-\nu)(1-2\nu_u)} f(T)\right] \tag{4.8}$$

where.

$$f(T) = \sum_{m=1,3,\ldots}^{\infty} \frac{8}{m^2\pi^2}[1 - \exp(-m^2\pi^2 T)] \tag{4.9}$$

and G is the shear modulus.

The column. with $L = 1\ m.$ is subjected. at $t = 0^+\ sec.$ to a vertical uniform compressive distribution of $\sigma_z = 1\ MPa$ on the top surface: the surface is otherwise free from stress and exposed to the atmosphere. Twenty block elements and eighty-four nodes were used in the calculations. Materials properties are given as following (the units of the parameters are listed in Table 4.2):

$$\nu = 0.2, \qquad G = 1.0, \qquad c = 1.0$$

Case 1 Incompressible fluid materials, $B = 1$ and $\nu_u = 0.5$. that leads:

$$E = 2.4, \qquad \alpha = 1.0, \qquad M = \infty, \qquad \frac{k_z}{\mu} = 0.375$$

$$K = 1.333, \qquad K_s = \infty, \qquad K_f = \infty$$

Case 2 Compressible materials. $B = 0.8$ and $\nu_u = 0.4$. that leads:

$$E = 2.4, \qquad \alpha = 0.89286, \qquad M = 4.18133, \qquad \frac{k_z}{\mu} = 0.53811$$

$$K = 1.333, \qquad K_s = 12.445, \qquad K_f = 0.1183$$

where the related formulations are listed below:

$$\begin{cases} E = 2G(1+\nu) \\ \alpha = \dfrac{3(\nu_u - \nu)}{B(1-2\nu)(1+\nu_u)} \\ M = \dfrac{2G(\nu_u - \nu)}{\alpha^2(1-2\nu_u)(1-2\nu)} \\ K = \dfrac{E}{3(1-2\nu)} \\ K_s = \dfrac{K}{1-\alpha} \\ \dfrac{1}{M} = \dfrac{\alpha - \phi}{K_s} + \dfrac{\phi}{K_f} \\ \dfrac{k_z}{\mu} = c\dfrac{\alpha^2(1-2\nu)^2(1-\nu_u)}{2G(1-\nu)(\nu_u - \nu)} \end{cases} \tag{4.10}$$

Also the related parameters applied in the analytical and numerical calculations are listed in Tables 4.2 and 4.3.

The comparisons between the analytical solutions (solid lines) and numerical results (scattered points) are made for the temporal evolution of pressure and displacements for both cases. Figures 4.6 and 4.8 show that the fluid pressure changes along the column at different times for case 1 and case 2, while Figures 4.7 and 4.9 demonstrate that the displacements change with time at the column top for case 1 and case 2, respectively. It is seen that an excellent match between the analytical and numerical solutions has been achieved.

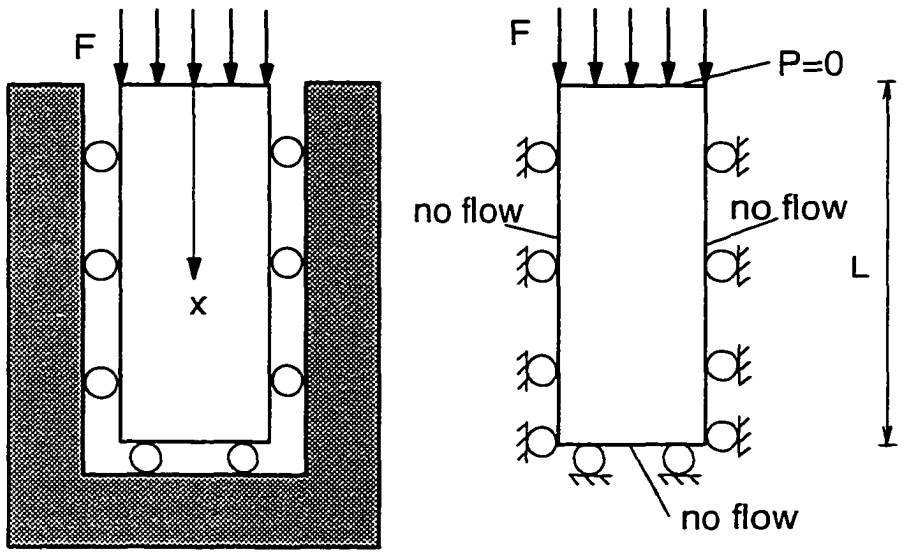

Figure 4.5: Consolidation problem and boundary conditions.

Table 4.2: Parameters used in consolidation case 1.

Parameter	Definition	Magnitude	Units
E	modulus of elasticity	2.4	MN/m^2
ν	Poisson's ratio	0.2	
α_l	Biot coefficient	1.0	
K_f	fluid bulk modulus	1.0E10	MN/m^2
ϕ_l	matrix porosity	0.2	
k_l/μ	matrix mobility	0.375	$m^4/(MN{\cdot}s)$
K_s	solid grain bulk modulus	1.0E10	MN/m^2
B	Skempton coefficient	1.0	
ν_u	undrained Poisson's ratio	0.5	
σ_z	loading stress	1.0	MN/m^2

4.3 Dual-porosity Two-phase Flow Problem

The developed model is further validated in the simulation of a poroelastic soil column with two immiscible porous fluids subjected to a step loading as discussed in the previous Section. The results obtained using the fully-implicit fully-coupled

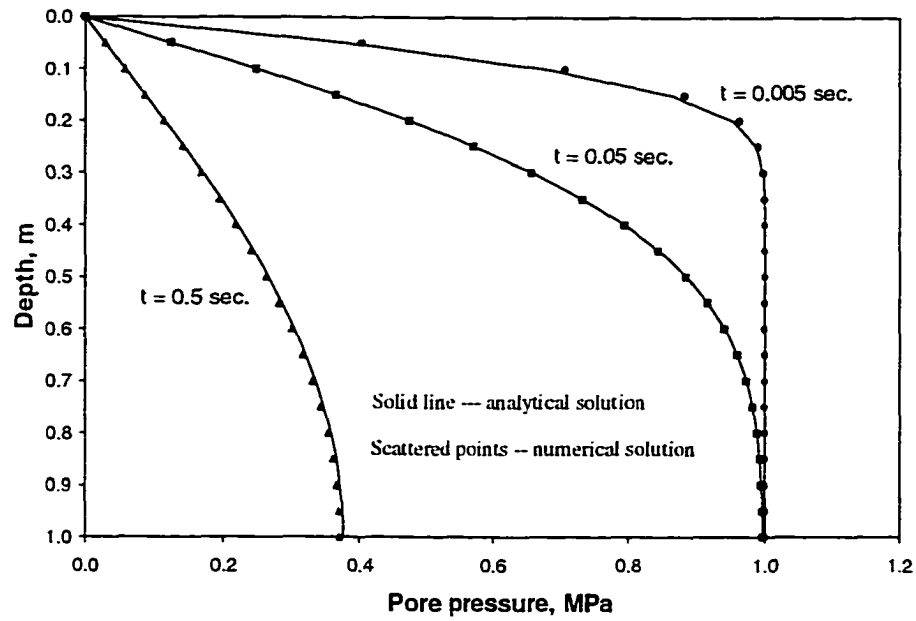

Figure 4.6: Pore pressure distribution along column for case 1.

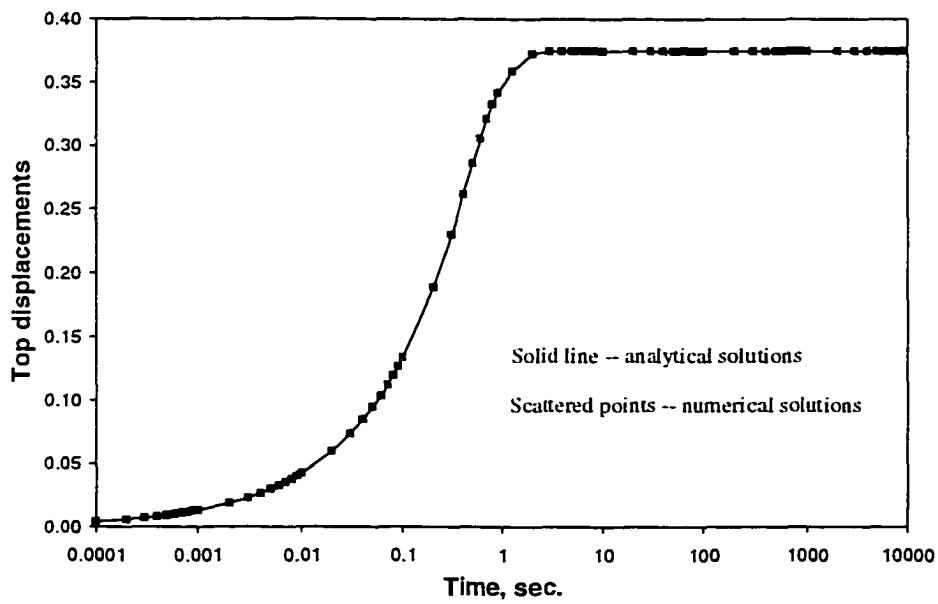

Figure 4.7: Displacement with time at top column for case 1.

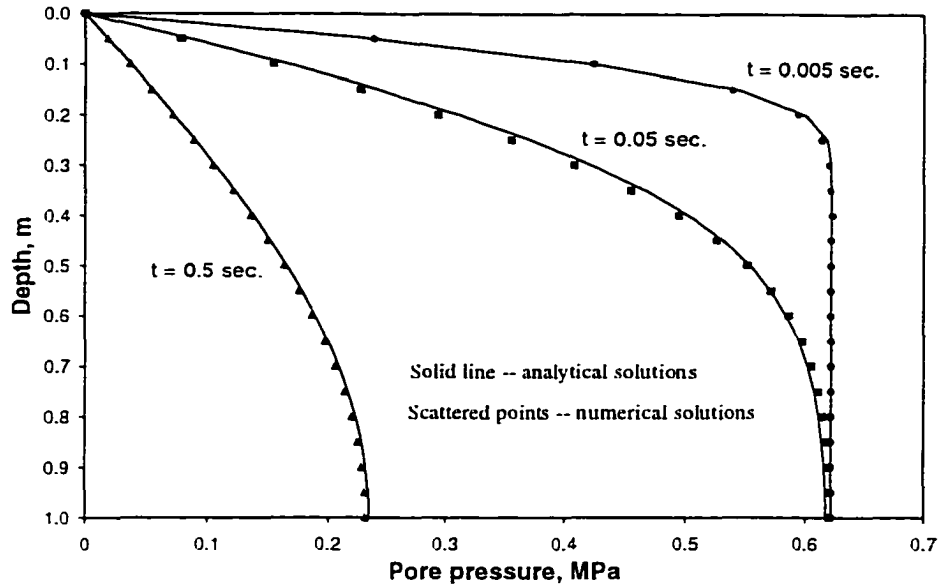

Figure 4.8: Pore pressure distribution along the column for case 2.

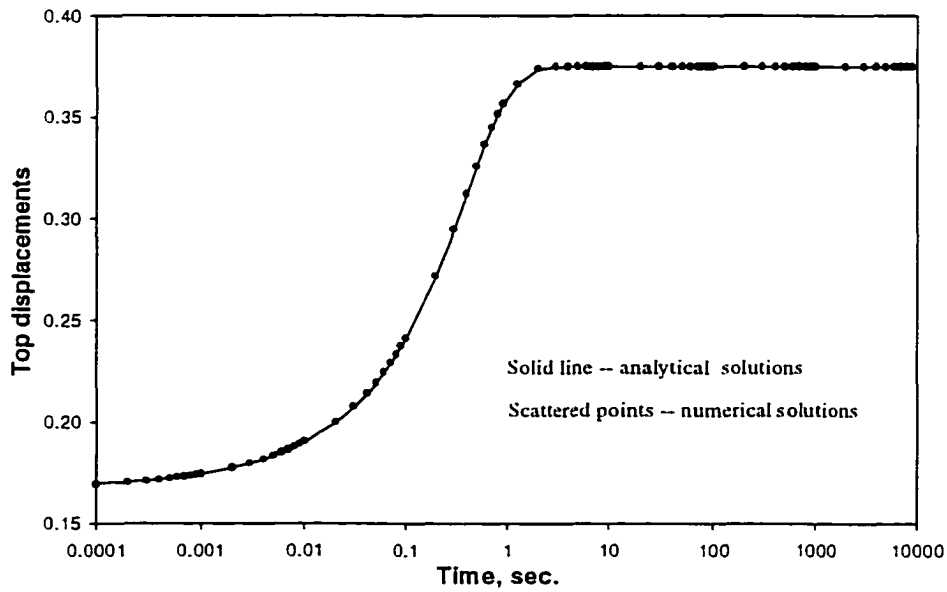

Figure 4.9: Displacement with time at top column for case 2.

Table 4.3: Parameters used in consolidation case 2.

Parameter	Definition	Magnitude	Units
E	modulus of elasticity	2.4	MN/m^2
ν	Poisson's ratio	0.2	
α	Biot coefficient	0.89286	
K_f	fluid bulk modulus	0.1183	MN/m^2
ϕ_1	matrix porosity	0.02	
k_1/μ	matrix mobility	0.53811	$m^4/(MN{\cdot}s)$
K_s	solid grain bulk modulus	12.445	MN/m^2
B	Skempton coefficient	0.8	
ν_u	undrained Poisson's ratio	0.4	
σ_z	loading stress	1.0	MN/m^2

finite element model will be compared with those obtained from the finite difference model.

The height, length and width of the column are 4 m, 4 m and 1 m, respectively. In the finite element layout, 20 block-type elements with 84 nodes are used. The basic boundary and initial conditions are identical to the previous case. For the two-phase fluid flow problem, some additional conditions need to be included in the calculations.

- The initial water and oil saturations are assumed to be 0.35 and 0.65 for the single porosity system and the dual-porosity system;
- The relative permeability and water saturation relationship is achieved via statistical analyses (least square) of the data. With reference to Mattax and Dalton (1990), the following empirical relationships were used in the calculations:

$$\begin{cases} k_{ro} = 1.9673S_w^3 - 1.3585S_w^2 - 1.8094S_w + 1.3031 \\ k_{rw} = 1.9552S_w^3 - 1.1725S_w^2 + 0.2329S_w - 0.0151 \end{cases} \tag{4.11}$$

These relationships have been graphically represented by Figure 2.3.

- The capillary pressure and water saturation relationship is given from the referenced curves described by Dagger (1997), which can be expressed as:

$$P_{cw} = \frac{13.159 - 10.8459 S_w}{1 + 3.6262 S_w} \times 6.98 \times 10^{-3} \ (MPa) \qquad (4.12)$$

This relationship is designed for the imbibition process, which is schematically shown in Figure 4.10. In general, the capillary pressures in the matrix and fracture systems are not equal to each other. The matrix capillary pressure is generally greater than the fracture capillary pressure (Kazemi *et al.*, 1975). However, an identical capillary pressure is used in both matrix and fracture systems in this validation problem (Nakornthap *et al.*, 1986).

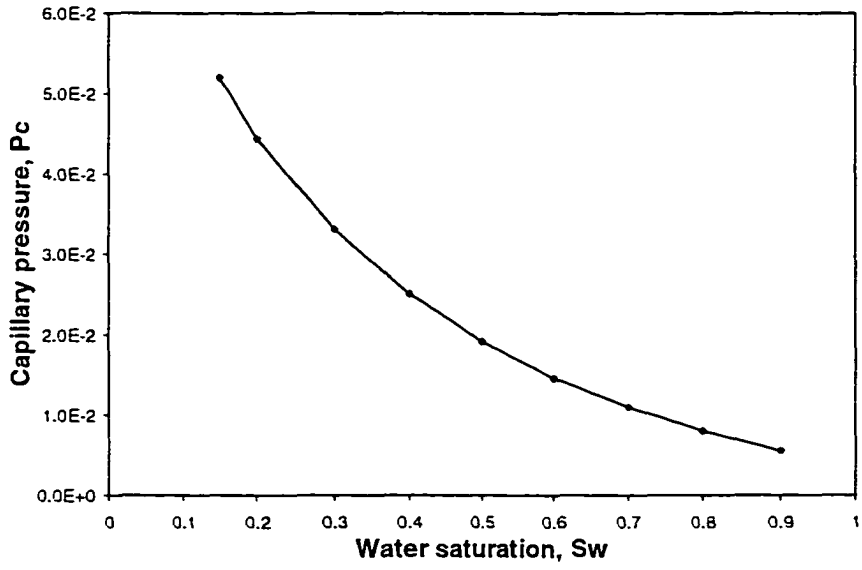

Figure 4.10: Water saturation with capillary pressure.

Other related parameters used in the calculation are listed in Table 4.4.

The results obtained from the present finite element code are shown in Figures 4.11 through 4.14 for the dual-porosity two-phase flow case. Those figures show

Table 4.4: Parameters used in two-phase validation.

Parameter	Definition	Magnitude	Units
E	modulus of elasticity	3000.0	MN/m^2
ν	Poisson's ratio	0.2	
α_1	Biot coefficient	0.861	
α_2		0.722	
K_n	normal fracture stiffness	30000.0	$MN/m^2/m$
K_f	fluid bulk modulus	3000.0	MN/m^2
ϕ_1	matrix porosity	0.2	
ϕ_2	fracture porosity	0.05	
$k_1/\mu_w, k_1/\mu_o$	matrix mobility	9.87E-6, 6.58E-6	$m^4/(MN{\cdot}s)$
$k_2/\mu_w, k_2/\mu_o$	fracture mobility	9.87E-4, 6.58E-4	$m^4/(MN{\cdot}s)$
s	fracture spacing	0.2	m
K_s	solid grain bulk modulus	12000.0	MN/m^2
σ_z	loading stress	2.0	MN/m^2

the comparison of the non-linear results for the tested soil column obtained from the present finite element model and those presented by the finite difference model of Shu (1998). Figure 4.11 demonstrates the changes of surface subsidence with time. The results obtained show the same trends for the two models. The largest differences occur only at the early time between these two methods. This may be caused by the methods used to solve the partial differential equations in the finite element and the finite difference approaches. The implicit method is used in the finite element approach, while the explicit method is applied for the finite difference.

The pressure changes near the column top (5% distance in the total height) and at the bottom of the column for the matrix and the fracture are illustrated in Figures 4.12 and 4.13. The pressures at the bottom of the column are larger than that at top surface. This can be rationalized by the fact that the bottom stays in no-flow conditions and the top surface is drained. Also this figure shows that the pressures change faster in the fracture than in the matrix. In other words, the pressure in the

matrix has a higher value than the pressure in the fracture; inducing fluid flow from the matrix to the fracture. The difference between oil pressure and water pressure is actually the capillary pressure. The results from both models match well.

Figure 4.14 shows the water saturation changes at the surface and bottom of the column. The water saturations increase in both the matrix and the fracture systems in early times which indicates more oil comes out of the column than water. Later, the water saturations maintain a constant value. It can be seen that both finite element and finite difference model predictions are identical; indicating the validity of the present dual-porosity two-phase program code.

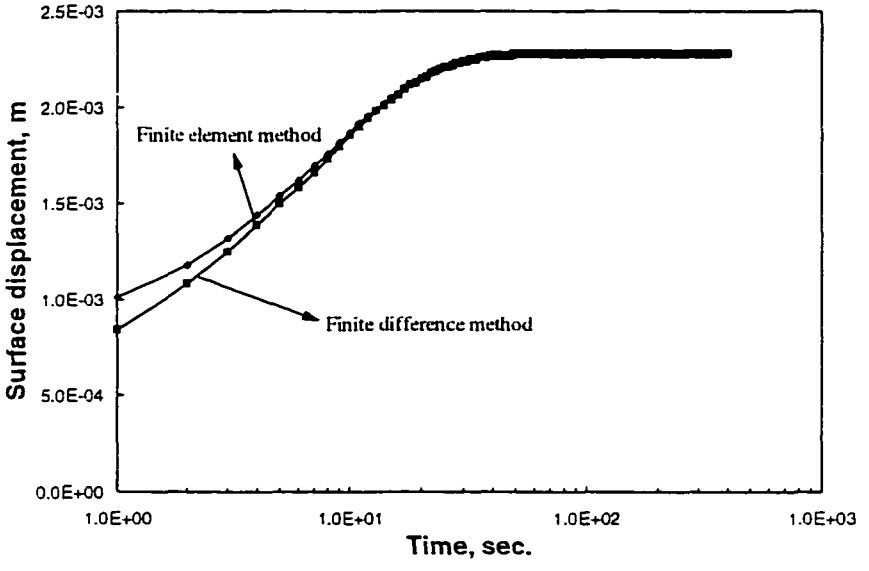

Figure 4.11: Surface subsidence with time.

It is clear that the developed finite element model has passed all the tested examples. Those results indicate the validity and the capability of the model for simulating two-phase flow coupled with solid deformations in fractured media in three dimensions. In the next Chapter, different kinds of coupling problems will be solved using the dual-porosity two-phase finite element model. Those problems

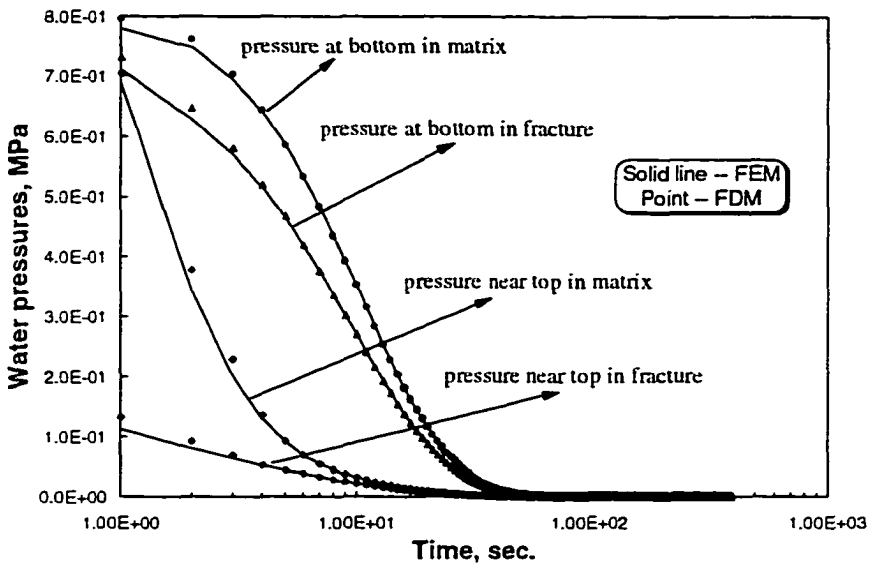

Figure 4.12: Water pressure changes near the top and at the bottom.

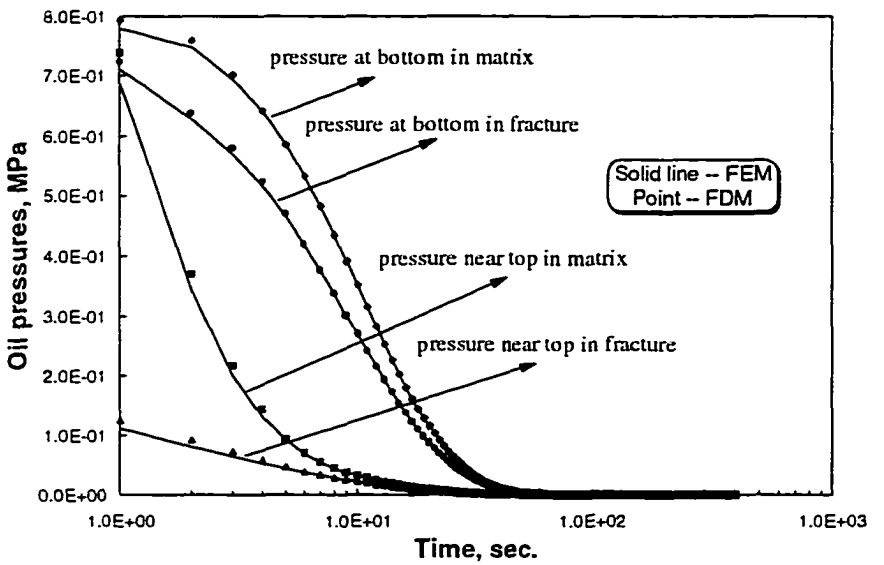

Figure 4.13: Oil pressure change near the top and at the bottom.

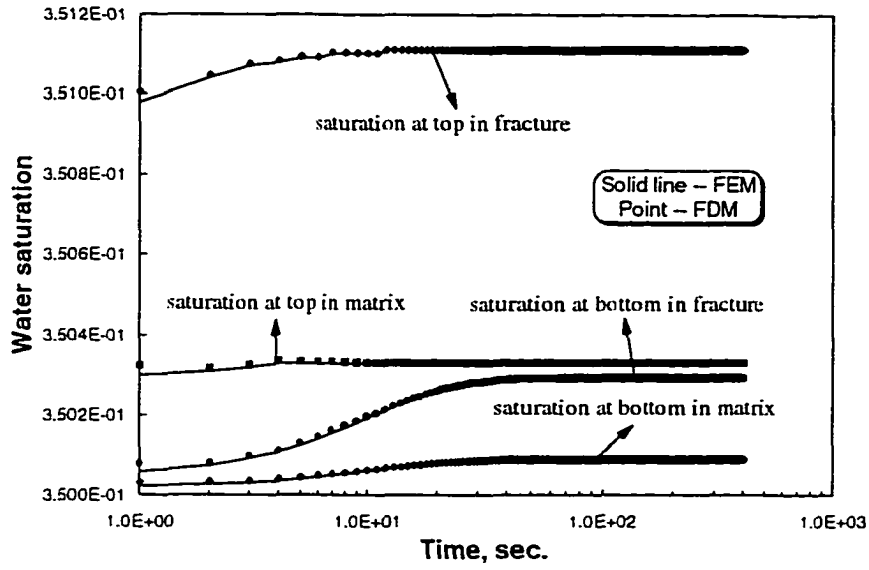

Figure 4.14: Water saturation changes at the top and the bottom.

include pure elastic, steady-state flow, single-porosity single-phase, single-porosity two-phase, dual-porosity single-phase and parametric studies.

Chapter 5

Parametric Analyses

The developed model and the program can be easily used for other problems which include pure elasticity, steady-state flow, single-porosity single-phase, single-porosity two-phase, dual-porosity single-phase and dual-porosity two-phase problems.

At first, the different kinds of problems will be discussed and the related formulations will also be given. Those formulations are derived from Equations (2.42) and (2.61) which are the basic equations for the coupling problems of solid deformations and two-phase fluid flow (water and oil) under the dual-porosity concept. Later, some examples will be given to demonstrate how the code works and to show the obvious differences in the results.

5.1 Pure Elasticity and Steady-state Flow

Although the numerical results of pure elasticity and steady-state flow have been validated in the previous Chapter, the basic concepts and related formulations are given in this Section.

For the pure elastic problems, some parts in Equation (3.26) should be modified due to:

1. fluid pressures have no influence on the solid media;

2. no time effect; and,

3. no fracture effect, which means the solid material is single-porosity homogeneous media.

For the steady-state flow problem, the following items need to be considered in order to use Equation (3.26):

1. no time effect;

2. no fracture influence;

3. the solid material is an homogeneous media;

4. no fluid exchange between rock matrix and fracture;

5. single-phase fluid flow; and,

6. no volumetric strain effect on the fluid flow.

Under all the above assumptions, the matrix (3.26) can be written as:

$$\begin{bmatrix} \mathbf{K}_1 & 0 & 0 & 0 & 0 \\ 0 & \mathbf{W}_{1w} & 0 & 0 & 0 \\ 0 & 0 & 0 & 0 & 0 \\ 0 & 0 & 0 & 0 & 0 \\ 0 & 0 & 0 & 0 & 0 \end{bmatrix} \begin{bmatrix} \mathbf{u} \\ \mathbf{P}_{1w} \\ \mathbf{P}_{1o} \\ \mathbf{P}_{2w} \\ \mathbf{P}_{2o} \end{bmatrix} = \begin{bmatrix} f \\ \mathbf{Q}_{1w} \\ 0 \\ 0 \\ 0 \end{bmatrix} \tag{5.1}$$

Equation (5.1) allows to solve the pure elastic and steady-state flow problems.

5.2 Single-porosity Single-phase

For the traditional single-porosity (no fracture) porous media, the developed model can also be used to simulate the coupled processes between the solid rock deformations and single-phase fluid flow.

On neglecting the contribution from the fracture fluid pressure, the fracture pressure term in the solid equilibrium equation disappears. But care has to be taken with the solid deformation effects on the fluid flow equations. Based on the single-porosity-single-phase concept, the following changes need to be considered:

1. no fracture influence on the porous media;
2. the fluid interchange between the rock matrix and the fractures does not exist; and,
3. single-phase fluid flow, which means the changes of capillary pressure, saturation, relative permeability have no effect on the final equations.

The case of single-phase fluid flowing at saturated conditions is considered here; thus Equation (3.26) can be further simplified. The related formulation is expressed as:

$$\frac{1}{\Delta t}\begin{bmatrix} \mathbf{K}_1 & \mathbf{L}_{1w} & 0 & 0 & 0 \\ \mathbf{K}_{1w} & \mathbf{W}_{1w}\Delta t + \mathbf{W}_{11} & 0 & 0 & 0 \\ 0 & 0 & 0 & 0 & 0 \\ 0 & 0 & 0 & 0 & 0 \\ 0 & 0 & 0 & 0 & 0 \end{bmatrix} \begin{bmatrix} \mathbf{u} \\ \mathbf{P}_{1w} \\ \mathbf{P}_{1o} \\ \mathbf{P}_{2w} \\ \mathbf{P}_{2o} \end{bmatrix}^{t+\Delta t} =$$

$$= \frac{1}{\Delta t}\begin{bmatrix} \mathbf{K}_1 & \mathbf{L}_{1w} & 0 & 0 & 0 \\ \mathbf{K}_{1w} & \mathbf{W}_{11} & 0 & 0 & 0 \\ 0 & 0 & 0 & 0 & 0 \\ 0 & 0 & 0 & 0 & 0 \\ 0 & 0 & 0 & 0 & 0 \end{bmatrix} \begin{bmatrix} \mathbf{u} \\ \mathbf{P}_{1w} \\ \mathbf{P}_{1o} \\ \mathbf{P}_{2w} \\ \mathbf{P}_{2o} \end{bmatrix}^{t} + \begin{bmatrix} \frac{df}{dt} \\ -\mathbf{Q}_{1w} \\ 0 \\ 0 \\ 0 \end{bmatrix}^{t+\Delta t} \tag{5.2}$$

It is noted that if $\mathbf{L}_{1w}$ and $\mathbf{K}_{1w}$ are equal zero, the solid deformations and the fluid flow are not coupled; and the solutions include two parts: one is the elastic solution and the other is the transient flow solution.

5.3 Single-porosity Two-phase

In the case of an immiscible two-phase fluid flow (water and oil) problem, more considerations should be given than what was mentioned in the previous Section. Those considerations include the influence of capillary pressure due to the pressure difference between two fluids, saturation changes because the pore space occupied by the fluid is changed and the relative permeability changes. Also the relations between capillary pressure and saturation, between relative permeability and saturation play a very important role in two-phase flow problems.

At this stage, the coefficients in the equations are dependent on the unknowns; hence, non-linearity is introduced.

Equation (3.26) will be modified according to the changes listed below:

1. no fracture influence on the porous media; and,
2. fluid interchanges between rock matrix and fracture do not exist for the two-phase fluids.

The coupled equations for solid deformation and two-phase fluid flow become:

$$\frac{1}{\Delta t}\begin{bmatrix} \mathbf{K}_1 & \mathbf{L}_{1w} & \mathbf{L}_{1o} & 0 & 0 \\ \mathbf{K}_{1w} & \mathbf{W}_{1w}\Delta t + \mathbf{W}_{11} & \mathbf{W}_{12} & 0 & 0 \\ \mathbf{K}_{1o} & \mathbf{W}_{21} & \mathbf{W}_{1o}\Delta t + \mathbf{W}_{22} & 0 & 0 \\ 0 & 0 & 0 & 0 & 0 \\ 0 & 0 & 0 & 0 & 0 \end{bmatrix} \begin{bmatrix} \mathbf{u} \\ \mathbf{P}_{1w} \\ \mathbf{P}_{1o} \\ \mathbf{P}_{2w} \\ \mathbf{P}_{2o} \end{bmatrix}^{t+\Delta t} =$$

$$= \frac{1}{\Delta t}\begin{bmatrix} \mathbf{K}_1 & \mathbf{L}_{1w} & \mathbf{L}_{1o} & 0 & 0 \\ \mathbf{K}_{1w} & \mathbf{W}_{11} & \mathbf{W}_{12} & 0 & 0 \\ \mathbf{K}_{1o} & \mathbf{W}_{21} & \mathbf{W}_{22} & 0 & 0 \\ 0 & 0 & 0 & 0 & 0 \\ 0 & 0 & 0 & 0 & 0 \end{bmatrix} \begin{bmatrix} \mathbf{u} \\ \mathbf{P}_{1w} \\ \mathbf{P}_{1o} \\ \mathbf{P}_{2w} \\ \mathbf{P}_{2o} \end{bmatrix}^{t} + \begin{bmatrix} \frac{df}{dt} \\ -\mathbf{Q}_{1w} \\ -\mathbf{Q}_{1o} \\ 0 \\ 0 \end{bmatrix}^{t+\Delta t} \tag{5.3}$$

Again if $\mathbf{L}_{1w}$, $\mathbf{L}_{1o}$, $\mathbf{K}_{1w}$ and $\mathbf{K}_{1o}$ are equal zero, the results represent both elastic and transient two-phase flow solutions.

5.4 Dual-porosity Single-phase

One method to represent the naturally fractured reservoirs is the dual-porosity approach. Many studies have been carried out using this concept in which different properties have been attributed to the pores and fissures: and this has proved to be a more reliable method when dealing with heterogeneous porous media.

Even for the single-phase fluid flow problem, there exist two fluid pressures in the reservoir: in the fractures and in the rock matrix. Thus, the solid rock deformations are affected not only by the loading conditions but also by those two fluid pressures.

For the fluid flow equations, one term will be added to the single-porosity single-phase problem to take into account the fluid interchange between the fractures and the matrix.

Equation (3.26) needs to ignore the effect of the capillary pressure, saturation and relative permeability because the problem is single-phase.

The finite element approximation will be obtained as follows:

$$\frac{1}{\Delta t}\begin{bmatrix} \mathbf{K}_1 & \mathbf{L}_{1w} & 0 & \mathbf{L}_{2w} & 0 \\ \mathbf{K}_{1w} & \mathbf{W}_{1w}\Delta t + \mathbf{W}_{11} & 0 & \mathbf{W}_{13} & 0 \\ 0 & 0 & 0 & 0 & 0 \\ \mathbf{K}_{2w} & \mathbf{W}_{31} & 0 & \mathbf{W}_{2w}\Delta t + \mathbf{W}_{33} & 0 \\ 0 & 0 & 0 & 0 & 0 \end{bmatrix}\begin{bmatrix} \mathbf{u} \\ \mathbf{P}_{1w} \\ \mathbf{P}_{1o} \\ \mathbf{P}_{2w} \\ \mathbf{P}_{2o} \end{bmatrix}^{t+\Delta t} =$$

$$= \frac{1}{\Delta t}\begin{bmatrix} \mathbf{K}_1 & \mathbf{L}_{1w} & 0 & \mathbf{L}_{2w} & 0 \\ \mathbf{K}_{1w} & \mathbf{W}_{11} & 0 & \mathbf{W}_{13} & 0 \\ 0 & 0 & 0 & 0 & 0 \\ \mathbf{K}_{2w} & \mathbf{W}_{31} & 0 & \mathbf{W}_{33} & 0 \\ 0 & 0 & 0 & 0 & 0 \end{bmatrix}\begin{bmatrix} \mathbf{u} \\ \mathbf{P}_{1w} \\ \mathbf{P}_{1o} \\ \mathbf{P}_{2w} \\ \mathbf{P}_{2o} \end{bmatrix}^{t} + \begin{bmatrix} \frac{df}{dt} \\ -\mathbf{Q}_{1w} \\ 0 \\ -\mathbf{Q}_{2w} \\ 0 \end{bmatrix}^{t+\Delta t} \tag{5.4}$$

As discussed in previous Sections, if $\mathbf{L}_{1w}$, $\mathbf{L}_{2w}$, $\mathbf{K}_{1w}$ and $\mathbf{K}_{2w}$ equal zero, the results will show both the elastic solution as well as the transient fluid flow solution in a dual-porosity system.

5.5 Dual-porosity Two-phase

The detailed formulations and physical explanations have been given in Chapters 2 and 3. The final coupled solid deformations and two-phase fluid flow (water and oil) equations are expressed in the finite element form shown in Equation (3.26). Differences from the previous Section are the introduction of capillary pressures, saturations and relative permeabilities effects. Also those capillary pressures, saturations and relative permeabilities exist in both the fractures and the matrix systems.

The following Section will show some results calculated for these different problems.

5.6 Examples

5.6.1 Single-phase for Single-porosity and Dual-porosity

A column loaded at the top surface (Figure 4.5) is considered as the first example. The height, length and width of the column are 7m, 2m and 1m, respectively. Twenty block-type elements and eighty-four nodes are used in this problem. The fluid pressures are equal to zero at the top surface; everywhere else, the surface of the column is assumed to be sealed and insulated.

Table 5.1 shows the material properties used in the example for both the single-porosity single-phase and the dual-porosity single-phase cases.

The column top surface settlement versus time is shown in Figure 5.1. It may be observed that for the dual-porosity model a more rapid surface displacement is predicted. Also Figure 5.2 demonstrates the fluid pressure changes at the bottom

Table 5.1: Parameters used in the example.

Parameter	Definition	Values (A* / B*)	Units
E	modulus of elasticity	3000.0 / 3000.0	MN/m^2
ν	Poisson's ratio	0.2 / 0.2	
α_1	Biot coefficient	0.861 / 0.861	
α_2		0.0 / 0.861	
K_n	normal fracture stiffness	40000.0 / 40000.0	$MN/m^2/m$
K_f	fluid bulk modulus	3000.0 / 3000.0	MN/m^2
ϕ_1	matrix porosity	0.2 / 0.2	
ϕ_2	fracture porosity	0.0 / 0.05	
k_1/μ	matrix mobility	9.87E-6 / 9.87E-6	$m^4/(MN{\cdot}s)$
k_2/μ	fracture mobility	0.0 / 9.87E-5	$m^4/(MN{\cdot}s)$
s	fracture spacing	1.0E10 / 0.3	m
K_s	solid grain bulk modulus	12000.0 / 12000.0	MN/m^2
σ_z	loading stress	0.2 / 0.2	MN/m^2

A*=Single-porosity single-phase case;
B*=Dual-porosity single-phase case.

of the column. Again the fluid pressures in the dual-porosity model changes faster than for the single-porosity model. This may be attributed to the presence of a fracture network within the porous medium which results in a more rapid drainage of the fluid and, consequently, a faster rate of pore pressure dissipation and surface settlement.

Figure 5.3 shows the displacements along the column for both the single- and dual-porosity methods at different times. Again the surface displacements from the dual-porosity approach are larger than the displacements from single-porosity at the same time. The pressure changes along the column are illustrated in Figure 5.4. It is shown again that the pressures along the column in the dual-porosity system changes faster than the pressures in the single-porosity system.

The physical characteristics of single- and dual-porosity models are essentially contrasting since, in dual-porosity, the fractures have low porosity and high permeability, whereas in both single- and dual-porosity the matrix shows high porosity

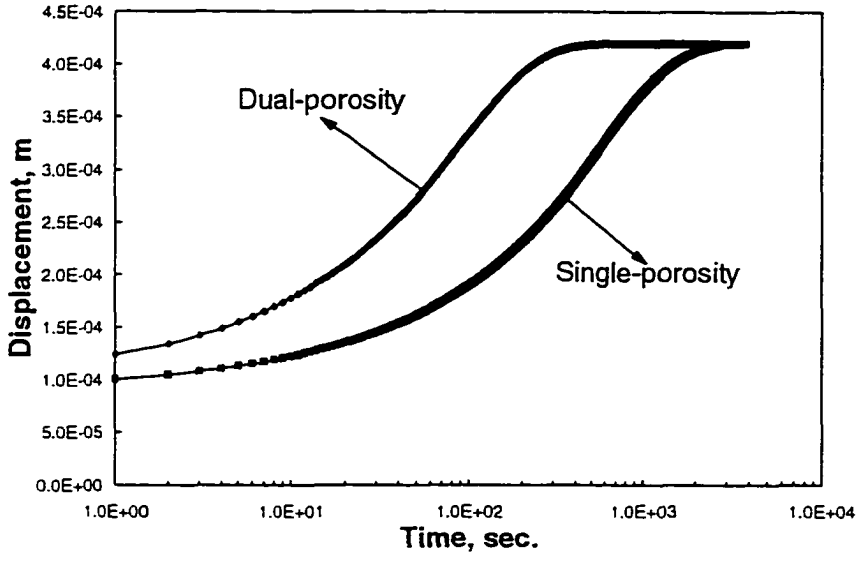

Figure 5.1: Surface displacement response for single- and dual-porosity approaches.

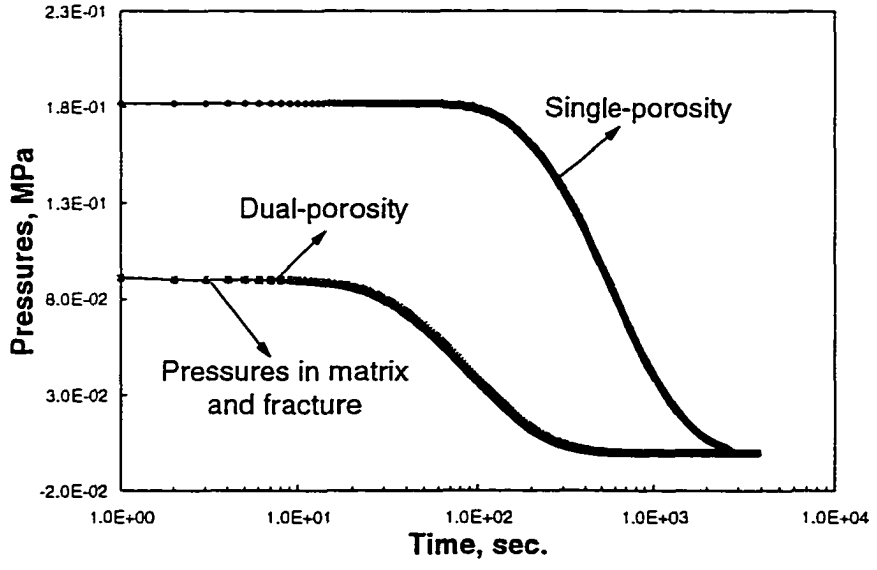

Figure 5.2: Pressure changes for single- dual-porosity approaches.

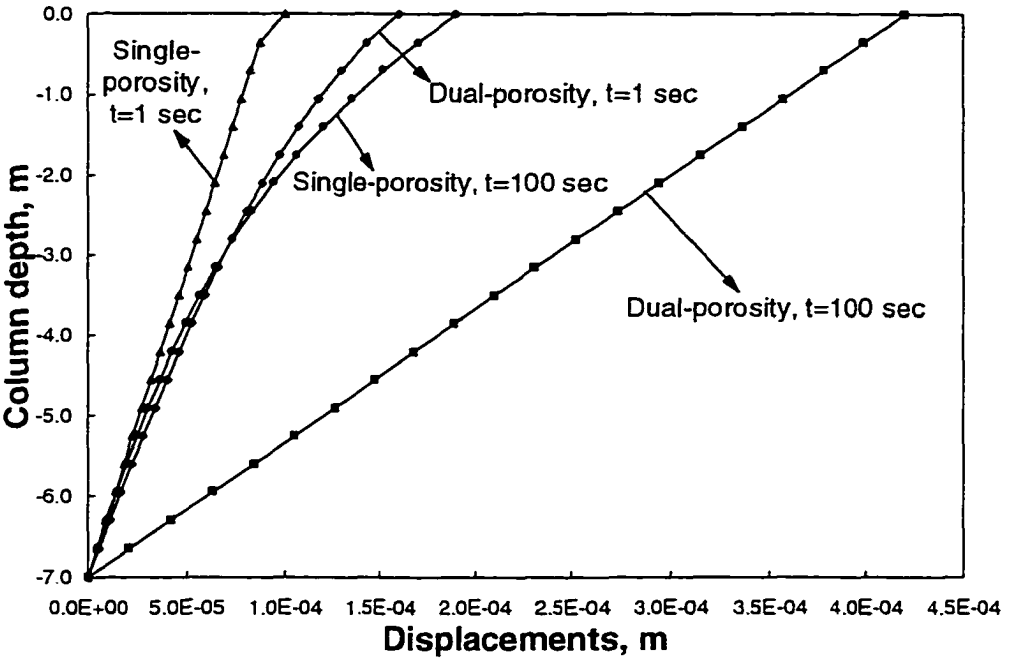

Figure 5.3: Displacements along the column.

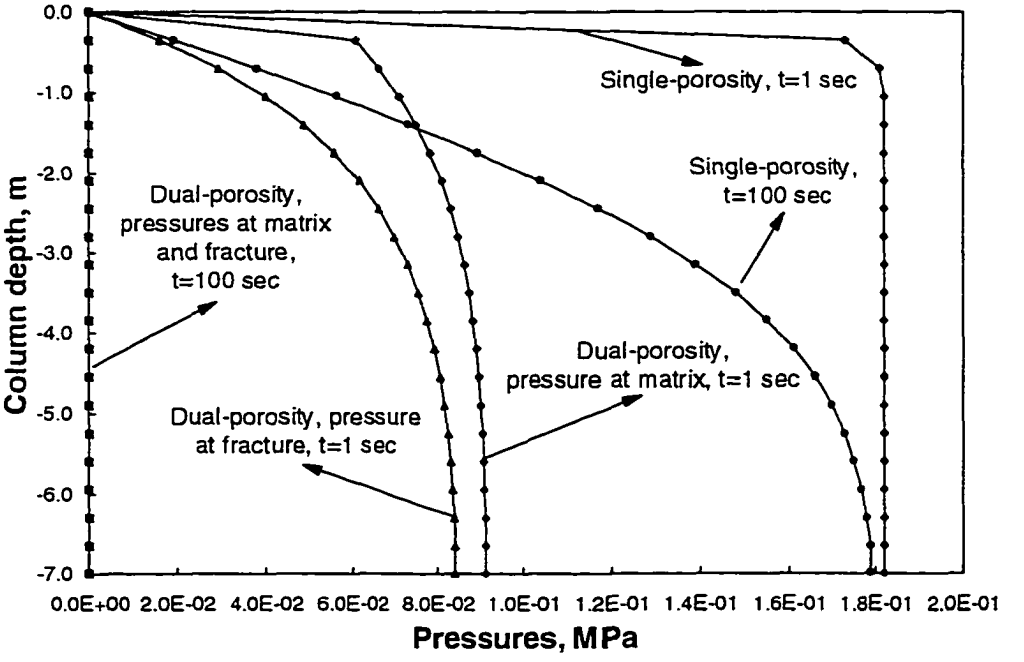

Figure 5.4: Pressure changes along the column.

and low permeability. As a result, in dynamic conditions, the fracture network will exhibit a small storage capacity, and thus, a very short transient time owing to its high permeability, whereas in single-porosity the matrix will exhibit a large storage capacity associated with a long transient time resulting from its low permeability.

Moreover, it may be observed that the final settlement and fluid pressures predicted by this model are precisely the same values for both dual-porosity and single-porosity approaches. Actually, the final settlements have the same values as that of the pure elastic solutions; while the final fluid pressures are equal to the values of the initial fluid pressures of the fractured porous medium.

Figure 5.5 depicts the top surface subsidence for different k_f/k_m ratios in which k_m, the rock matrix permeability, is kept constant and equal to 9.87E−6 $m^4/(MN \cdot s)$, while k_f, the fracture permeability, changes. As expected, the higher ratio will cause a more rapid consolidation. It is shown that the final values of the surface subsidence are the same for all permeability ratios. The bottom pressure changes are demonstrated in Figure 5.6. In this figure it is clear that the pressure drops faster for higher ratios k_f/k_m. Also Figure 5.6 shows that in fractured media the pressure is either higher in the matrix than in the fracture with higher ratio of k_f/k_m or closer in both systems with lower ratio of k_f/k_m, which means that more flow interchanges take place from the rock matrix to the fracture regions for higher k_f/k_m ratios. This will cause the fluid within the fractures to be depleted rapidly, especially with higher ratios k_f/k_m.

For highly fractured formations, a more rapid rate of the column top surface subsidence is indicated in Figure 5.7. Different fracture spacing values, $s^1 = 0.1$, 0.2 and 0.3 m, are considered in the calculations. Smaller values of spacing mean more fractures in the media and show faster consolidation rates. The behavior of

[1] Fracture spacing is defined as the distance between two parallel fractures of a fracture set.

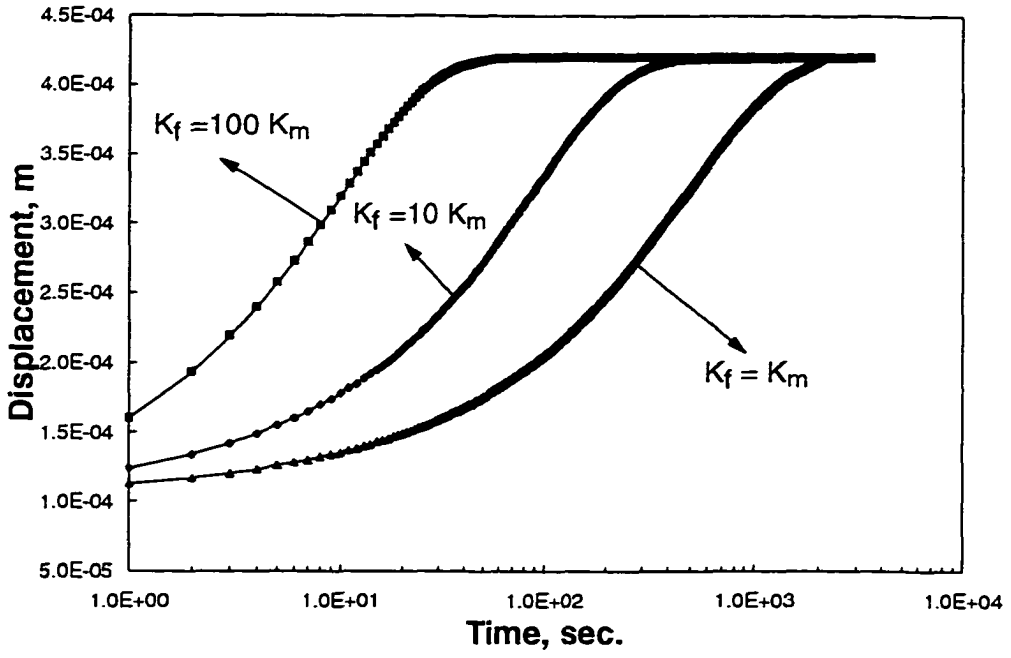

Figure 5.5: Surface subsidence for different fracture permeabilities.

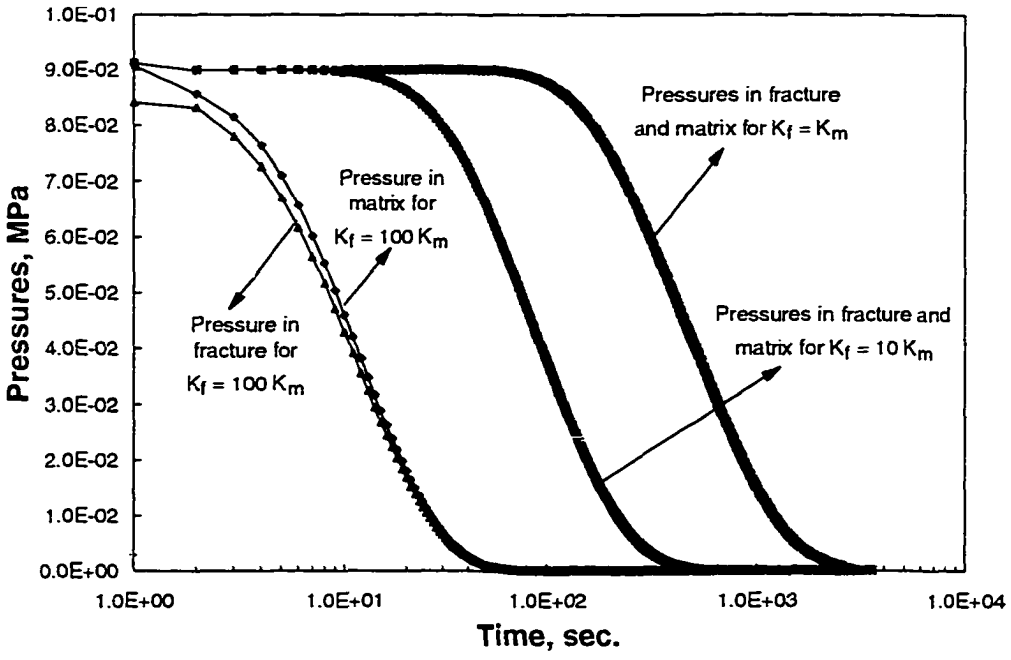

Figure 5.6: Bottom pressure for different fracture permeabilities.

bottom fluid pressures is displayed in Figures 5.8 and 5.9. It may be noted that at early times the pressures in both matrix and fracture systems with smaller fracture spacing values are higher; while at later times, this situation is reversed because with smaller spacing values (i.e. more fractures) the permeability per unit volume is higher, then the fluid will be rapidly depleted.

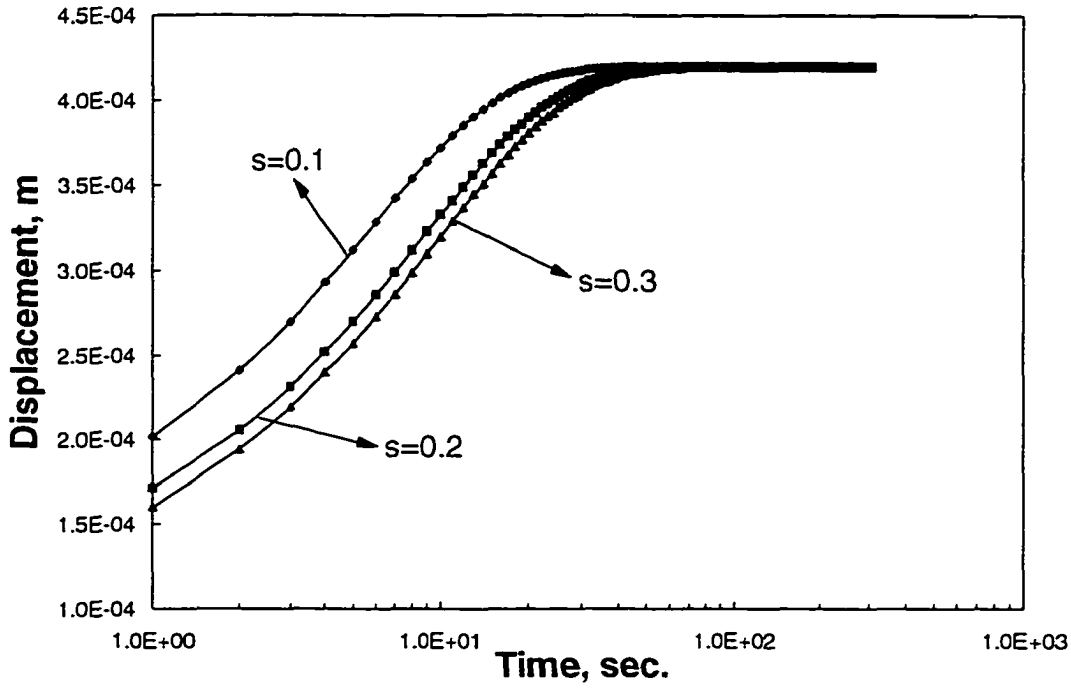

Figure 5.7: Surface subsidence for different fracture spacings.

5.6.2 Two-phase for Single- and Dual-porosity

Using the same example as shown in the previous Section with similar boundary and initial conditions, the relationship between the relative permeability and water saturation is obtained using Equation (4.11), and shown in Figure 2.3. The relationship between the capillary pressure and the water saturation is expressed by Equation (4.12), which is represented in Figure 4.5. Other related parameters used in the calculation are listed in Table 5.2.

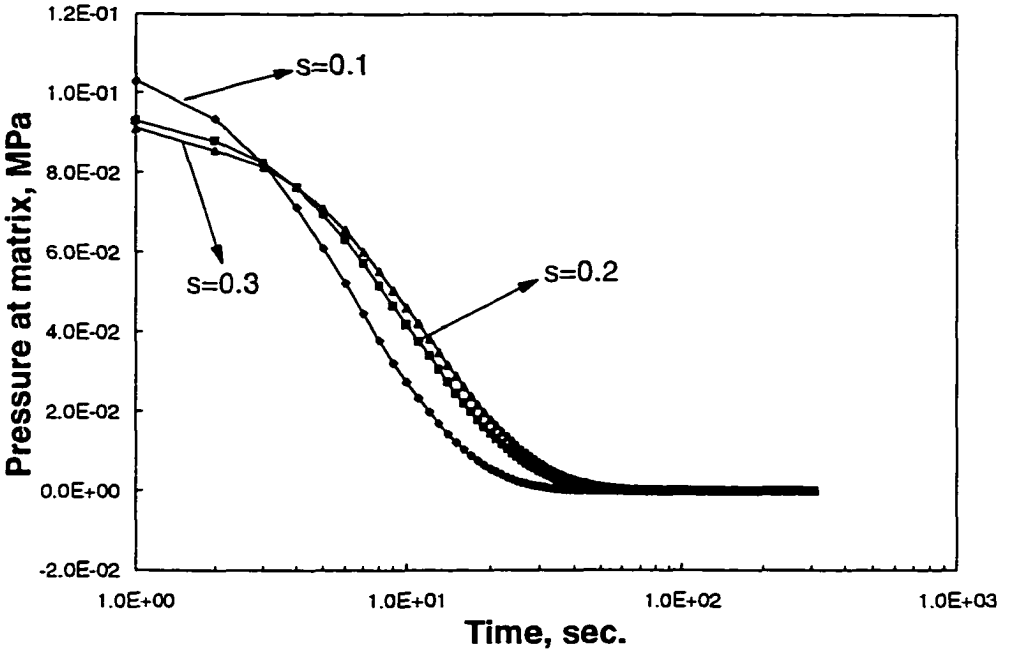

Figure 5.8: Bottom matrix pressures for different fracture spacings.

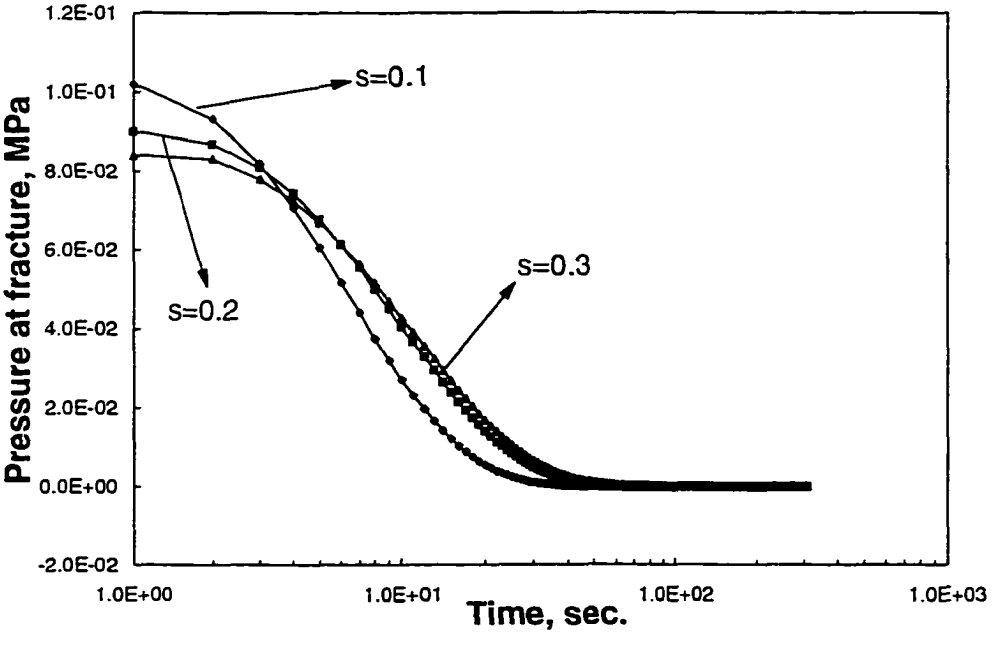

Figure 5.9: Bottom fracture pressures for different fracture spacings.

Figure 5.10 demonstrates the changes of surface subsidence with time for both single- and dual-porosity systems under two-phase fluid flow conditions. It is observed that for the dual-porosity model a more rapid surface subsidence occurred. This behavior is similar to what was discussed in Section 6.1 due to the presence of a fracture network within the porous medium.

Figure 5.11 shows the fluid pressure changes at the bottom of the column. Again the water and oil pressures in a dual-porosity system change faster than the pressures in a single-porosity system.

The water saturation changes at the column bottom and at the top surface are illustrated in Figures 5.12 and 5.13. It is shown that, at the bottom, saturations change faster for the dual-porosity system, especially at early times, compared to the single-porosity system, which is relative stable in the early time and only changes at later times. Also in the dual-porosity system, the saturation changes in the fractures are faster than the saturation changes in the matrix. At the top surface, the saturation values change a little with higher values in the fractures. The water saturation values increase in both surface and bottom of the column, which means more oil moves out of the column than water.

Table 5.2: Parameters used in two-phase case.

Parameter	Definition	Values (A* / B*)	Units
E	modulus of elasticity	3000.0 / 3000.0	MN/m^2
ν	Poisson's ratio	0.2 / 0.2	
α_1	Biot coefficient	0.861 / 0.861	
α_2		0.0 / 0.815	
K_n	normal shear fracture stiffness	30000.0 / 30000.0	$MN/m^2/m$
K_f	fluid bulk modulus	3000.0 / 3000.0	MN/m^2
ϕ_1	matrix porosity	0.2 / 0.2	
ϕ_2	fracture porosity	0.0 / 0.05	
k_1/μ_w	matrix water mobility	9.87E-6 / 9.87E-6	$m^4/(MN \cdot s)$
k_1/μ_o	matrix oil mobility	0.0 / 6.58E-6	$m^4/(MN \cdot s)$
k_2/μ_w	fracture water mobility	9.87E-4 / 9.87E-4	$m^4/(MN \cdot s)$
k_2/μ_o	fracture oil mobility	0.0 / 6.58E-4	$m^4/(MN \cdot s)$
s	fracture spacing	1.0E10 / 0.3	m
K_s	solid grain bulk modulus	12000.0 / 12000.0	MN/m^2
σ_z	loading stress	0.2 / 0.2	MN/m^2

A*=Single-porosity two-phase case;
B*=Dual-porosity two-phase case.

For the analysis of the capillary pressure influence, two different sets of capillary pressure data were used in the calculations of the dual-porosity system. Those data are expressed in the following equations and graphically represented by Figure 5.14 (Dagger, 1997).

$$\begin{cases} P_c^1 = \dfrac{13.159 - 10.8459 S_w}{1 + 3.6262 S_w} \times 6.98 \times 10^{-3} (MPa) \\ P_c^2 = \dfrac{8.0 - 6.1 S_w}{1 + 2.6262 S_w} \times 6.98 \times 10^{-3} (MPa) \end{cases} \tag{5.5}$$

where superscripts 1 and 2 represent first and second capillary pressure data, respectively.

The surface subsidences for both cases are plotted in Figure 5.15. Same trends are observed for the two cases, except the displacement values for case 1 is slightly higher.

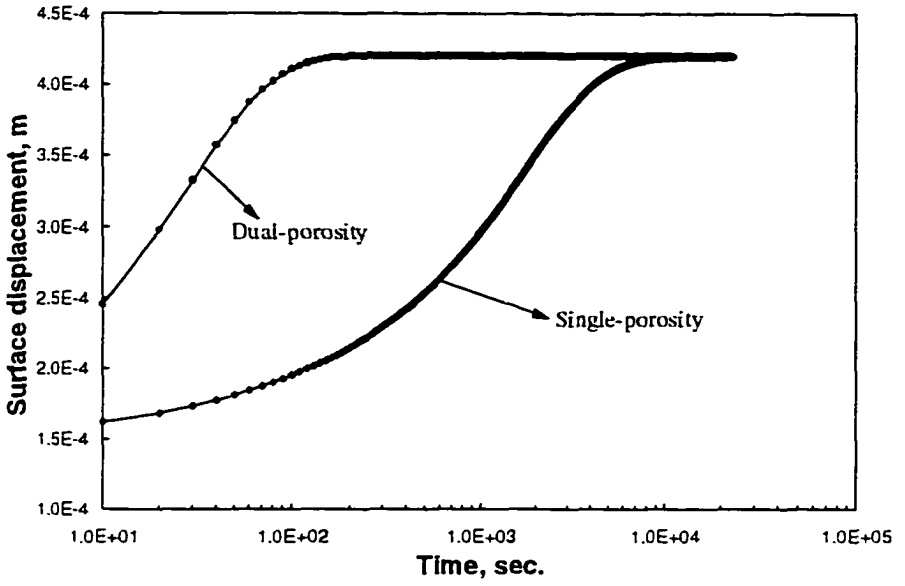

Figure 5.10: Surface subsidence with time.

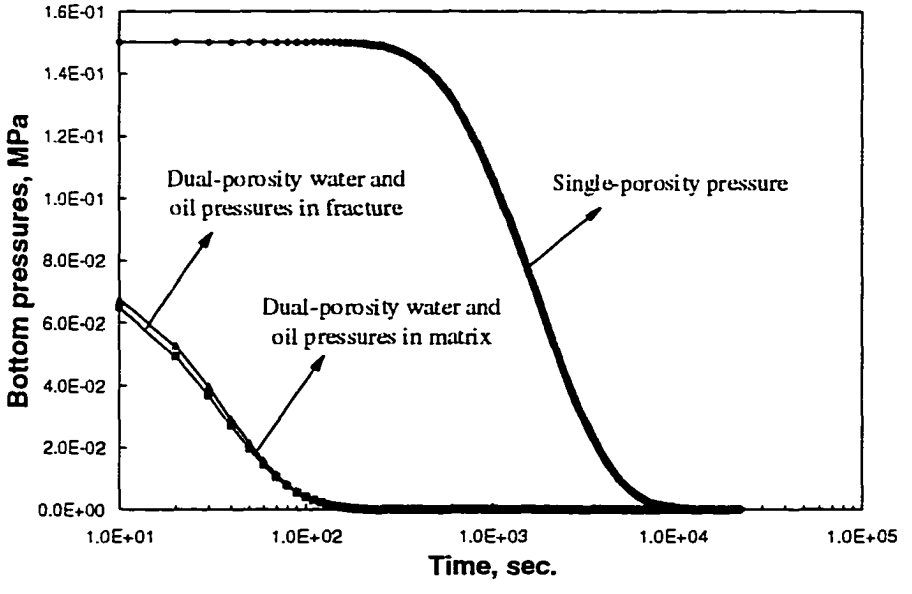

Figure 5.11: Bottom pressure changes with time.

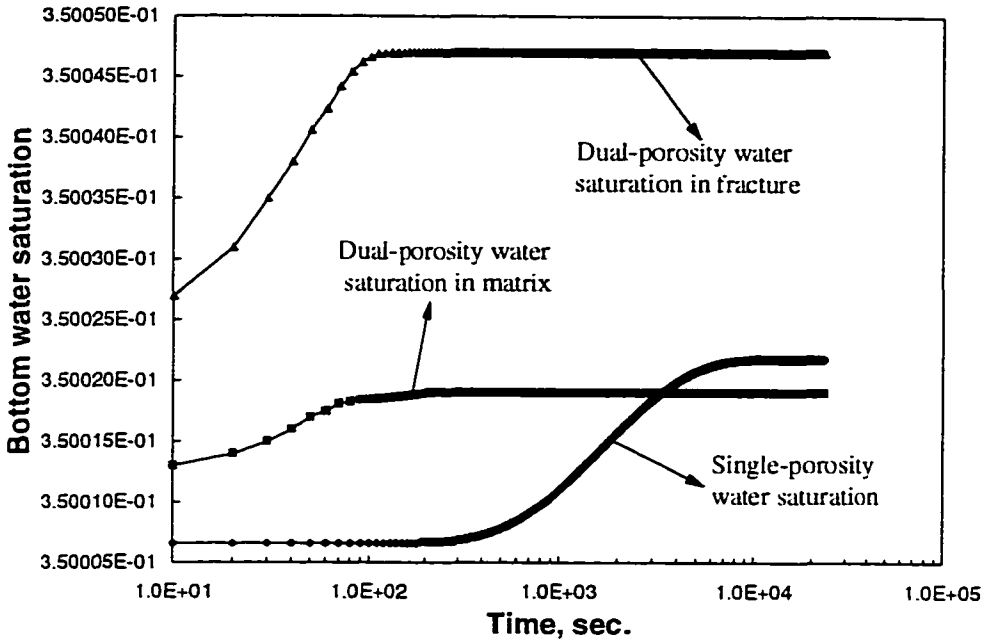

Figure 5.12: Water saturation change at the bottom with time.

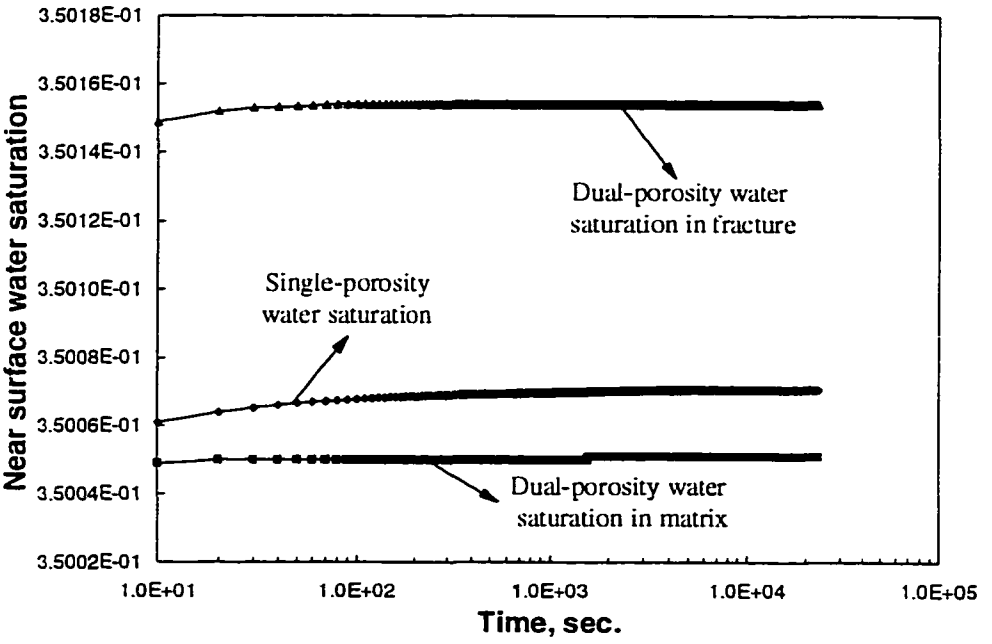

Figure 5.13: Water saturation changes at the surface with time.

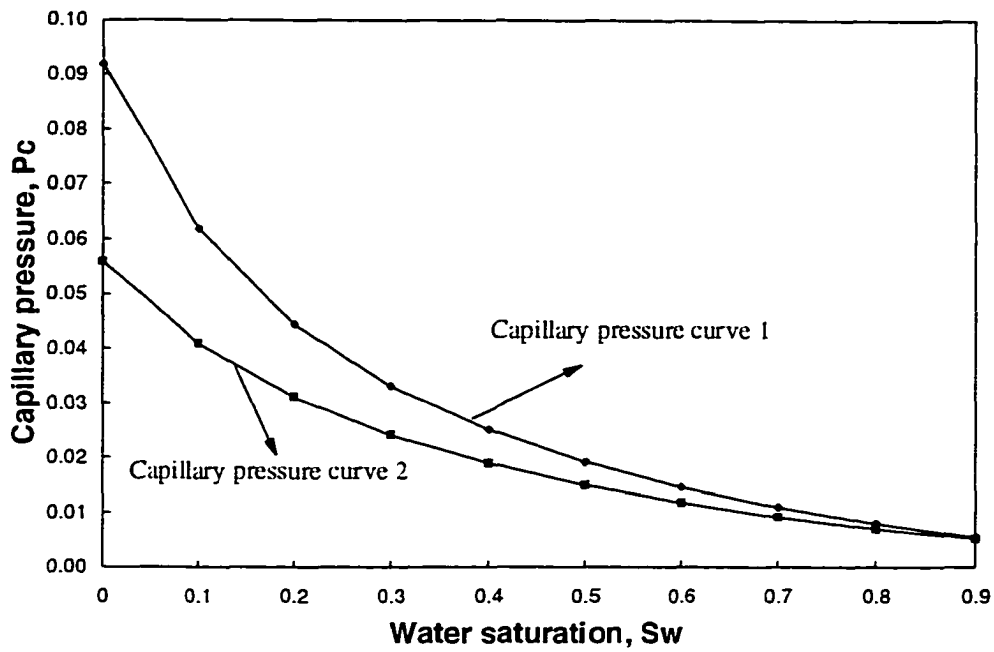

Figure 5.14: Water saturation with two sets of capillary pressures.

Figure 5.16 shows the water saturation changes at the bottom of the column. The changes of water saturation in the fracture are faster than in the matrix for both cases. Figure 5.17 represents the water saturation changes near the surface of the column (5% distance in the total height) and shows the same behavior compared to the saturation changes at the bottom. After passing the transition period, the values of the water saturations remain stable at the bottom and near the top surface of the column. For both the fracture and the matrix, the saturation values keep higher for capillary pressure case 2.

The water and oil pressure changes near the column top and at the bottom of the column for the matrix and fracture are illustrated in Figures 5.18, 5.19, 5.20 and 5.21. The pressures at the bottom of the column are larger than that near the top surface because the bottom remains undrained, causing the pressures at the bottom

to reach higher values. Also those figures show that the pressures in the matrix have a higher value than the values of the pressure in the fractures. The effects of the capillary pressure are limited for the pressure changes. For case 1 and case 2 of the capillary pressures, the pressure changes are very close to each other.

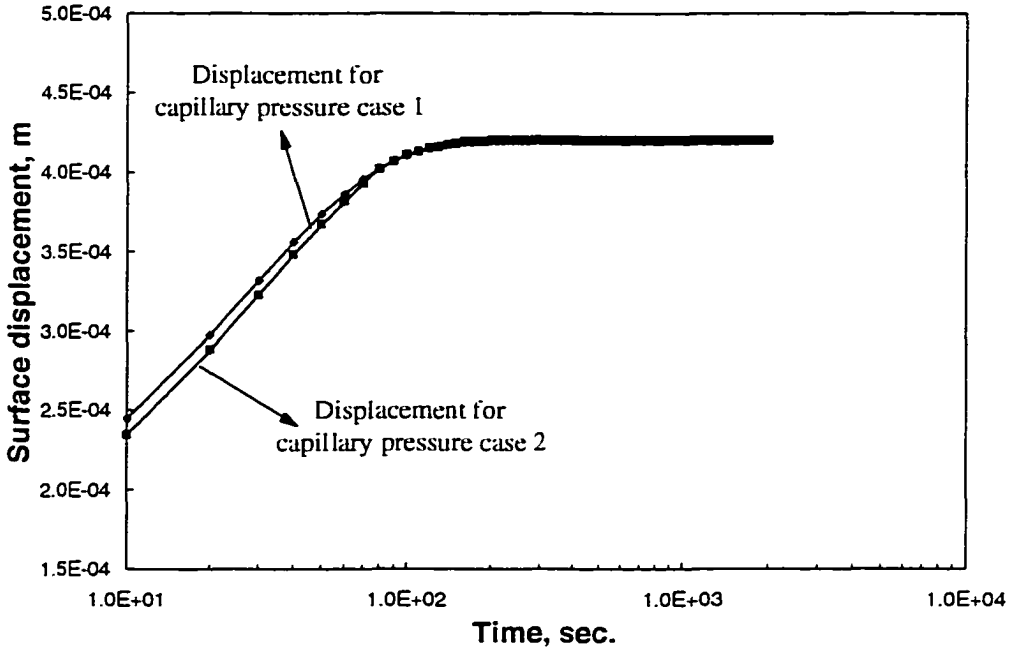

Figure 5.15: Surface subsidence with time for different capillary pressures.

Next Chapter will show the applications using this dual-porosity model to simulate the single- or two-phase flow problems in the laboratory.

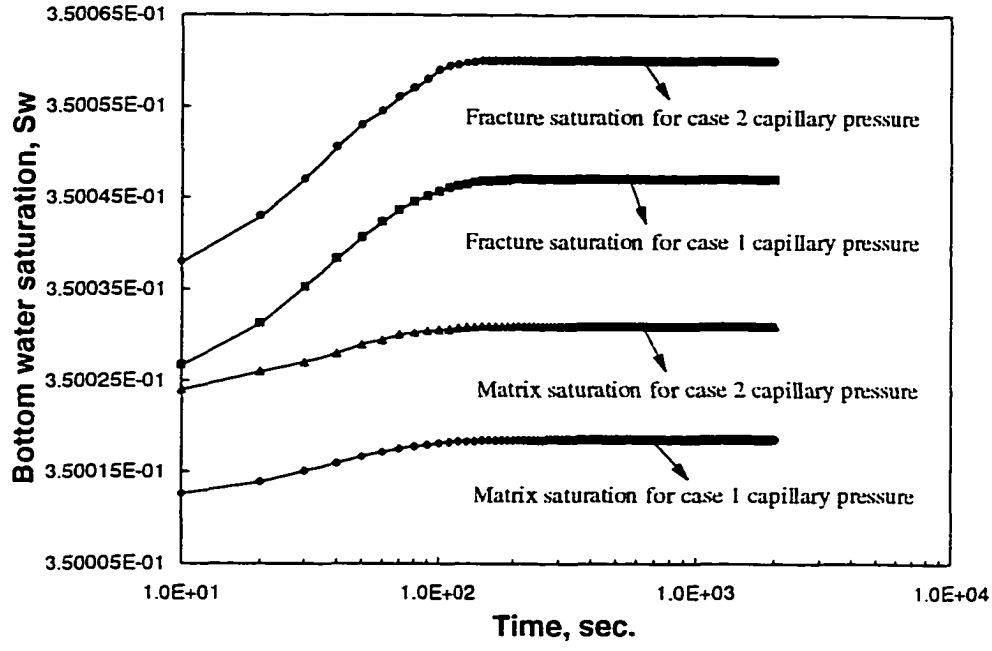

Figure 5.16: Saturation at bottom with time.

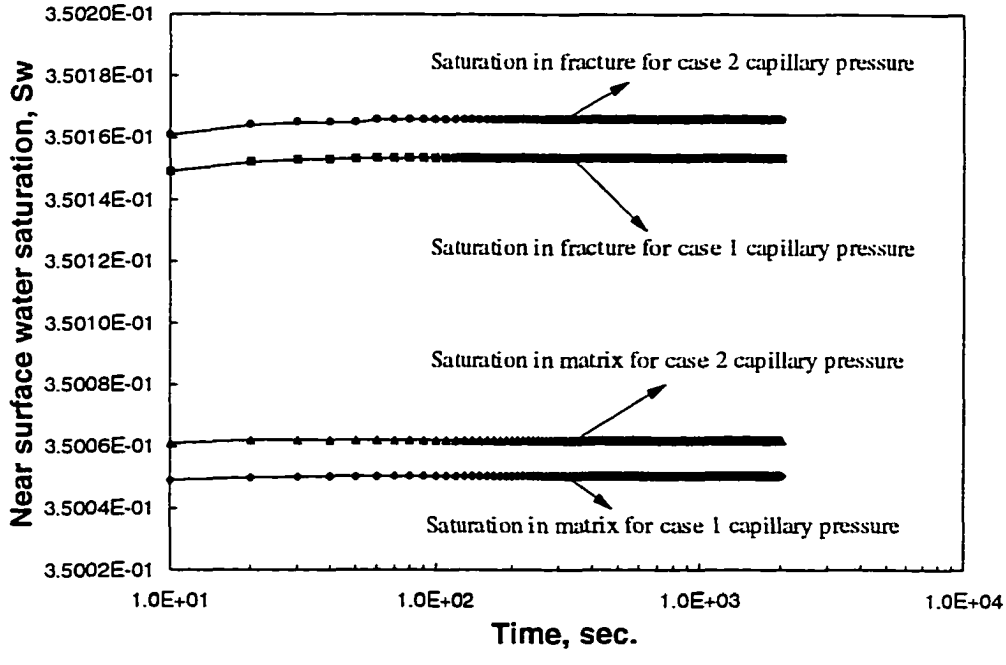

Figure 5.17: Saturations near surface with time.

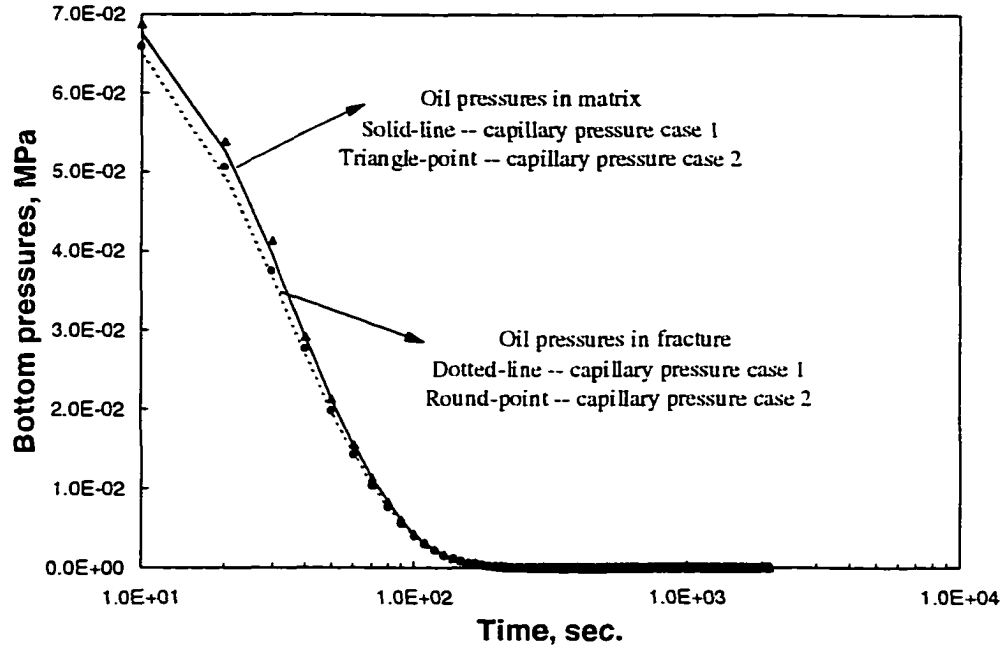

Figure 5.18: Oil pressures at bottom with time.

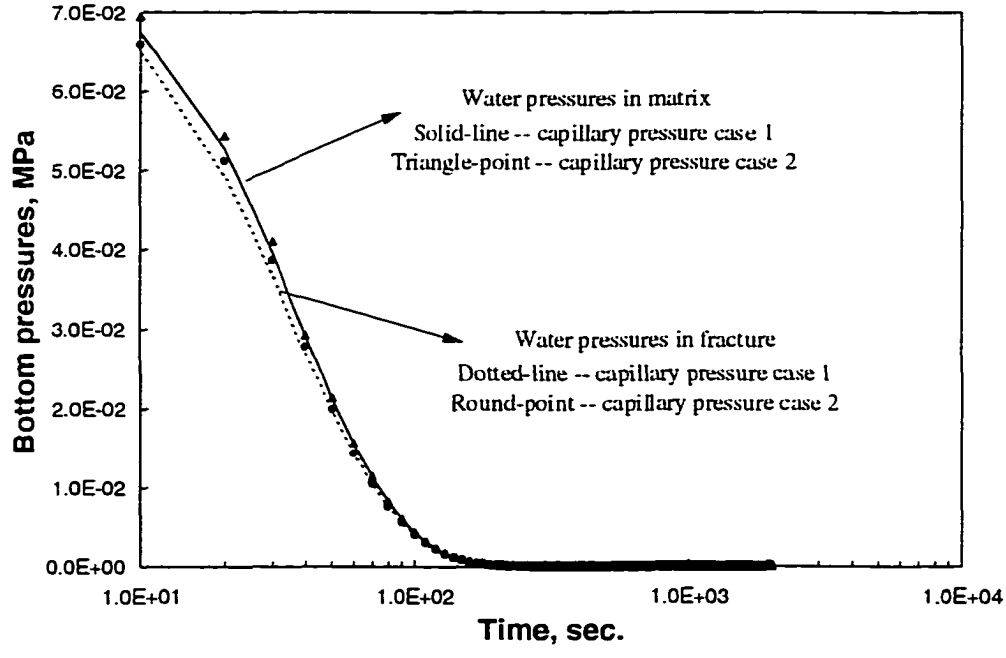

Figure 5.19: Water pressures at bottom with time.

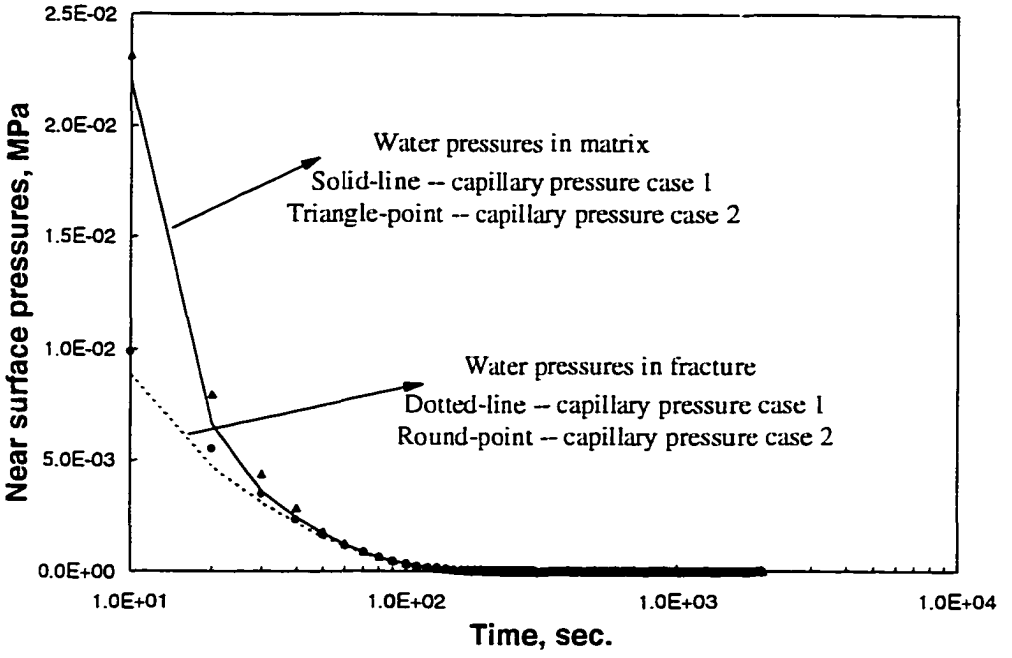

Figure 5.20: Water pressures near surface with time.

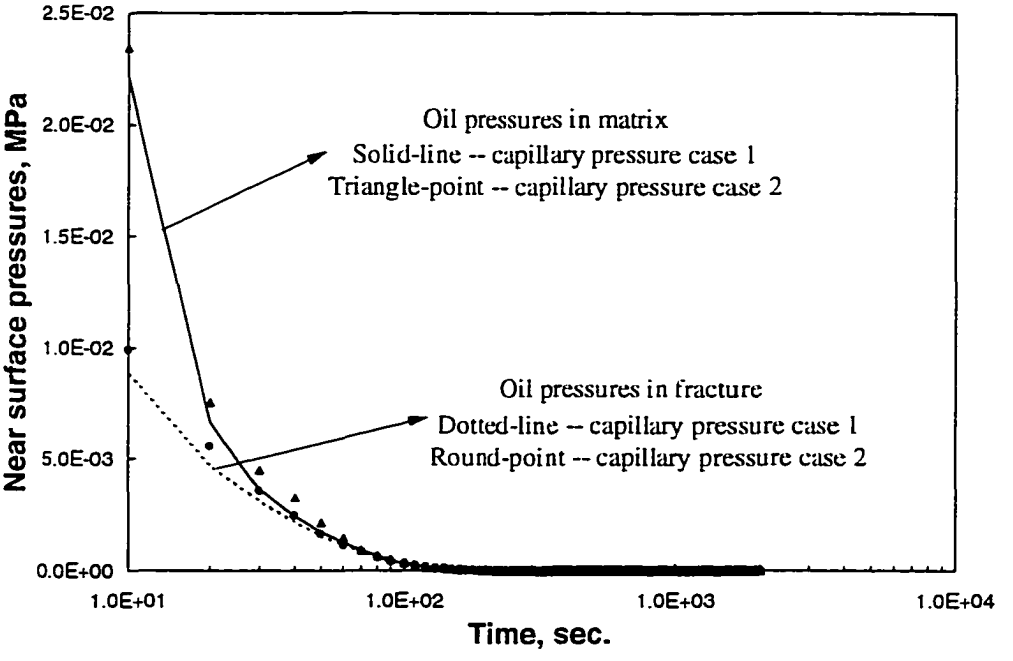

Figure 5.21: Oil pressures near surface with time.

Chapter 6

Model Applications

The capabilities of the finite element model have been demonstrated in several problems presented in the previous Chapters. For practical purposes, the model is used here to simulate the behavior of a rock sample which may be tested in the laboratory in an attempt to measure the fluid flow, permeability and rock properties.

The developed model may also be used to predict fluid flow behavior and to study the effect of anisotropic permeability. In addition, the present work is capable of studying the intact rock and fractured rock characteristics under single- or two-phase fluid flow conditions.

6.1 Laboratory Tests

Because of the direct relationship with production rate, the study of formation permeability is of great concern to petroleum engineers. In the cases of intact and fractured media, the permeabilities should be considered as stress-dependent in response to stress variations.

During fluid injection/withdrawal, various stress states occur ranging from compression to tension. These induced stresses cause the joints or fractures to open or close which in turn strongly affects the magnitude of the permeability.

The rock sample permeability can be measured in the laboratory. In general,

laboratory permeability tests are performed based on constant head (Al-Dhahir and Tan, 1968), transient or pulse-decay (Brace *et al.*, 1968) and constant flowrate (Morin and Olsen, 1987) methods. During such tests, either flowrate or pressure can be controlled at the injection point. While, at the observation point, either pressure or flowrate may be measured. It is assumed that the sample is fully jacketed except at the injection and observation points.

There are two methods to obtain the relative permeability. One method relies on analytical expressions which must be determined experimentally. Another possibility is to determine the relative permeability directly via laboratory experiments.

Two types of laboratory experiments are used for the determination of relative permeability: steady flow experiments and unsteady flow experiments (Bear, 1988). The most commonly used methods are based on steady flow. The tested sample, or core, is mounted either in a plexiglass tube or in a pressurized rubber sleeve, and a steady flow of the two fluids is established through it. The two fluids used in the experiment are introduced simultaneously at the inflow end, at a certain ratio, through separate piping systems. When steady flow conditions are reached, the pressures in the two fluids at either end of the sample, the rates of flow and the saturation are determined. The relative permeability corresponding to this saturation state can then be calculated. The injected ratio is then increased, removing more of the wetting phase, until once again steady state conditions are established. The process is repeated until a complete relative permeability curve is obtained (Bear, 1988).

6.2 Finite Element Scheme

Fluid flow through rock samples can be simulated by using the developed finite element model. Figure 6.1 shows a configuration used for measuring the horizontal rock permeability in the laboratory. The cylindrical sample is 0.2 m in height and

0.1 m in diameter. Vertical permeability can also be measured through the vertical injection.

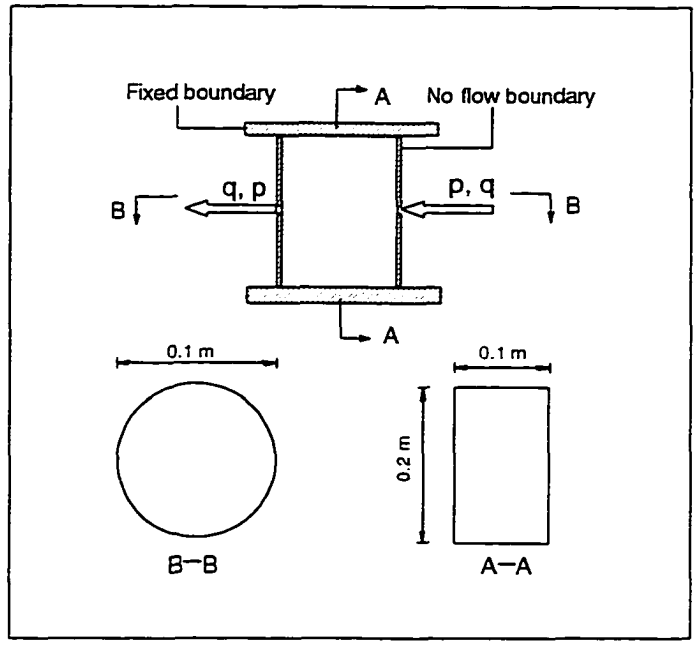

Figure 6.1: Rock sample configuration.

The finite element mesh arrangement is depicted in Figure 6.2. Because of the symmetries of the sample geometry, boundary conditions and applied flow rate or pressure conditions, the calculation needs only to be carried out in half of the sample. A total of four layers are considered in the vertical direction, 42 elements and 54 nodes in each horizontal plane. Eight-node isoparametric elements are used in this study case. The total nodal and element numbers are 270 and 168, respectively.

The boundary and initial conditions used in the cylindrical sample are as follows:

(a). displacement boundaries

$$\begin{cases} u_x(x,y,0,t) = u_y(x,y,0,t) = u_z(x,y,0,t) = 0 \\ u_x(x,y,-0.2,t) = u_y(x,y,-0.2,t) = u_z(x,y,-0.2,t) = 0 \\ u_y(x,0,z,t) = 0 \end{cases} \tag{6.1}$$

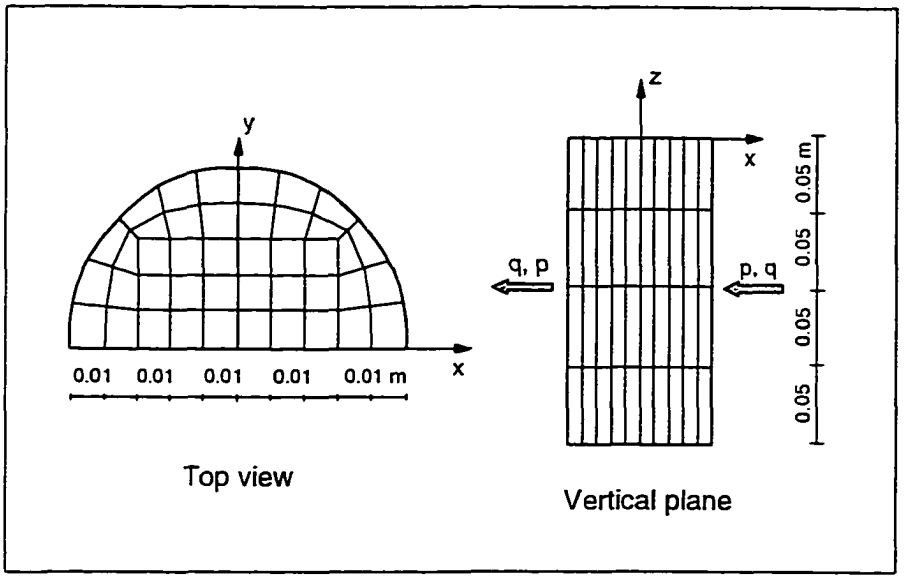

Figure 6.2: Mesh view in both horizontal and vertical planes.

(b). flow boundaries

No flow is allowed through the sample boundaries, except at the injection and withdrawal points.

(c). initial conditions

Fluid pressures are set to zero at $t = 0$. For the two-phase flow case, the initial water saturations are $S_w = 0.35$ and $S_o = 0.65$, respectively.

The applications of simulating the permeability tests are listed in Table 6.1. The detailed explanations for each application are discussed in the follow Sections.

6.3 Single-porosity Approach

In this Section, the simulation is carried out by using the single-porosity approach. Both single-phase and two-phase fluid flow cases are considered in the study, in

Table 6.1: Different methods used in the simulation of the permeability test.

Single-porosity approach	Single-phase, horizontal injection Single-phase, vertical injection Two-phase, horizontal injection
Dual-porosity approach	Single-phase, horizontal injection Single-phase, vertical injection Two-phase, horizontal injection, no loading Two-phase, horizontal injection with loading

which the water is injected at one side and withdrawn at other side of the sample for the horizontal injection case, and injected at the top and withdrawn at the bottom of the sample for the vertical injection case.

6.3.1 Single-phase Fluid Flow

For the case of a single-phase fluid in a single-porosity problem, there are two cases to study: horizontal and vertical injections.

Horizontal Injection

In the experiment to test rock sample permeability, single-porosity single-phase fluid flow test is commonly used for its simplicity. The single-phase fluid (water) is injected through one side of the rock sample by controlling the flowrate or fluid pressure, and the pressures or flowrate are also controlled on the other side of the sample. The parameters used in the horizontal injection simulation are shown in Table 6.2.

Figure 6.3 shows the changes in fluid pressures and displacements in the x-direction with time at some points of the rock sample shown in Figure 6.4. The fluid pressures decrease with time. Higher pressure values appear near the injection area and decrease with the positions from injection to withdrawal areas.

Figures 6.5, 6.6, 6.7 and 6.8 demonstrate the contours of the fluid pressures and

Table 6.2: Parameters used in single-phase single-porosity case.

Parameter	Definition	Magnitude	Units
E	modulus of elasticity	3000.0	MN/m^2
ν	Poisson's ratio	0.2	
α_1	Biot coefficient	0.861	
K_f	fluid bulk modulus	3.0E3	MN/m^2
ϕ_1	matrix porosity	0.2	
k_1/μ	matrix mobility	9.87E-6	$m^4/(MN{\cdot}s)$
K_s	solid grain bulk modulus	1.2E4	MN/m^2
Q_w	injection water flow rate	5.0E-7	m^3/s

the displacements at the cross-sections of central vertical plane (y = 0 at Figure 6.4) and central horizontal plane (z = -0.1 m at Figure 6.4) at the beginning of the fluid injection. While the changes of fluid pressures and displacements after 5 timestep are shown in Figures 6.9, 6.10 and 6.11. Comparing with Figure 6.3, Figures 6.5, 6.6, 6.9 and 6.10 also show the changes of fluid pressures with higher values around the injection area and the pressures decreasing with time. The displacements show that the rock volume increases with the larger values near both the injection and the withdrawal areas. It is noted that the sample volume change is due to the pressure increase which results in the pore volume expansion.

Vertical Injection

The fluid is injected through the center of the sample top surface by controlling the flowrate or fluid pressures, and also the fluid pressures or flowrate are controlled at the withdrawn area which is located in the center of the sample bottom. For the vertical injection experiment, the permeability along z-direction of the sample (Figure 6.2) can be obtained. The parameters used in the simulation are similar to the previous case and shown in Table 6.2.

Figure 6.12 demonstrates the changes of fluid pressures and displacements along x-direction with time in some points of the rock sample (Points B, C and D in

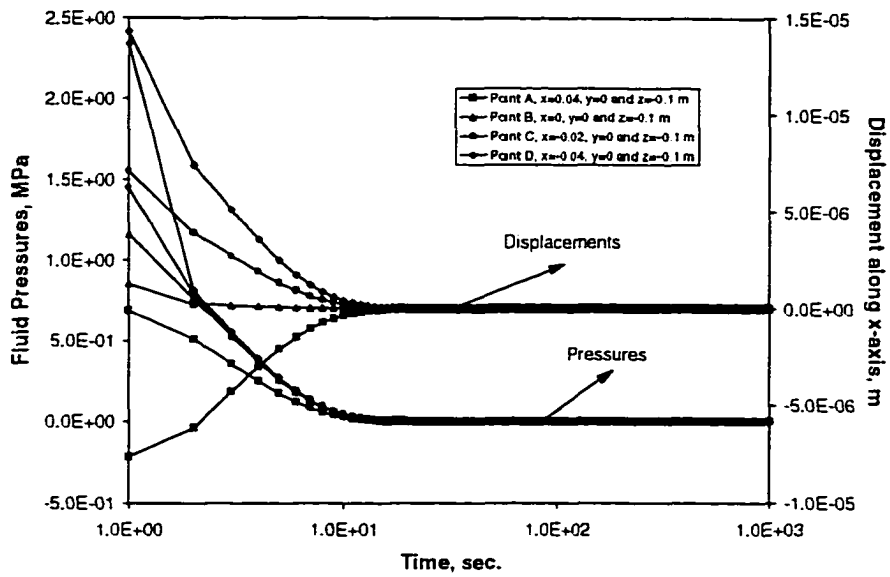

Figure 6.3: Fluid pressures and displacements with time.

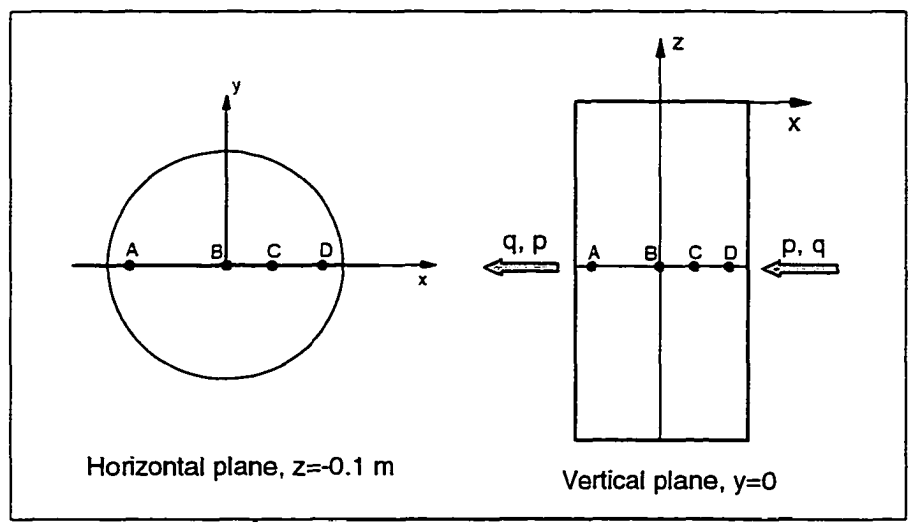

Figure 6.4: Cross-sections and points for the analysis.

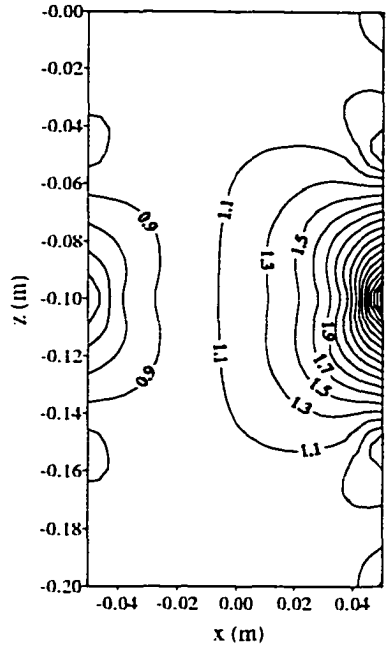

Figure 6.5: Fluid pressure distributions at vertical plane, t = 1 sec.

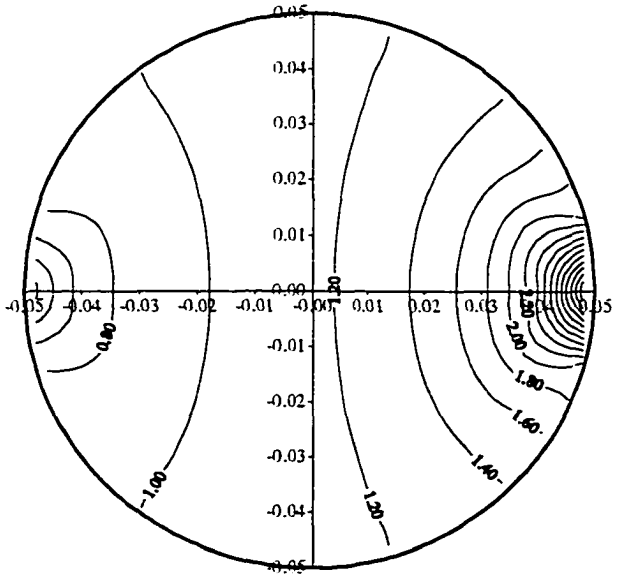

Figure 6.6: Fluid pressure distributions at horizontal plane, z = -0.1 m, t = 1 sec.

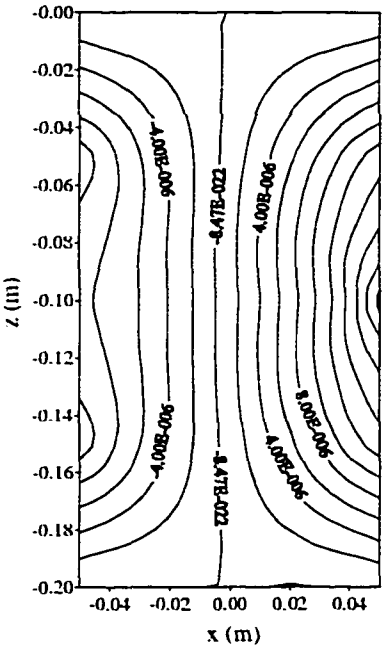

Figure 6.7: Displacements along x-axis at vertical plane, t = 1 sec.

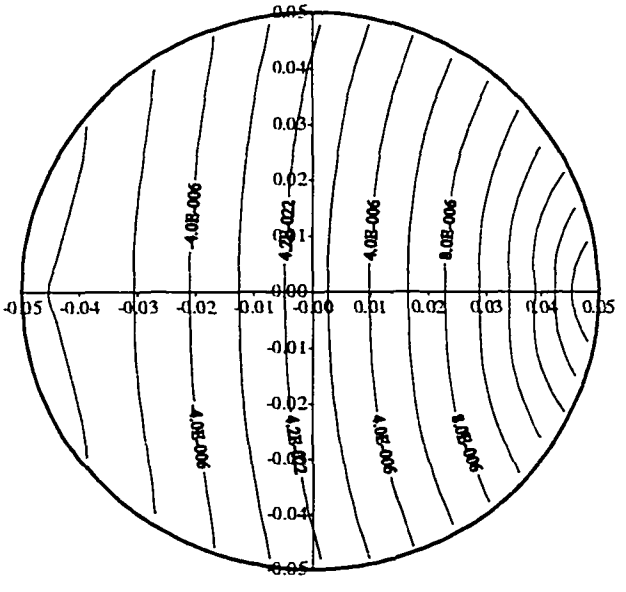

Figure 6.8: Displacements along x-axis at horizontal plane, t = 1 sec.

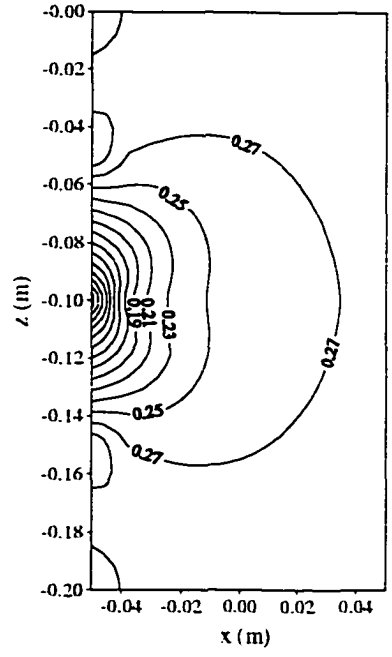

Figure 6.9: Fluid pressure contours at vertical plane, t = 5 sec.

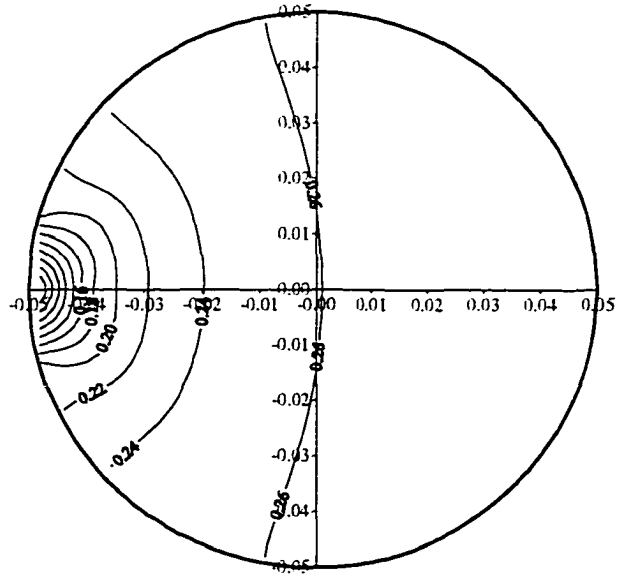

Figure 6.10: Fluid pressure contours at horizontal plane, t = 5 sec.

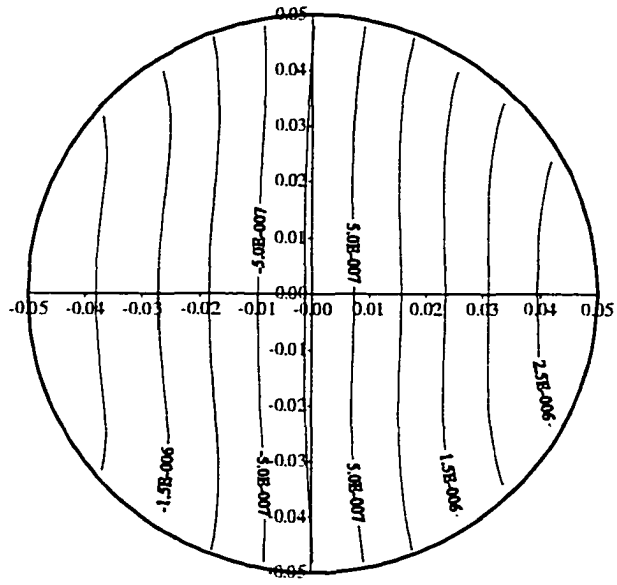

Figure 6.11: Displacements along x-axis at horizontal plane. t = 5 sec.

Figure 6.4), respectively. Together with Figures 6.13, 6.14, 6.15 and 6.16, which show the fluid pressure distributions around both the sample central vertical plane and central horizontal plane at two different timesteps; it can be seen that the fluid pressures decrease as time elapses.

The changes of displacements along the x-axis across the vertical planes are shown in Figures 6.17 and 6.19 for two different timesteps. Figures 6.18 and 6.20 represent the displacements along radial direction at the horizontal plane. The displacements decrease with time and show that the rock sample volume increases with fluid injected from the top.

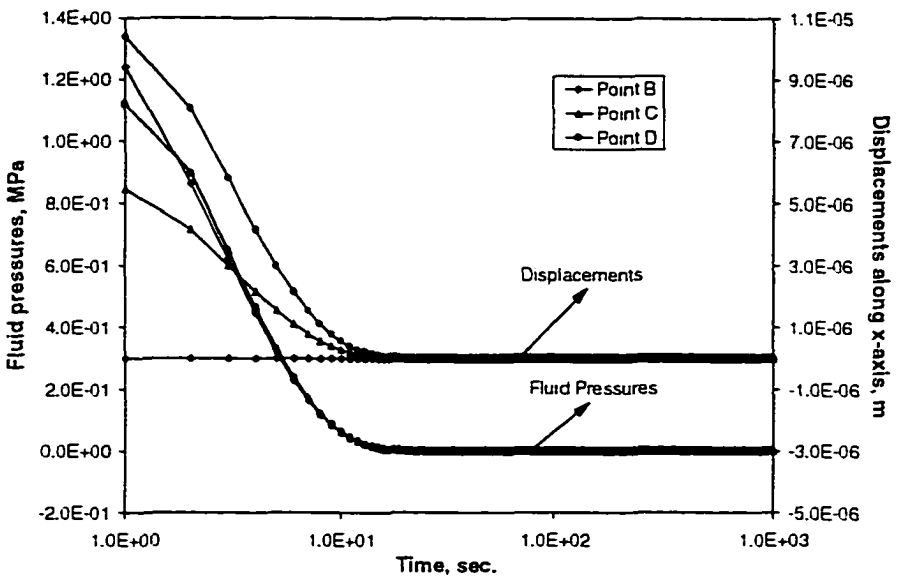

Figure 6.12: Fluid pressures and displacements along x-axis with time.

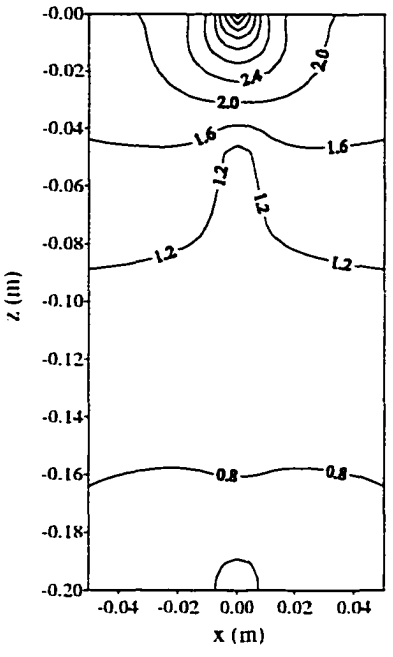

Figure 6.13: Fluid pressures at vertical plane, t = 1 sec.

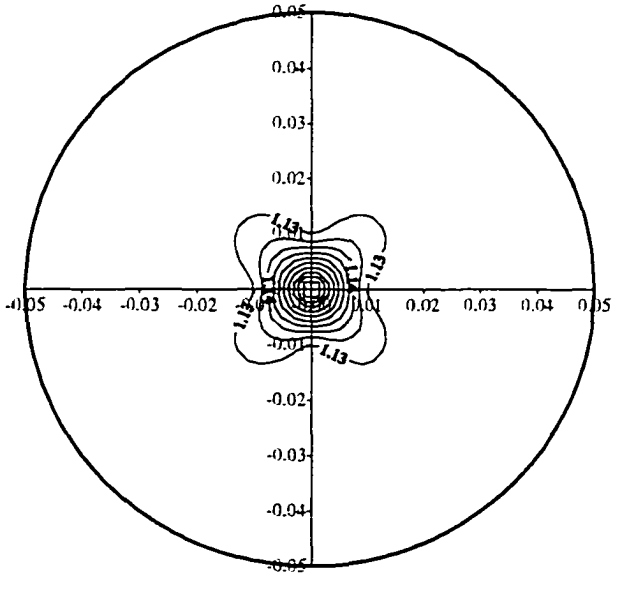

Figure 6.14: Fluid pressures at horizontal plane, t = 1 sec.

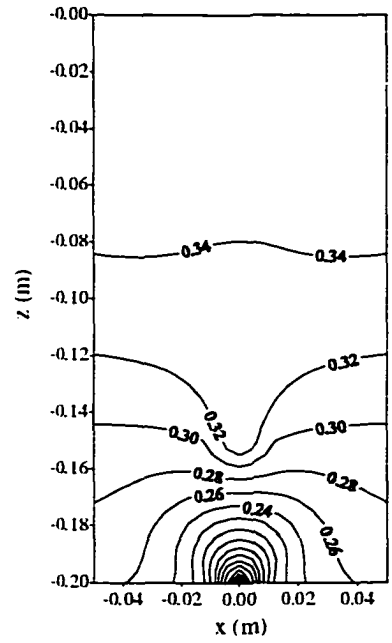

Figure 6.15: Fluid pressures at vertical plane. t = 5 sec.

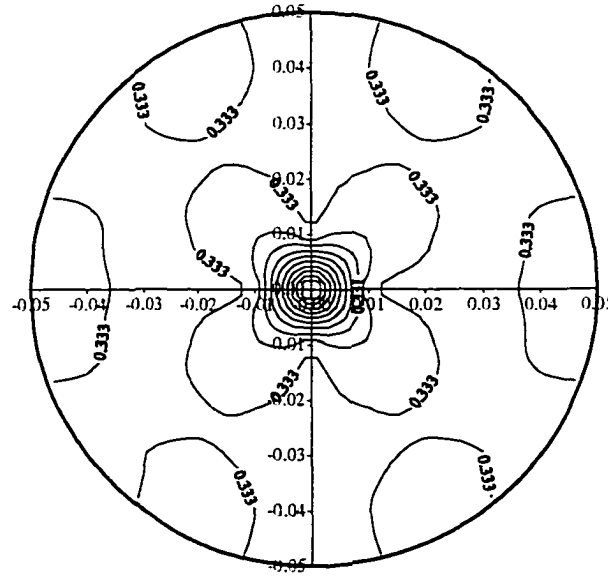

Figure 6.16: Fluid pressures at horizontal plane, t = 5 sec.

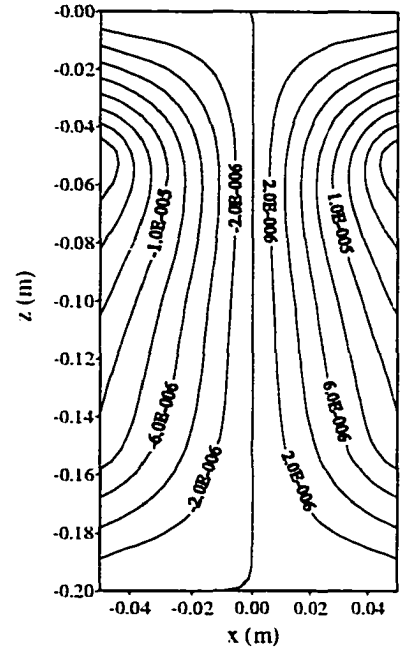

Figure 6.17: Displacements along x-axis at vertical plane, t = 1 sec.

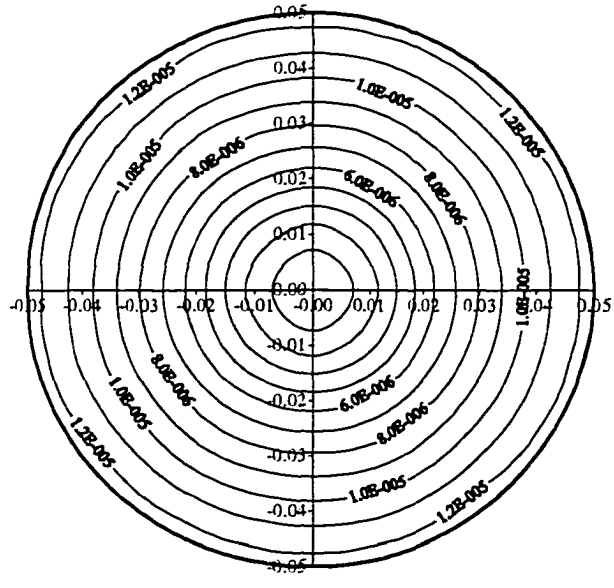

Figure 6.18: Displacements in radial direction at horizontal plane, t = 1 sec.

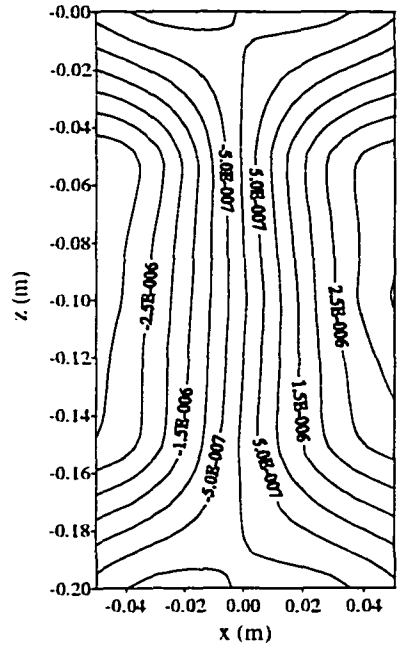

Figure 6.19: Displacements along x-axis at vertical plane. t = 5 sec.

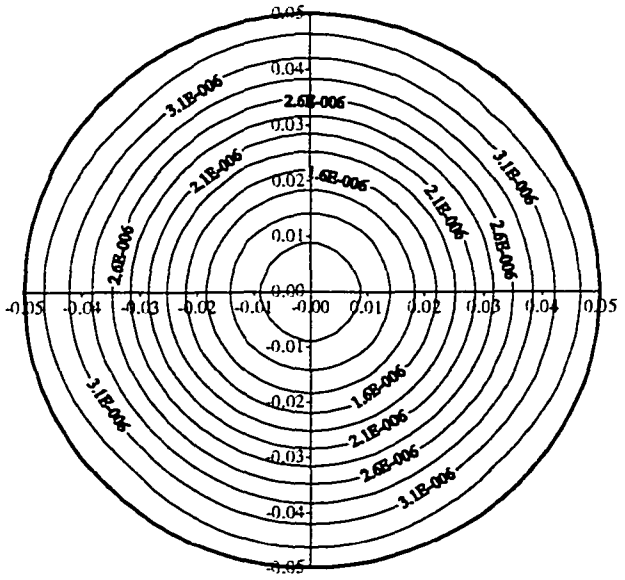

Figure 6.20: Displacements in radial direction at horizontal plane, t = 5 sec.

6.3.2 Two-phase Fluid Flow

For the two-phase fluid flow simulation, the relationships between the relative permeability and the water saturation remain the same as predicted by Equation (4.11). Also the relationship based on the same expression as Equation (4.12) and Figure 4.5 is used for the capillary pressure and water saturation curves. The parameters used in the two-phase simulation are listed in Table 6.3.

Table 6.3: Parameters used in two-phase single-porosity case.

Parameter	Definition	Magnitude	Units
E	modulus of elasticity	3000.0	MN/m^2
ν	Poisson's ratio	0.2	
α_1	Biot coefficient	0.861	
K_f	fluid bulk modulus	3.0E3	MN/m^2
ϕ_1	matrix porosity	0.2	
k_1/μ	matrix mobility	9.87E-6	$m^4/(MN \cdot s)$
K_s	solid grain bulk modulus	1.2E4	MN/m^2
Q_w	injection water flow rate	5.0E-8	m^3/s

Figures 6.21 and 6.22 illustrate the changes of water pressures and displacements along the x-direction, and water saturations as a function of time for points A, B, C and D of the rock sample (Figure 6.4), respectively. The water pressures decrease with time when the locations are close to the injection area and when the analyzed points are near withdrawal area the water pressures increase a little at the beginning then decrease. In this case study, the fluid (water) is instantaneously injected into the rock sample. In such case, the changes of the fluid pressures will reach the highest values immediately after the injection, then decrease to the initial fluid pressure values at the locations close to injection area. While at the points near the withdrawal area, the fluid pressures will increase at the beginning time, and then decrease. This is due to the fact that the fluid pressures will achieve the highest

values after a period of time of injection.

The water saturations show a faster increase when close to the injection area. The displacements indicate that the rock sample volume increases around the injection area because the water fills the pore volume, while at the withdrawal area the sample volume shrinks at the very early time, then expands due to the fact that fluid start to fill the pore space.

Figures 6.23, 6.24, 6.25 and 6.26 show the water pressure distributions around the sample central vertical plane ($y = 0$ at Figure 6.4) and central horizontal plane (z = -0.1 m at Figure 6.4) at two timesteps. It also can be seen that the water pressures are higher at the beginning than at later times, and higher at the injection than withdrawal areas.

The changes of water saturation across the vertical and horizontal planes are shown in Figures 6.27, 6.28, 6.29 and 6.30. The displacing process (e.g., water displacing oil) can be clearly seen along the moving front of the injected water.

The displacements depicted in Figures 6.31, 6.32, 6.33 and 6.34 demonstrate that the rock sample volume increases due to the fluid filling the pore volume of the sample.

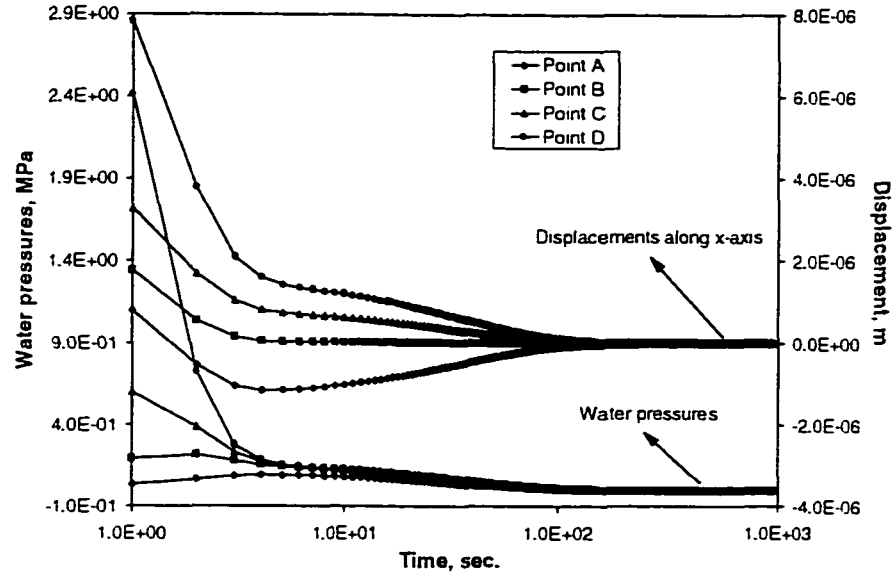

Figure 6.21: Water pressures and displacements with time.

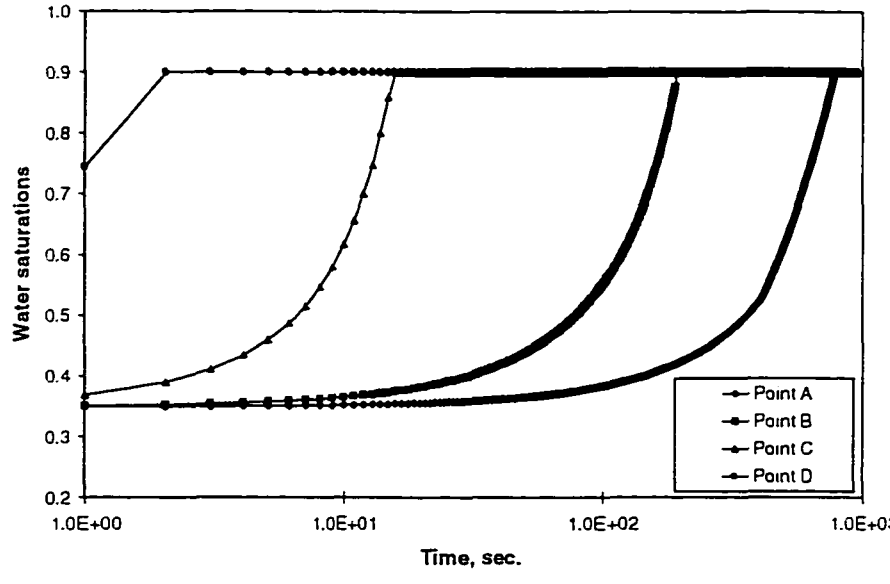

Figure 6.22: Water saturations with time at different points.

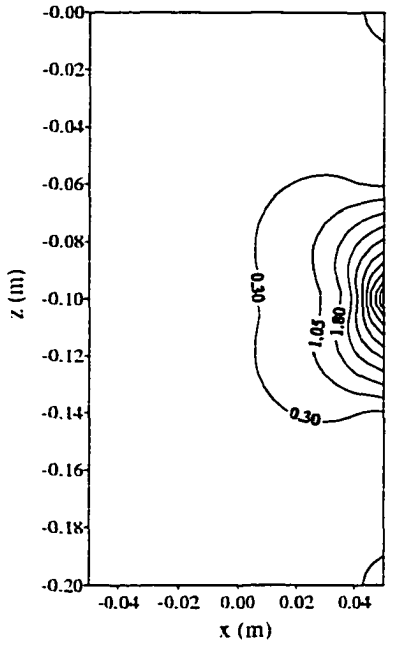

Figure 6.23: Water pressures at central vertical plane, t = 1 sec.

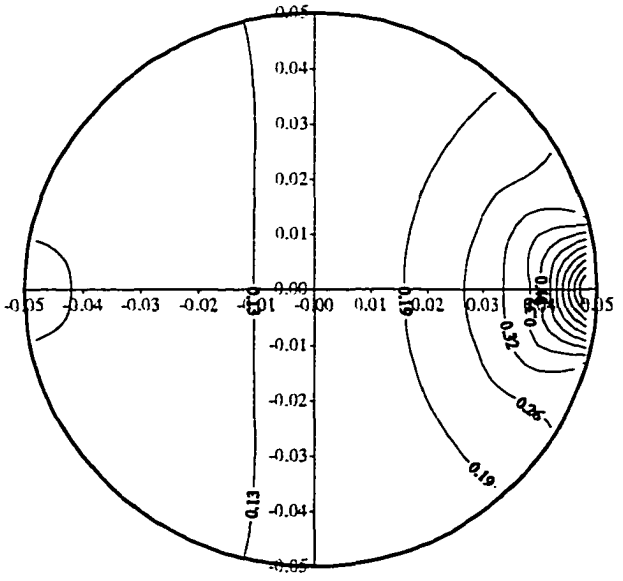

Figure 6.24: Water pressures at central horizontal plane, t = 1 sec.

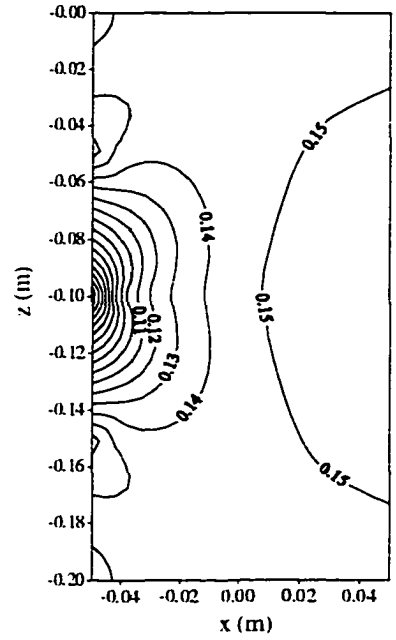

Figure 6.25: Water pressures at central vertical plane, t = 5 sec.

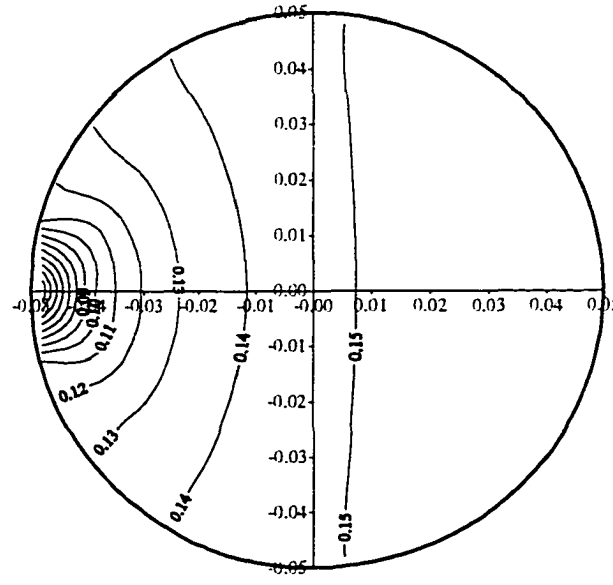

Figure 6.26: Water pressures at central horizontal plane, t = 5 sec.

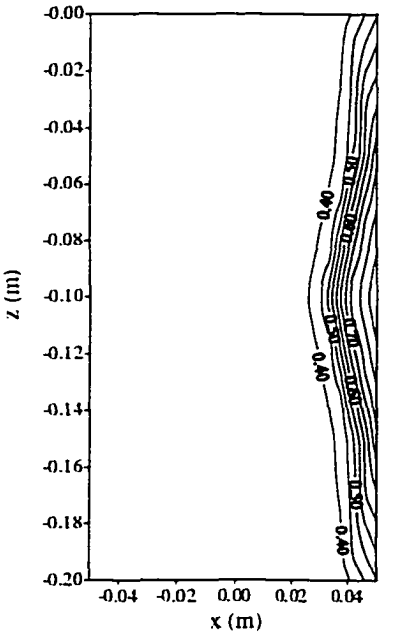

Figure 6.27: Water saturations at central vertical plane. t = 1 sec.

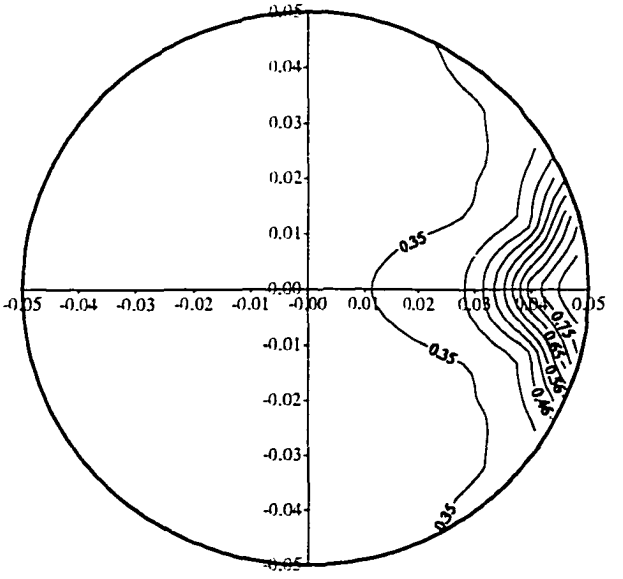

Figure 6.28: Water saturations at central horizontal plane. t = 1 sec.

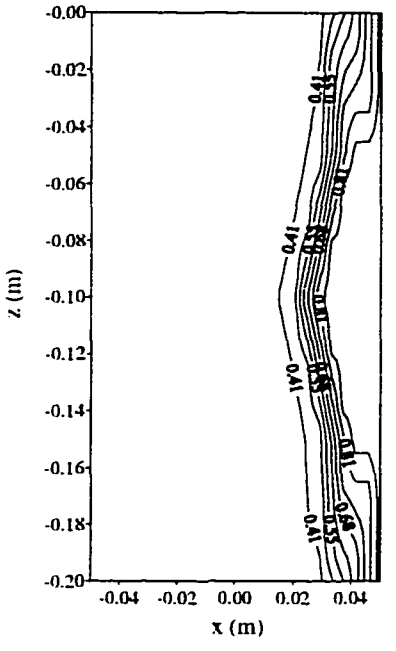

Figure 6.29: Water saturations at central vertical plane. t = 5 sec.

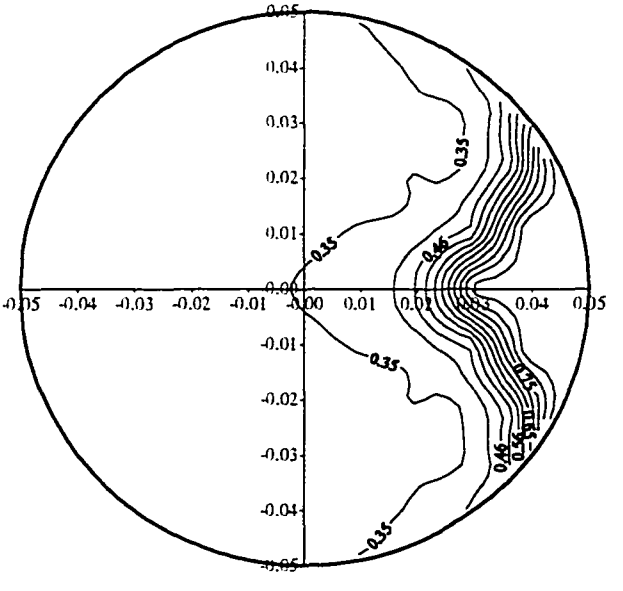

Figure 6.30: Water saturations at central horizontal plane. t = 5 sec.

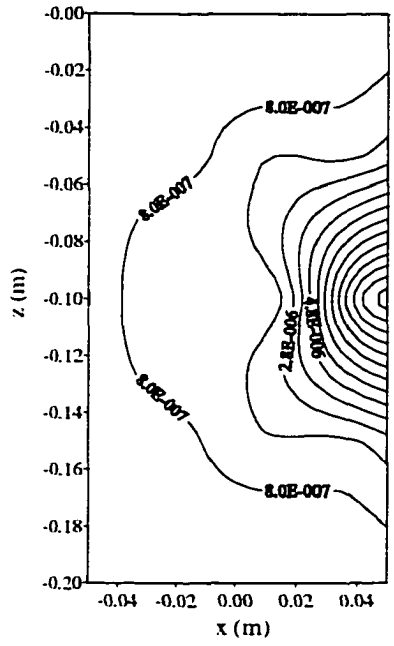

Figure 6.31: Displacements along x-axis at vertical plane. t = 1 sec.

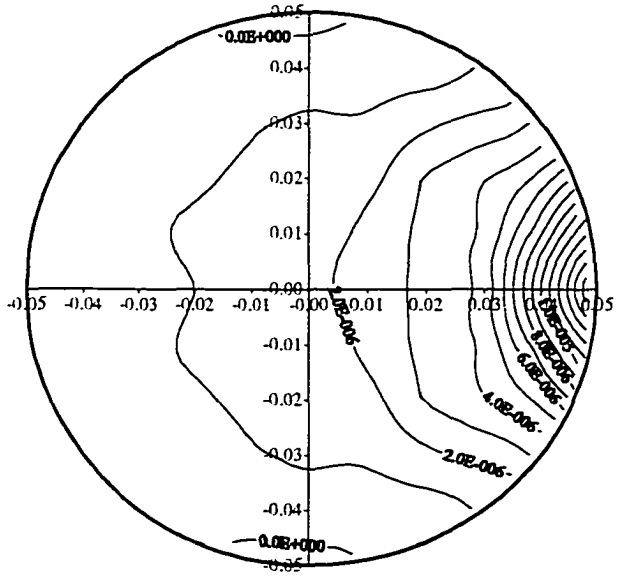

Figure 6.32: Displacements at central horizontal plane along x-axis, t = 1 sec.

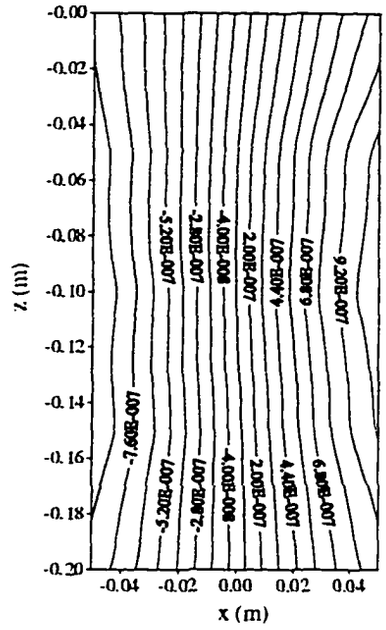

Figure 6.33: Displacements along x-axis at horizontal plane. t = 5 sec.

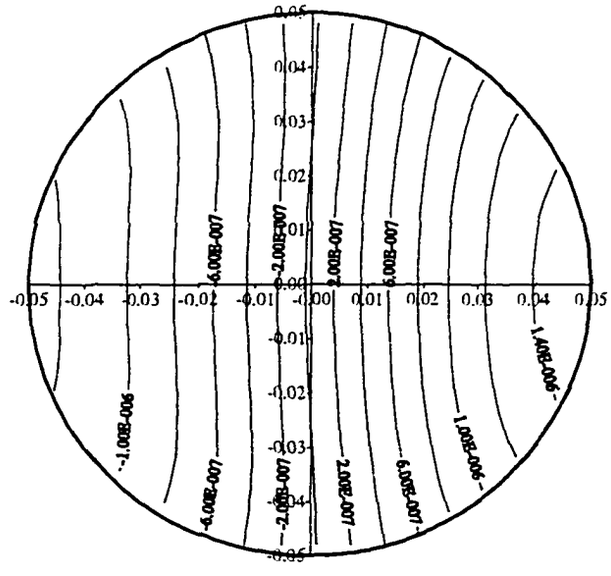

Figure 6.34: Displacements at central horizontal plane along x-axis, t = 5 sec.

6.4 Dual-porosity Approach

For the fractured rock sample, the more reasonable method for the simulation is to use the dual-porosity approach. Single-phase and two-phase fluid flow cases are involved in the examples. Also for the two-phase horizontal injection case, both considering the external loading and without external loading cases are compared. For the no external loading case (only fluid injection), the fixed boundaries on the top and bottom of the specimen are designed. And for the loading case (external loading and fluid injection), the uniaxial load is imposed on the top of the sample, which allows the compression of the sample in the vertical direction.

6.4.1 Single-phase Fluid Flow

This case is studied using the dual-porosity approach in which horizontal and vertical injections are considered. The parameters in the simulation are listed in Table 6.4.

It should be noted that in general, α_1 and α_2, in Table 6.4, are not equal to each other (Bai *et al.*, 1993). Based on an experimental study, *Walsh* (1981) suggested that α_2 varies between 0.5 and 1.0. In that work it was determined that $\alpha_2 = 0.9$ for joints with polished surfaces and $\alpha_2 = 0.56$ for a joint made from a tension fracture. However, for this particular simulation, it is assumed that these two parameters were equal.

Horizontal Injection

Figure 6.35 demonstrates the changes of water pressures in both the rock matrix and the fracture with time at some points of the rock sample (Figure 6.4), respectively. Both pressures in the rock matrix and the fractures decrease with time. At the early time, the pressures in the fractures are higher than the pressures in the rock matrix. While at positions not close to the injection area, it can be seen that the water pressures are higher in the rock matrix than in the fractures.

Table 6.4: Parameters used in single-phase dual-porosity case.

Parameter	Definition	Magnitude	Units
E	modulus of elasticity	3000.0	MN/m^2
ν	Poisson's ratio	0.2	
α_1, α_2	Biot coefficient	0.861	
K_n	normal fracture stiffness	1.2E5	$MN/m^2/m$
K_f	fluid bulk modulus	3.0E3	MN/m^2
ϕ_1	matrix porosity	0.2	
ϕ_2	fracture porosity	0.05	
k_1/μ	matrix mobility	9.87E-8	$m^4/(MN{\cdot}s)$
k_2/μ	fracture mobility	9.87E-6	$m^4/(MN{\cdot}s)$
s	fracture spacing	1.0E-2	m
K_s	solid grain bulk modulus	1.2E4	MN/m^2
Q_w	injection water flow rate	5.0E-7	m^3/s

The changes of the displacements along the x-direction in Figure 6.36 indicate that the rock sample volume increases around the injection area because the water fills the pore volume, and the expansion of the volume decreases with time. While at the withdrawal area the volume also expands, but with a small value compared with the volume change in injection area. This is the fact that higher fluid pressures exist in the injection area than in the withdrawal area.

Water saturations show more faster increase when the locations are close to injection area. This is because the injected water moves from the injection area to the withdrawal area. Gradually the injected water fills the whole sample.

Figures 6.37, 6.38, 6.39 and 6.40 show the water pressure distributions around the sample central vertical plane and central horizontal plane at two timesteps. It can be seen that the water pressures are higher at the beginning than the later time, and also higher at the injection area than withdrawal area.

The displacements depicted in Figures 6.41, 6.42, 6.43 and 6.44 also show the increase of the changes of the sample volume.

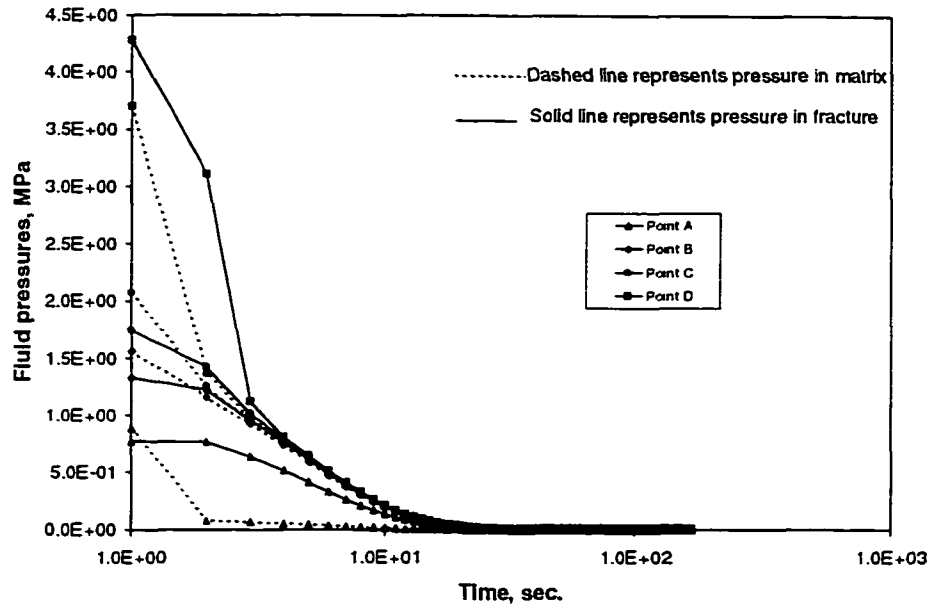

Figure 6.35: Fluid pressures with time at different points.

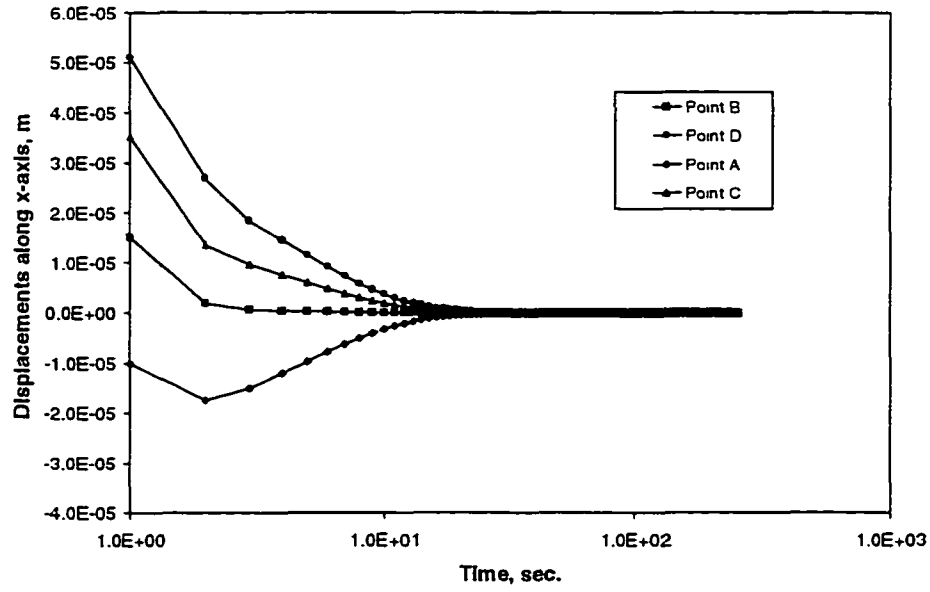

Figure 6.36: Displacements along x-axis with time at different points.

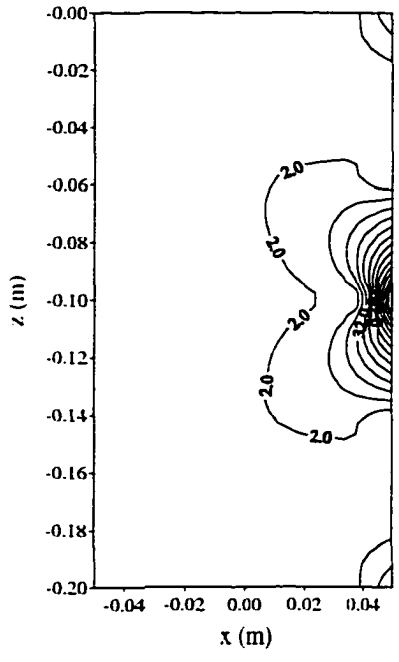

Figure 6.37: Fluid pressure at vertical plane, t = 1 sec.

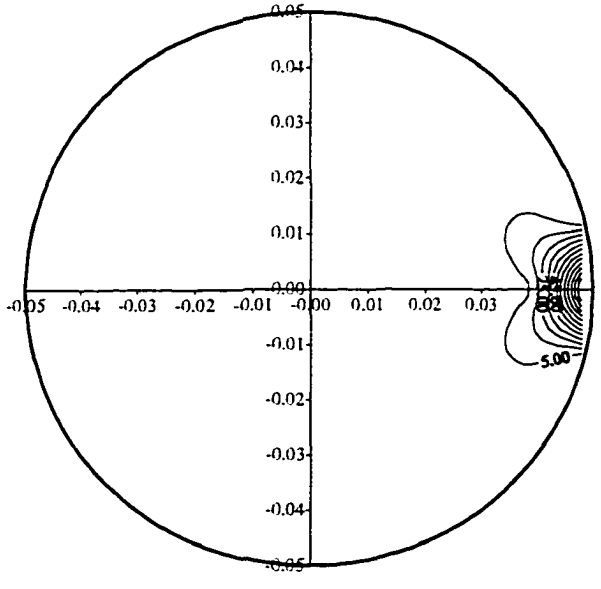

Figure 6.38: Fluid pressures at horizontal plane, t = 1 sec.

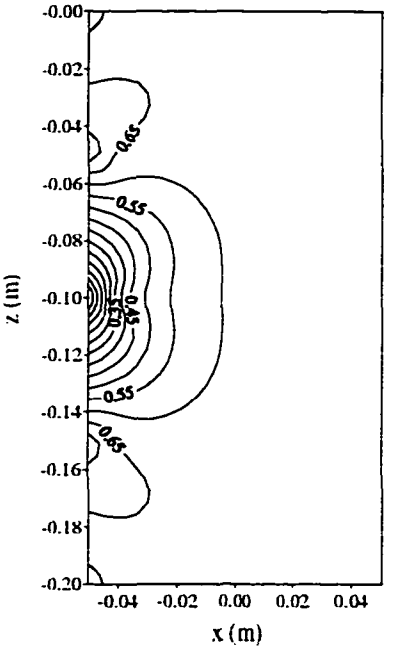

Figure 6.39: Fluid pressures at vertical plane, t = 5 sec.

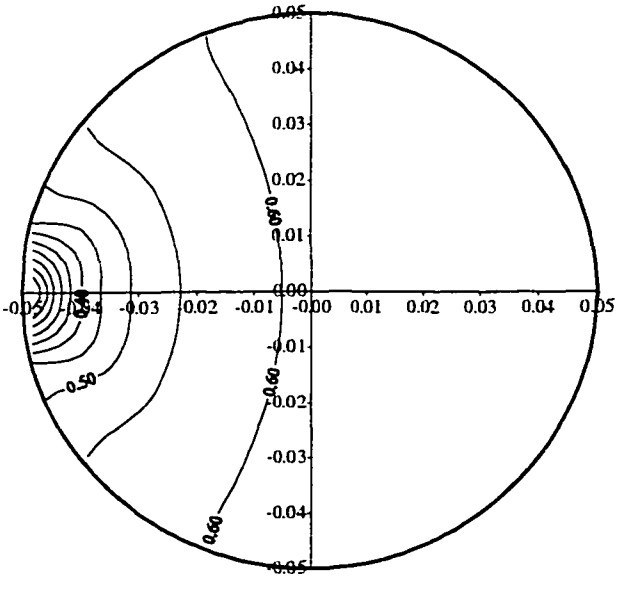

Figure 6.40: Fluid pressures at horizontal plane, t = 5 sec.

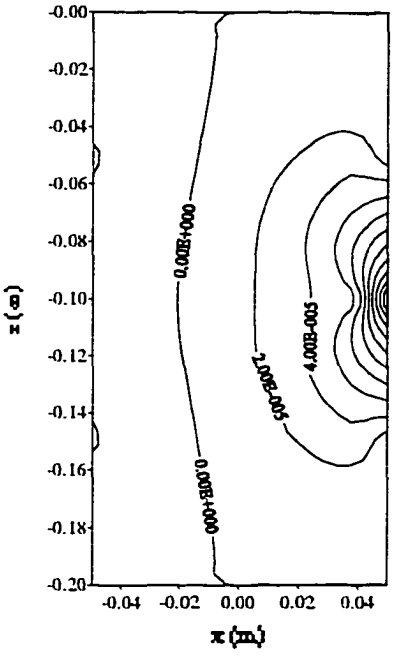

Figure 6.41: Displacements along x-axis at vertical plane, t = 1 sec.

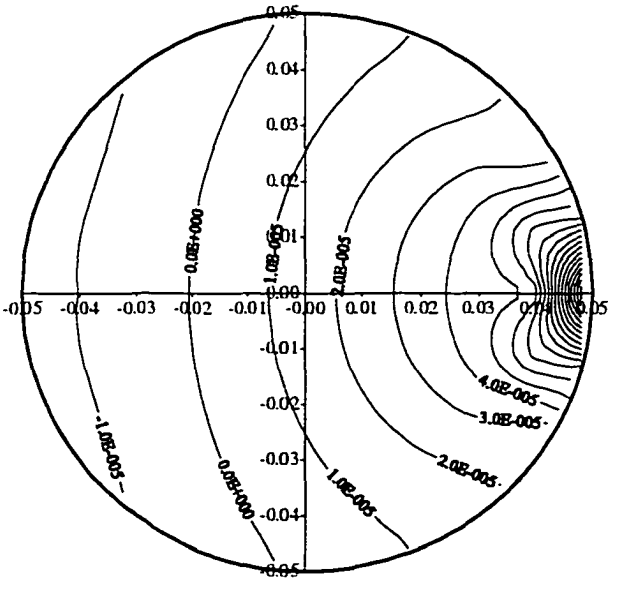

Figure 6.42: Displacements along x-axis at horizontal plane, t =1 sec.

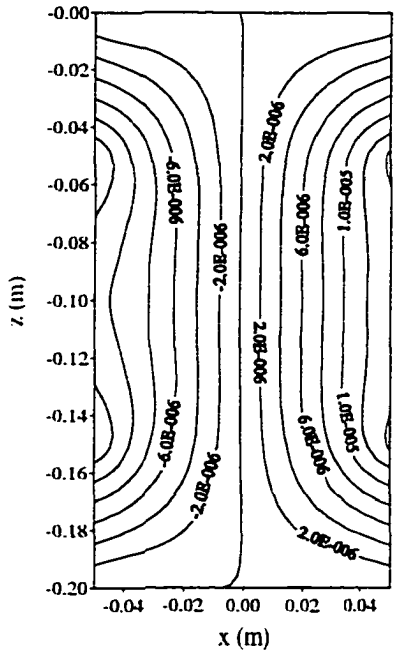

Figure 6.43: Displacements along x-axis at vertical plane. t = 5 sec.

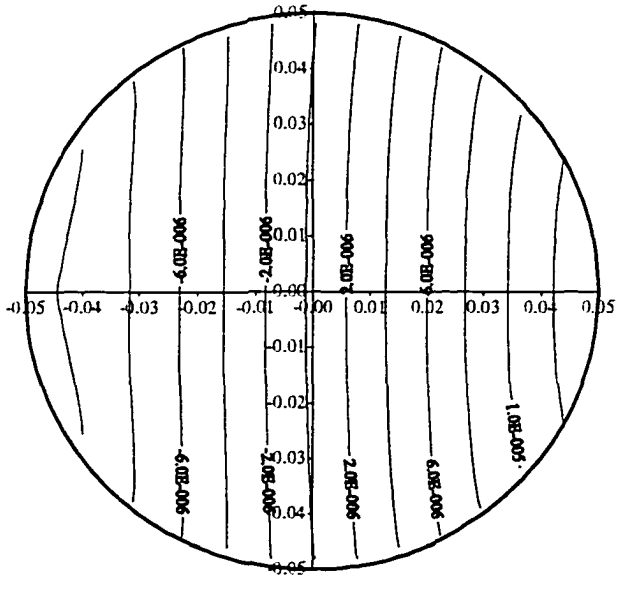

Figure 6.44: Displacements along x-axis at horizontal plane, t = 5 sec.

Vertical Injection

In this case, the fluid is injected through the center of the sample top surface and withdrawn from the area which is located in the center of the sample bottom. The parameters used in the simulation are shown in Table 6.4.

Figure 6.45 demonstrates the changes of fluid pressures and displacements along the x-direction as a function of time at some points of the rock sample (Points B, C and D in Figure 6.4), respectively. The fluid pressures in both the rock matrix and the fracture decrease with time except in locations far from the center, like point D, where the pressures in the matrix increase at the very early time. The pressures are higher when the analyzed points are close to the center of the sample than those located far from the center. When comparing the displacements along the x-direction in points B, C and D, it can be seen that the largest value appears in point D, and the smallest value in point B. This indicates that the largest changes of the displacements along the x-direction which represent the rock sample expansion will appear at the boundary of the sample.

Figures 6.46, 6.47, 6.48 and 6.49 show the matrix fluid pressure distributions around both the sample central vertical plane and central horizontal plane at two different timesteps.

The changes of displacements along x-axis across the vertical planes are shown in Figures 6.50 and 6.51 for two different timesteps. Figures 6.52 and 6.53 represent the displacements along the radial direction in a horizontal plane. The displacements decrease with time and show the rock sample volume increases with fluid injected from the top.

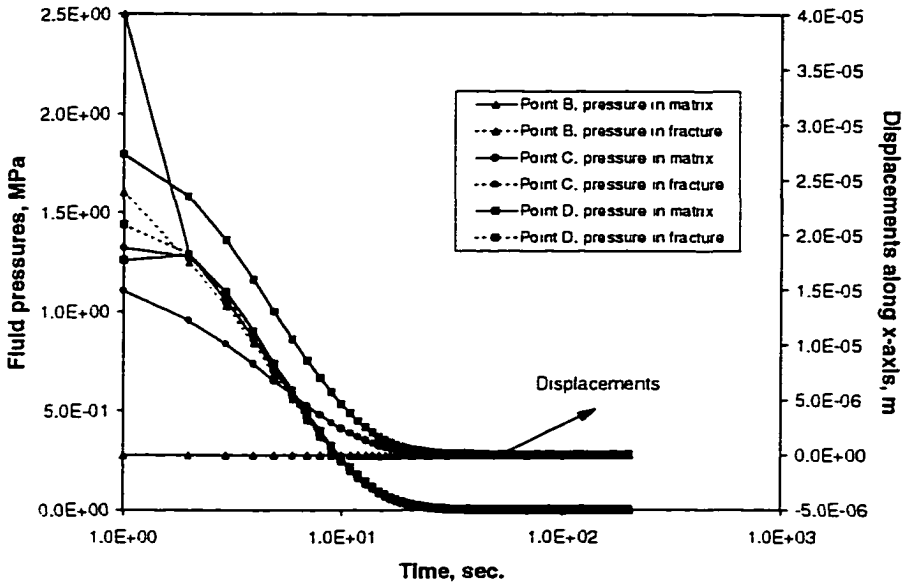

Figure 6.45: Fluid pressures and displacements along x-axis with time.

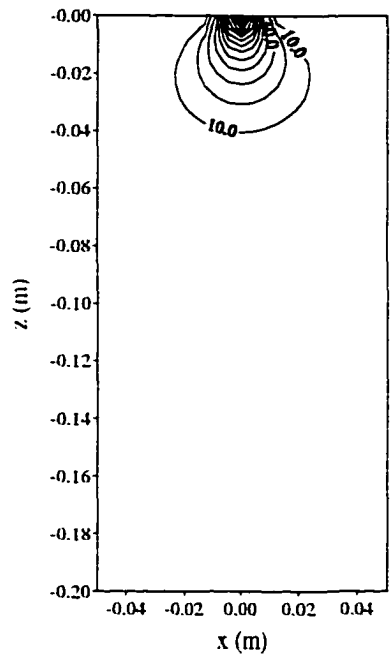

Figure 6.46: Fluid pressures in the matrix at vertical plane, t = 1 sec.

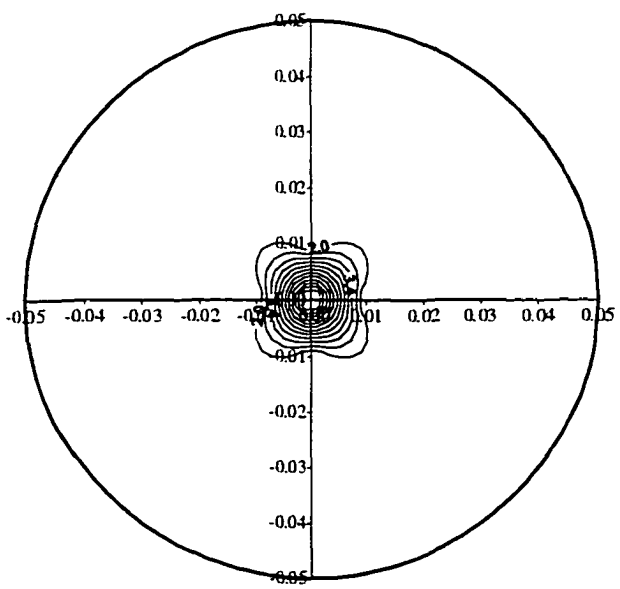

Figure 6.47: Fluid pressures in the matrix at horizontal plane, t =1 sec.

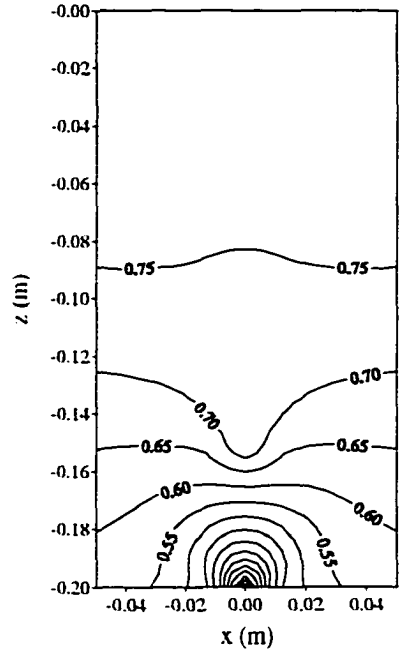

Figure 6.48: Fluid pressures in the matrix at vertical plane. t = 5 sec.

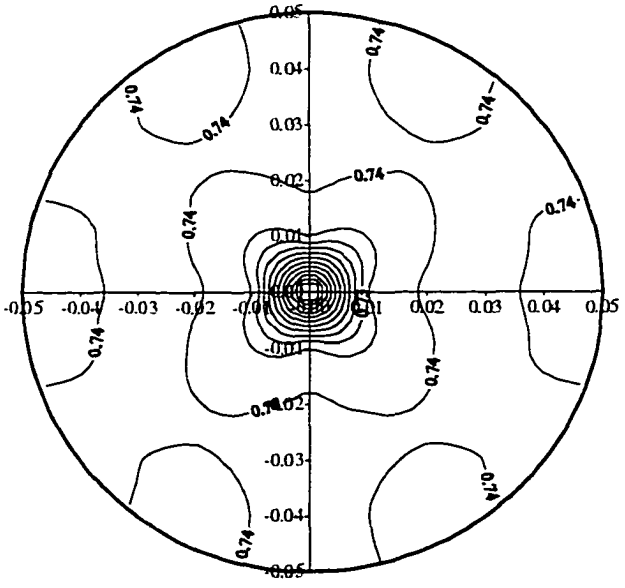

Figure 6.49: Fluid pressures in the matrix at horizontal plane, t = 5 sec.

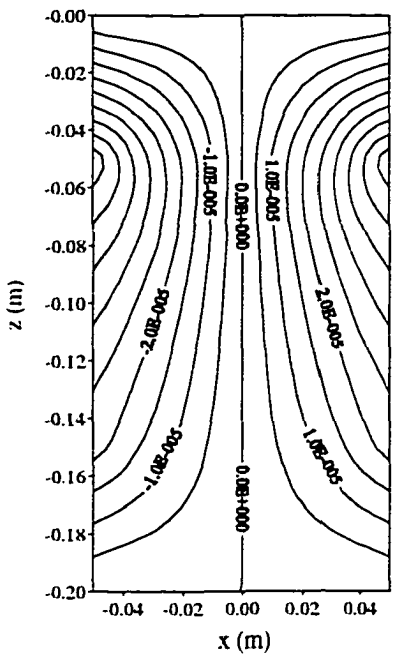

Figure 6.50: Displacements along x-axis at vertical plane, t = 1 sec.

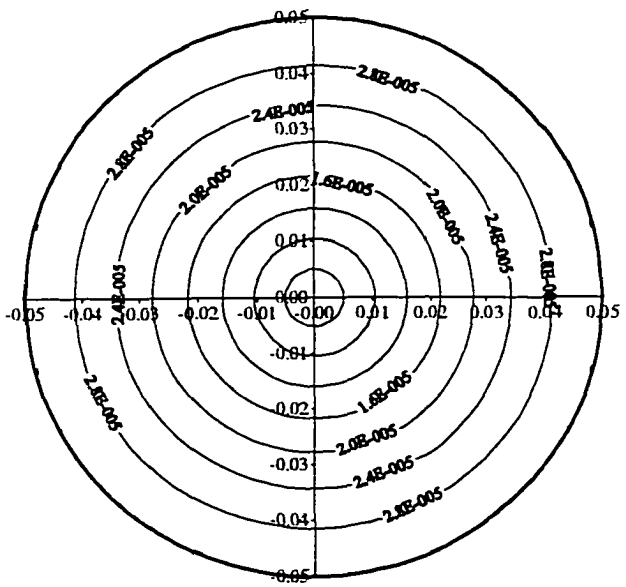

Figure 6.51: Displacements along radial direction at horizontal plane, t =1 sec.

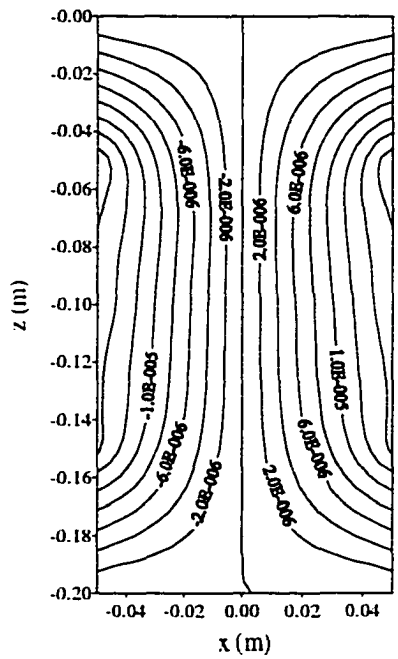

Figure 6.52: Displacements along x-axis at vertical plane. t = 5 sec.

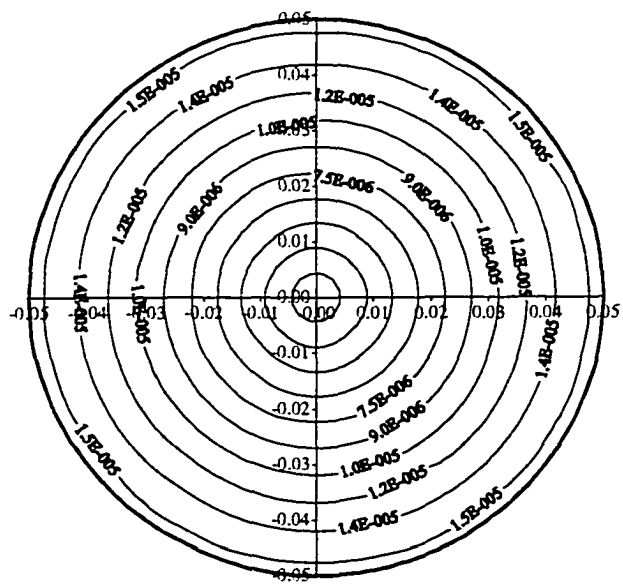

Figure 6.53: Displacements along the radial direction at horizontal plane, t = 5 sec.

6.4.2 Two-phase Fluid Flow

In order to simulate two-phase fluid flow in fractured rock samples, the relationships between the relative permeability and the water saturation are assumed to remain the same as expressed by Equation (4.11); and Equation (4.12) and Figure 4.5 are used. The parameters used in the two-phase simulation are listed in Table 6.5.

Table 6.5: Parameters used in two-phase dual-porosity case.

Parameter	Definition	Magnitude	Units
E	modulus of elasticity	3000.0	MN/m^2
ν	Poisson's ratio	0.2	
α_1, α_2	Biot coefficient	0.861	
K_n	normal fracture stiffness	1.2E6	$MN/m^2/m$
K_f	fluid bulk modulus	3.0E3	MN/m^2
ϕ_1	matrix porosity	0.2	
ϕ_2	fracture porosity	0.05	
k_1/μ	matrix mobility	9.87E-8	$m^4/(MN{\cdot}s)$
k_2/μ	fracture mobility	9.87E-6	$m^4/(MN{\cdot}s)$
s	fracture spacing	1.0E-2	m
K_s	solid grain bulk modulus	1.2E4	MN/m^2
Q_w	injection water flow rate	5.0E-8	m^3/s
σ_z	uniaxial loading stress	10.0	MN/m^2

Figure 6.54 demonstrates the water pressure changes in the rock matrix for points A, B, C and D shown in Figure 6.4. At the very early time, the pressures increase with the water injected into the sample; then the pressures decrease with time. The water pressures in the fractures, compared with the water pressures in the rock matrix, show an overall decreasing trend as time elapses (Figure 6.55). The oil pressures in the rock matrix and the fracture systems are very close to the water pressures in each system.

The water saturation changes in the rock matrix and the fracture systems are depicted in Figures 6.56 and 6.57, respectively. Both systems show the water saturation changes faster at points close to the water injection area. In addition, the

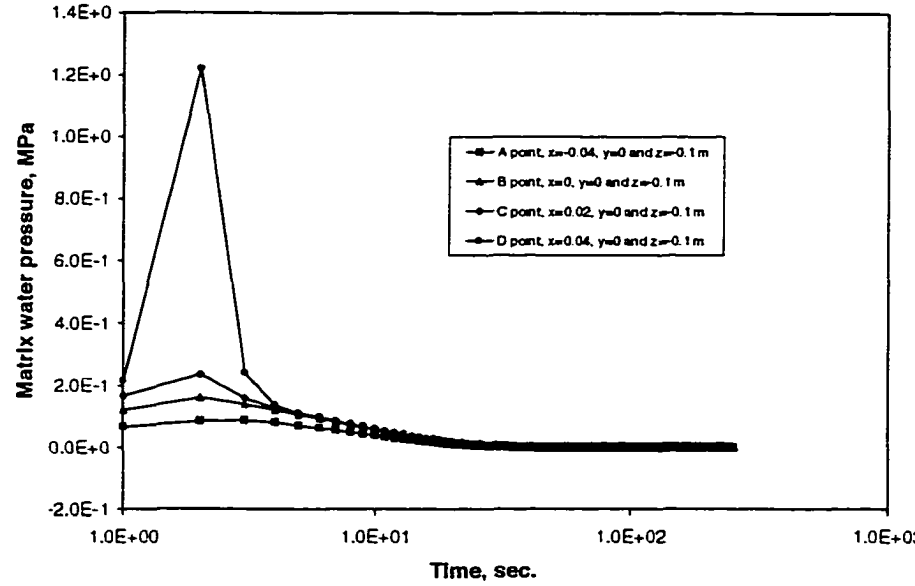

Figure 6.54: Matrix water pressure changes with time at different locations.

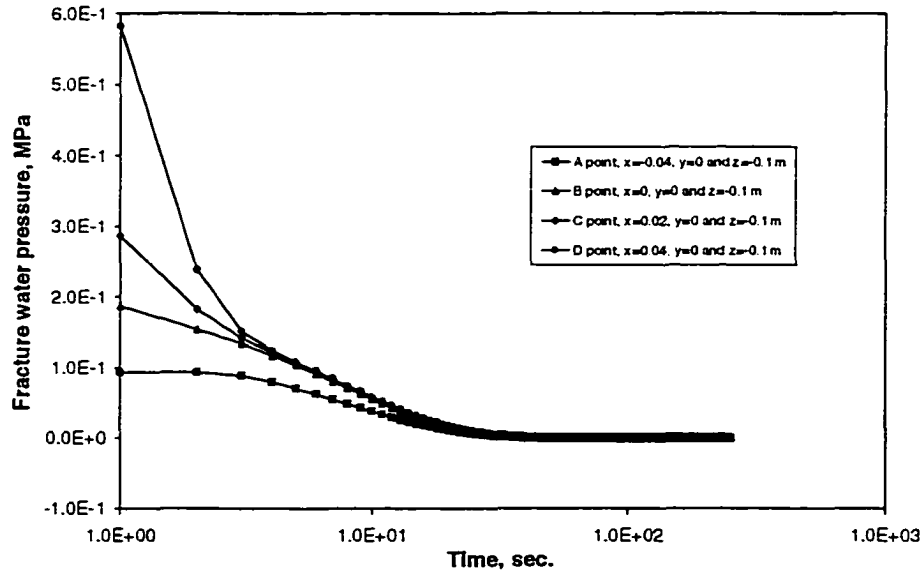

Figure 6.55: Fracture water pressure changes with time at different locations.

water saturations in the fracture system increase faster than the same positions in the rock matrix system due to the higher mobility characteristics of the fracture system.

The displacements along the x-axis for those four points (A. B. C and D in Figure 6.4) are illustrated in Figure 6.58. Water is injected into the rock sample which causes the sample volume to expand. Again, the largest expansion takes place in the beginning close to the water injection area, then the sample volume shrinks with time due to the pore pressure decreasing. While in the withdrawal area, the sample volume will expand at early times until it reaches a maximum before shrinking with time.

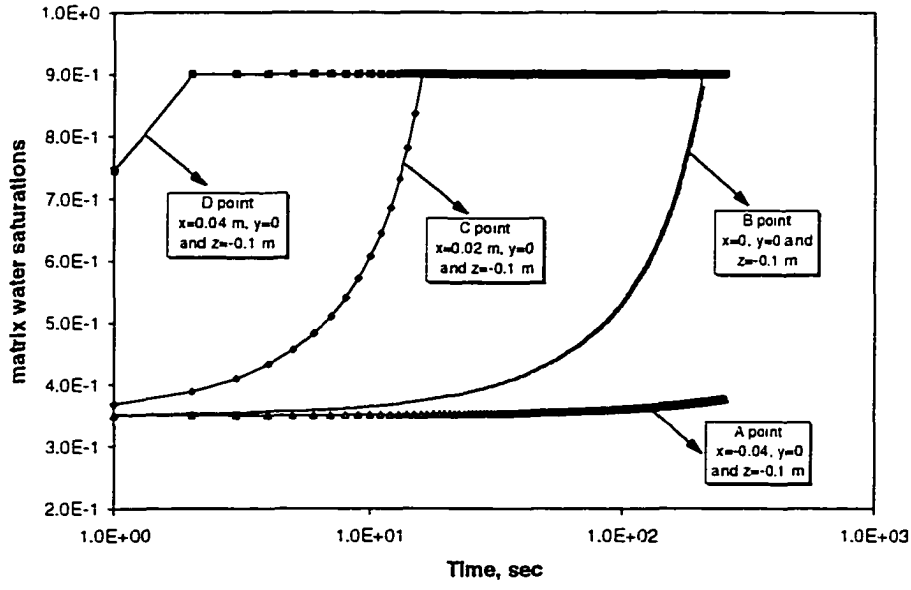

Figure 6.56: Matrix water saturation changes with time at different locations.

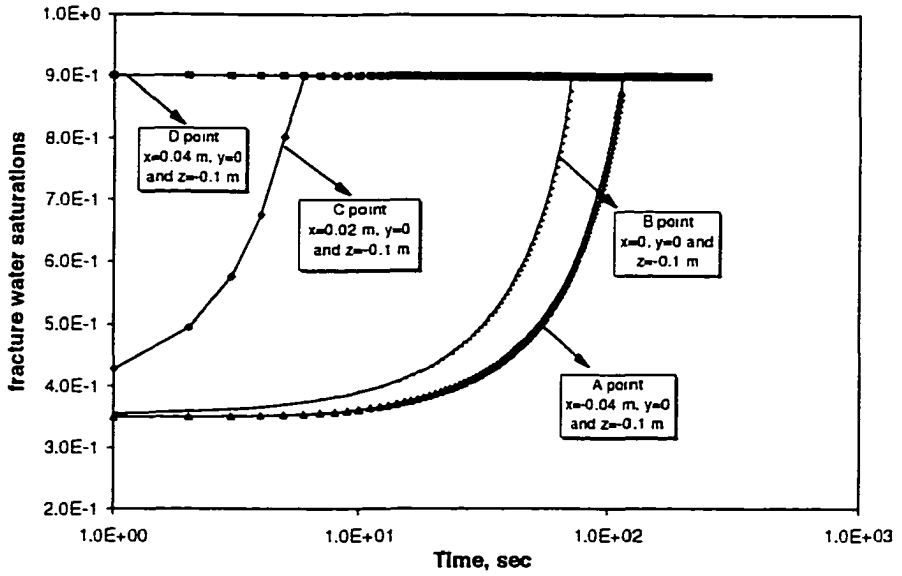

Figure 6.57: Fracture water saturation changes with time at different locations.

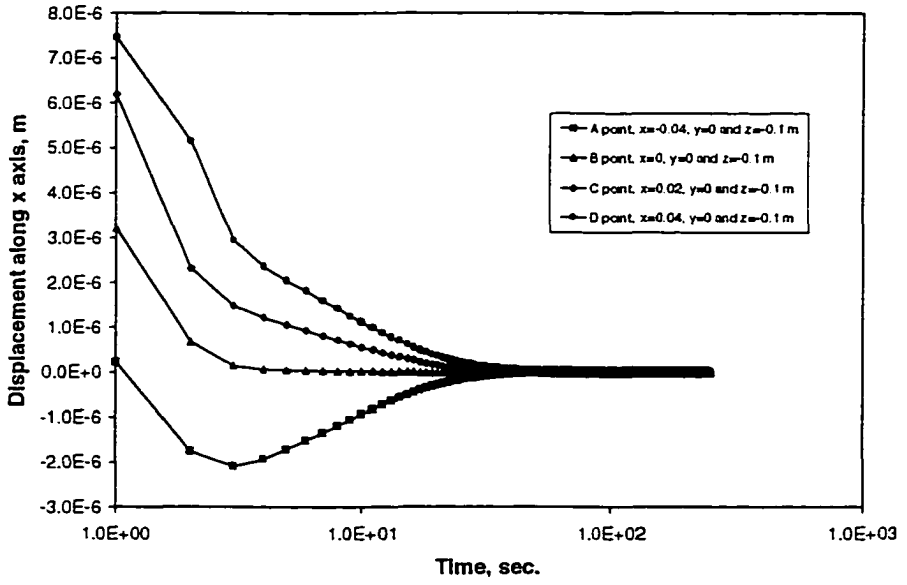

Figure 6.58: Displacement changes with time along x-axis at different locations.

The rock matrix water pressure distributions in the central vertical plane (y = 0, Figure 6.2) and horizontal plane (z = −0.1 m, Figure 6.2) are shown in Figures 6.59, 6.60, 6.61 and 6.62 at two different timesteps. Figures 6.63, 6.64, 6.65 and 6.66 show the fracture water pressure distributions in both the central vertical and horizontal planes.

The water saturation distributions in the rock matrix in both the central vertical and horizontal planes at two different timesteps are depicted in Figures 6.67, 6.68, 6.69 and 6.70, respectively. The figures show that the water saturations increase with time in both cross-sections. The water saturation moving from the right side of the figures (water injection areas) to the left side of the figures is clearly demonstrated in those figures. Figures 6.71, 6.72, 6.73 and 6.74 show the fracture water saturation distributions in both vertical and horizontal planes. The water saturation changes in the fracture system not only demonstrate the values increasing with time, but also show a larger value than the water saturation changes in the rock matrix at the same point and at the same time. This is again because the injection water moves faster in fracture system which has a higher mobility than the rock matrix system.

The displacements along the x-axis are shown in Figures 6.75, 6.76, 6.77 and 6.78, respectively. The values in the figures represent the sample volume expansion after the water injection. The largest expansion values occur at the injection points. And the changes of sample expansion decrease with time. Figures 6.79 and 6.80 show the displacements along y-axis in central horizontal plane for two timesteps. At the beginning, the largest displacements appear near the injection point. Then as time elapses, the largest values move up to the top and bottom sides of the horizontal plane.

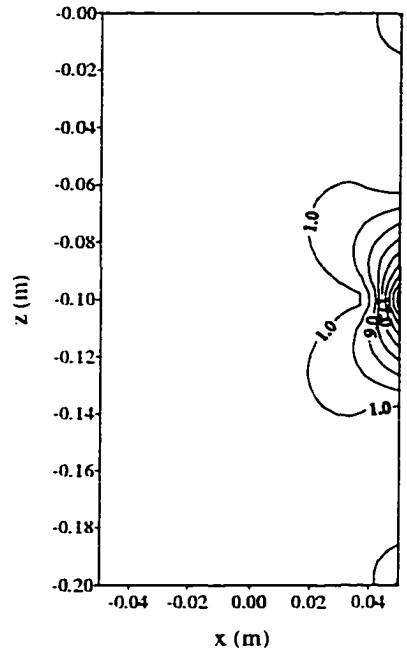

Figure 6.59: Matrix water pressure distributions in vertical plane, y = 0, t = 1 sec.

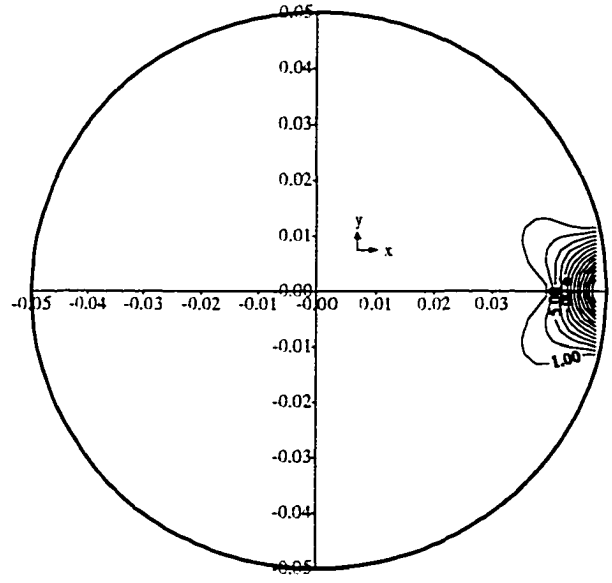

Figure 6.60: Matrix water pressures in horizontal plane, z = -0.1 m, t = 1 sec.

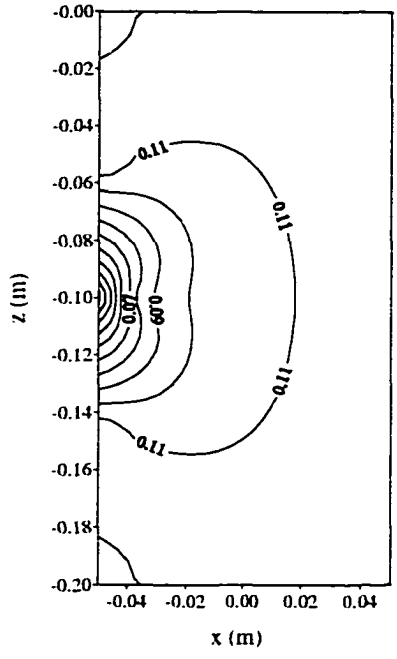

Figure 6.61: Matrix water pressure distributions in vertical plane, y = 0, t = 5 sec.

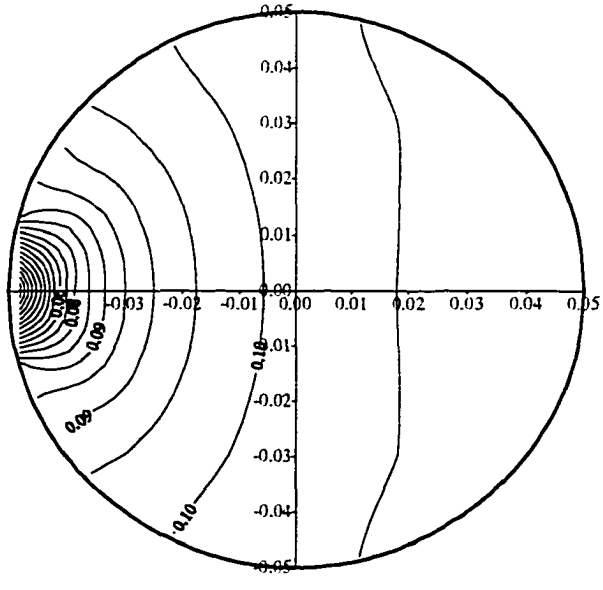

Figure 6.62: Matrix water pressures in horizontal plane, z = -0.1 m, t = 5 sec.

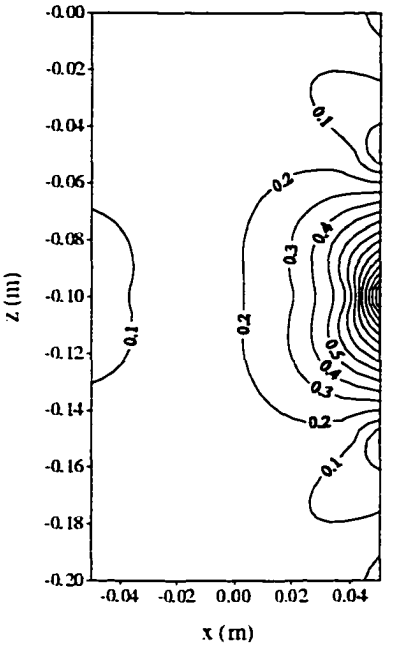

Figure 6.63: Fracture water pressures in vertical plane, y = 0, t = 1 sec.

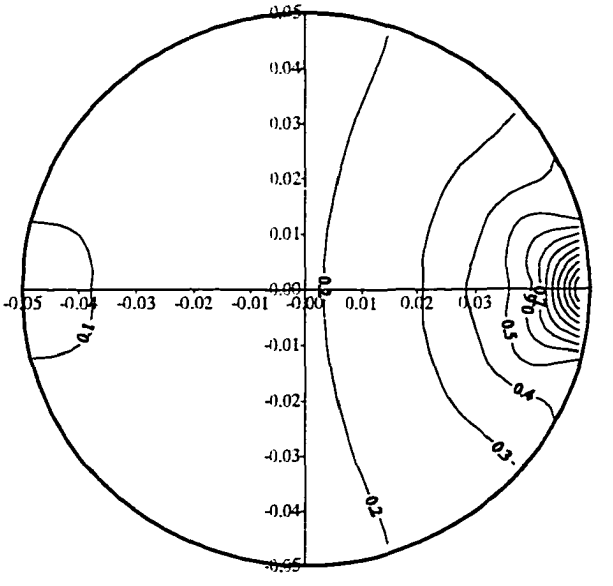

Figure 6.64: Fracture water pressures in horizontal plane, z = -0.1 m, t = 1 sec.

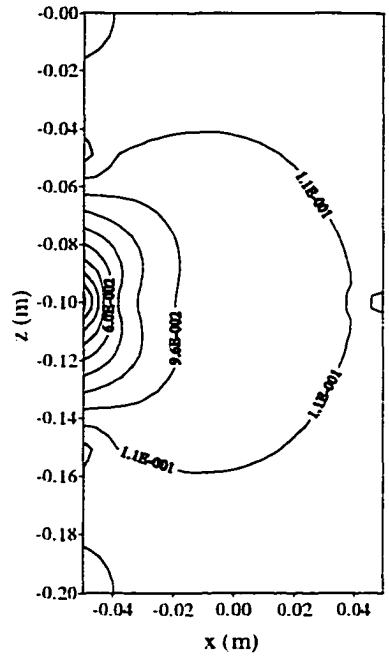

Figure 6.65: Fracture water pressures in vertical plane. y = 0. t = 5 sec.

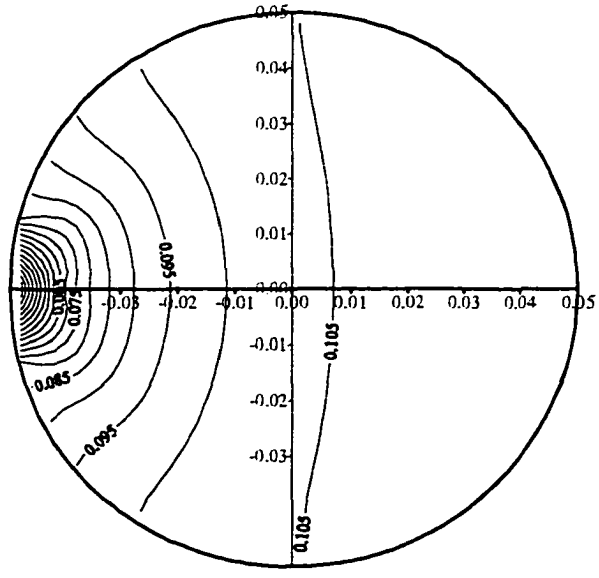

Figure 6.66: Fracture water pressures in horizontal plane, z = -0.1 m, t = 5 sec.

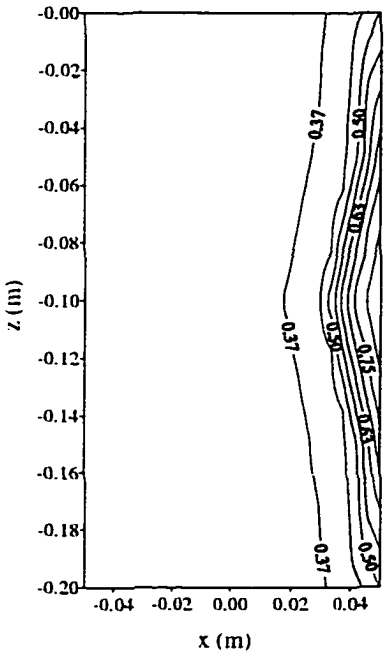

Figure 6.67: Matrix water saturation distributions in vertical plane. t = 1 sec.

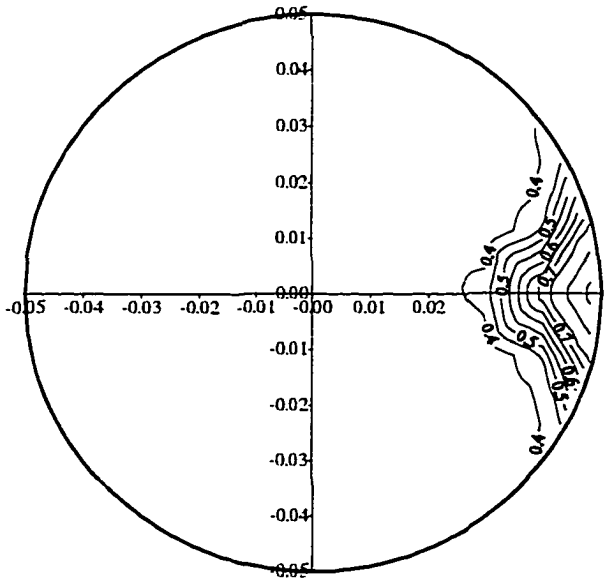

Figure 6.68: Matrix water saturations in horizontal plane, t = 1 sec.

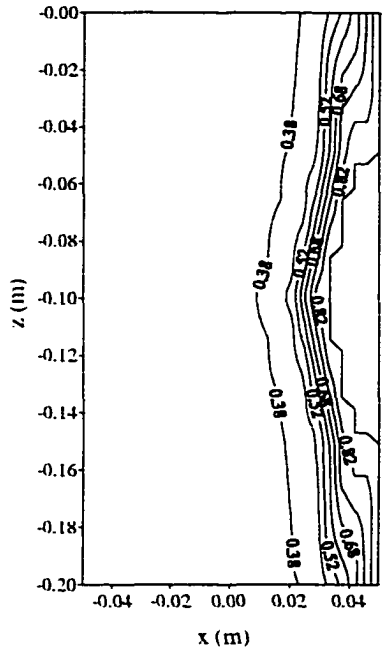

Figure 6.69: Matrix water saturation distributions in vertical plane. t = 5 sec.

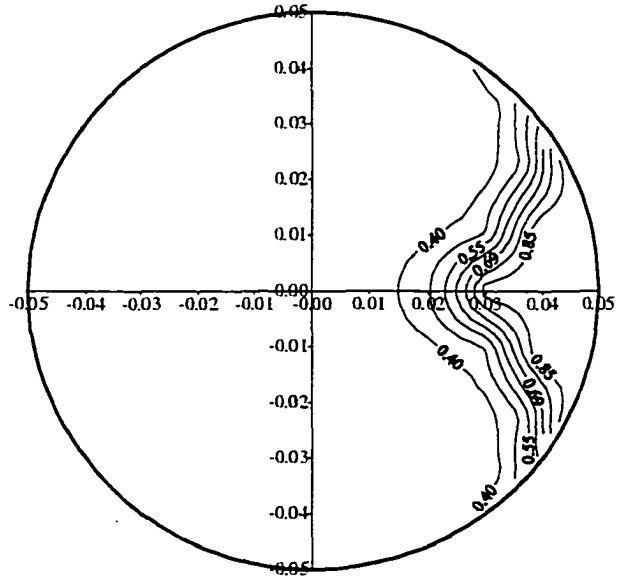

Figure 6.70: Matrix water saturations in horizontal plane, t = 5 sec.

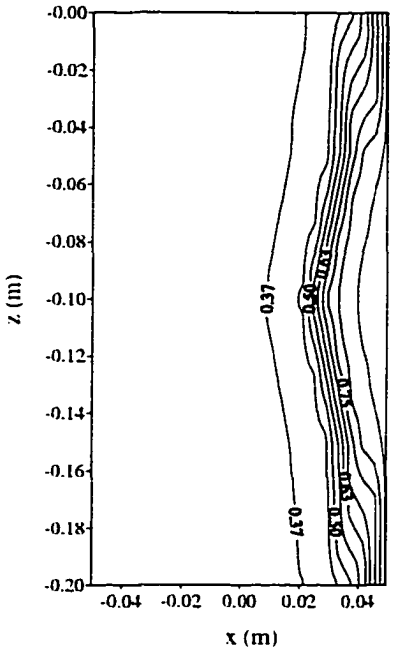

Figure 6.71: Fracture water saturation distributions in vertical plane, t = 1 sec.

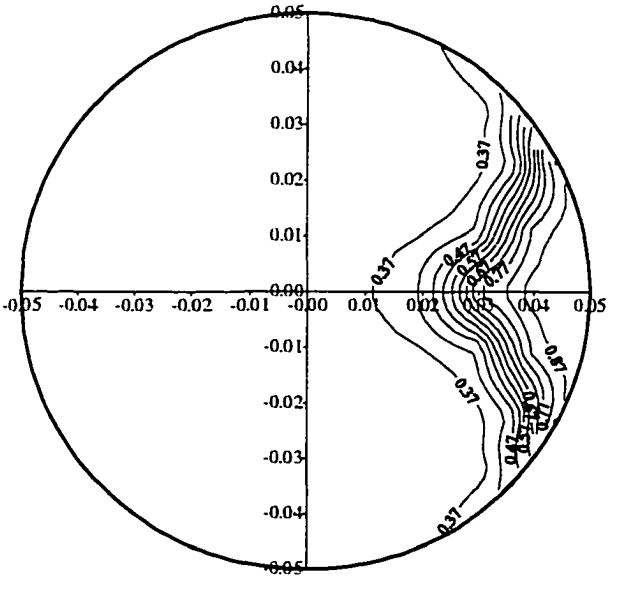

Figure 6.72: Fracture water saturations in horizontal plane, t = 1 sec.

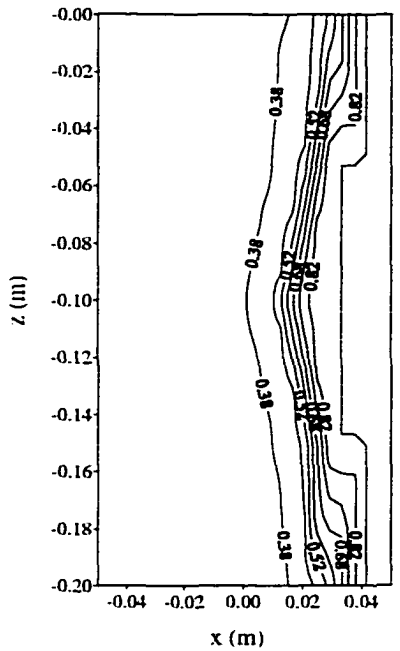

Figure 6.73: Fracture water saturation distributions in vertical plane, t = 5 sec.

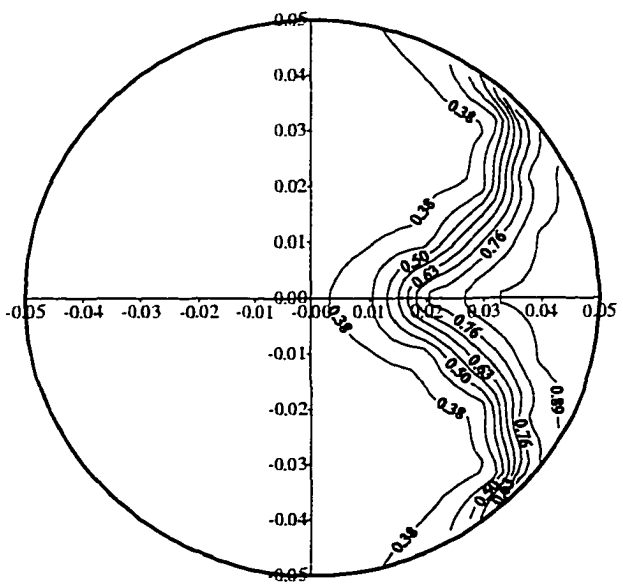

Figure 6.74: Fracture water saturations in horizontal plane, t = 5 sec.

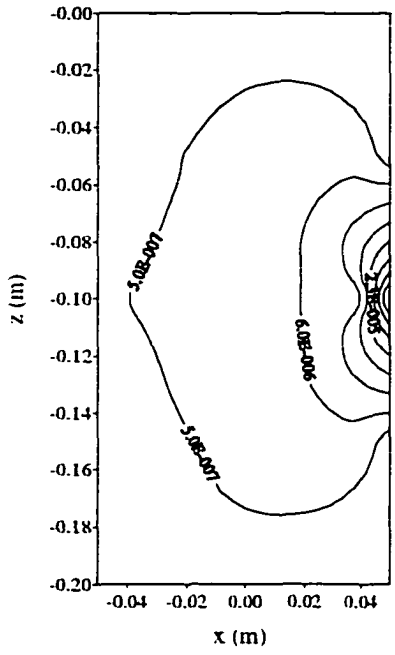

Figure 6.75: Displacement distributions along x-axis in vertical plane, t = 1 sec.

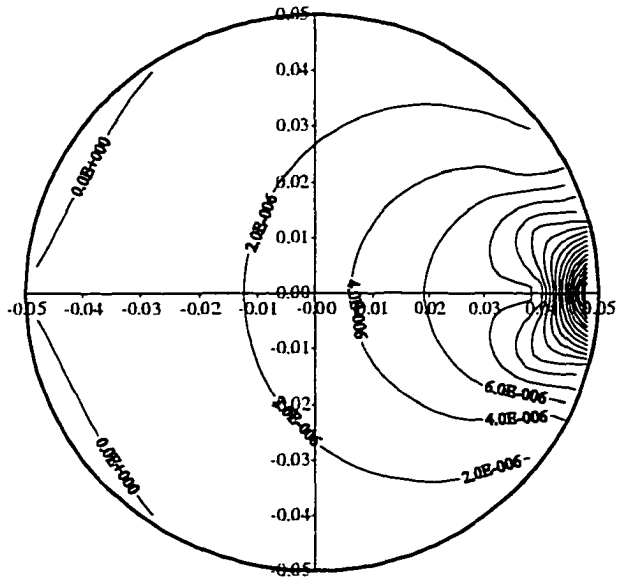

Figure 6.76: Displacements along x-axis in horizontal plane, t = 1 sec.

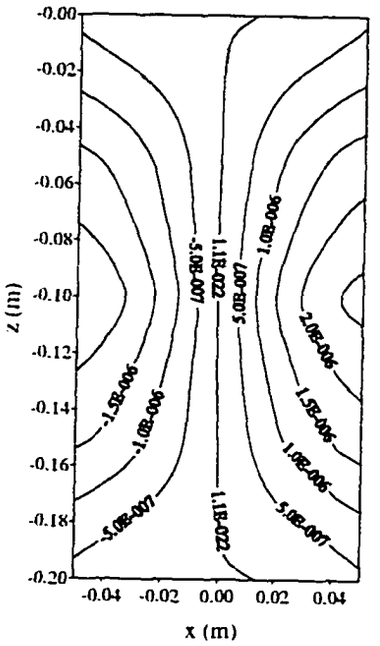

Figure 6.77: Displacement distributions along x-axis in vertical plane. t = 5 sec.

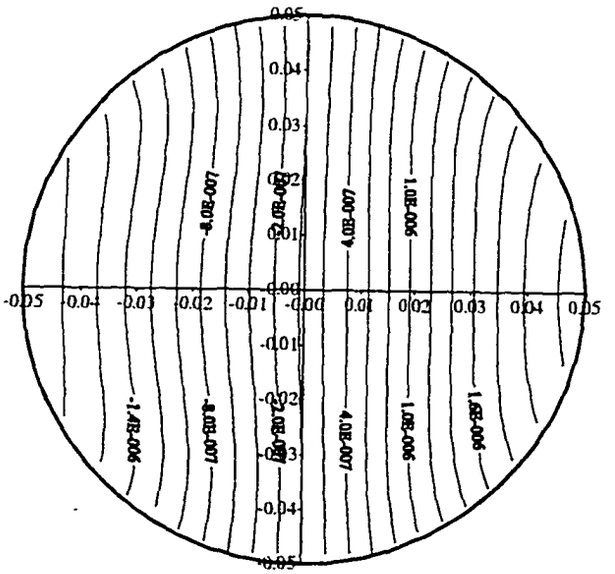

Figure 6.78: Displacements along x-axis in horizontal plane. t = 5 sec.

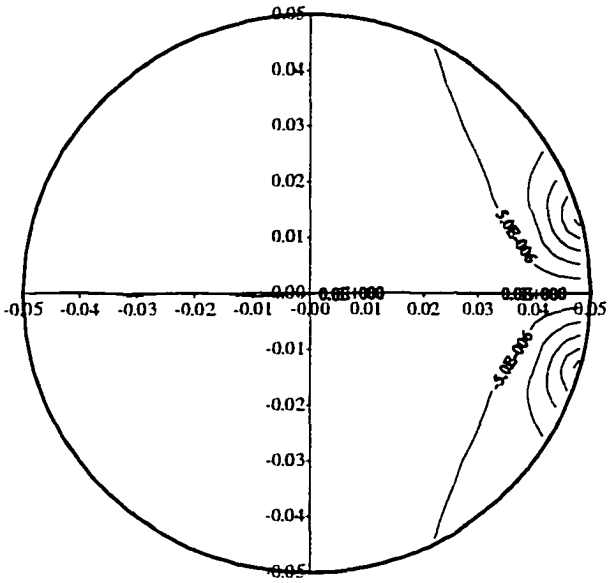

Figure 6.79: Displacement distributions along y-axis in horizontal plane. t = 1 sec.

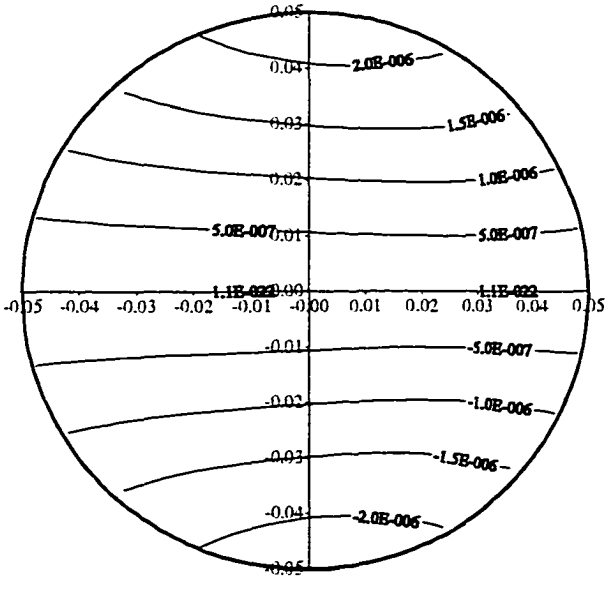

Figure 6.80: Displacements along y-axis in horizontal plane, t = 5 sec.

The rock sample is further considered to be subjected to an uniaxial loading at the top surface. The boundary and initial conditions are exactly same as previously, except the top surface moves in the vertical direction. The loading stress is equal to 10 MPa.

Figures 6.81 and 6.82 compare the results of the water pressures in both rock matrix and fracture systems with time for no-loading and loading cases. Both cases demonstrate the same trend in pressure changes. A larger pressure value is obtained in the loading case than in the no-loading case, which is reasonable because the loading stress will increase the pore pressures inside the rock sample.

The displacements along the x- (horizontal) and z- (vertical) directions are represented in Figures 6.83 and 6.84, respectively. As expected, larger displacement values are shown in Figure 6.83 under loading condition. The rock sample also shows larger expansions under loading condition.

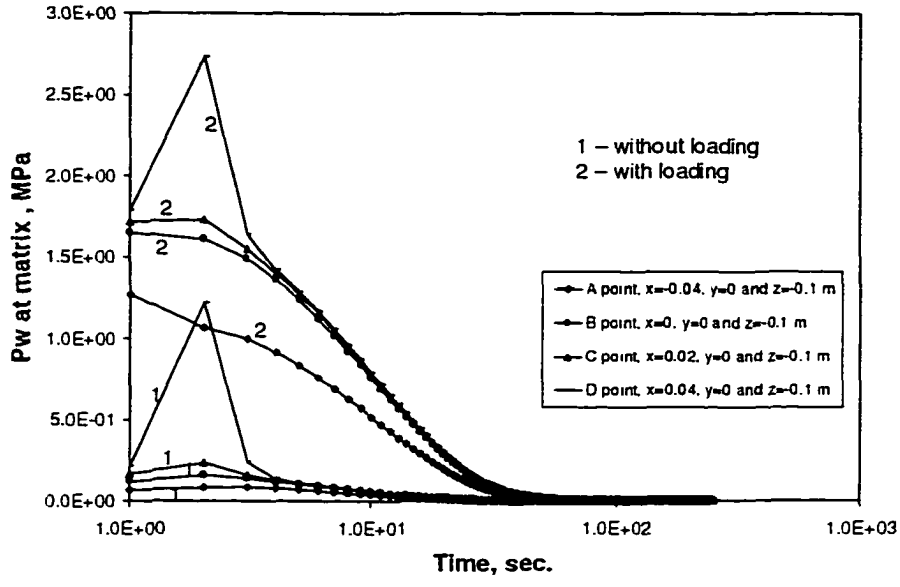

Figure 6.81: Matrix water pressures with time in no-loading and loading cases.

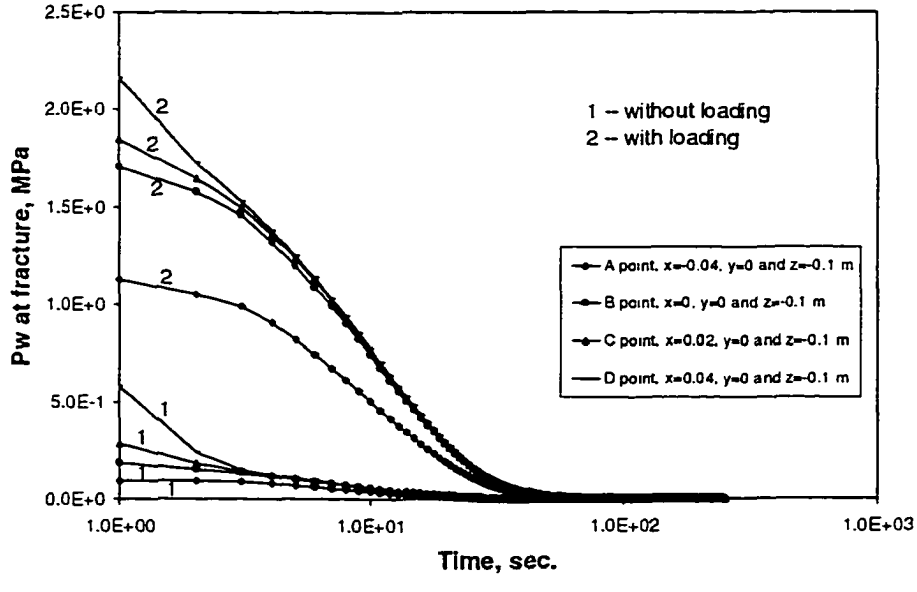

Figure 6.82: Fracture water pressures with time in no-loading and loading cases.

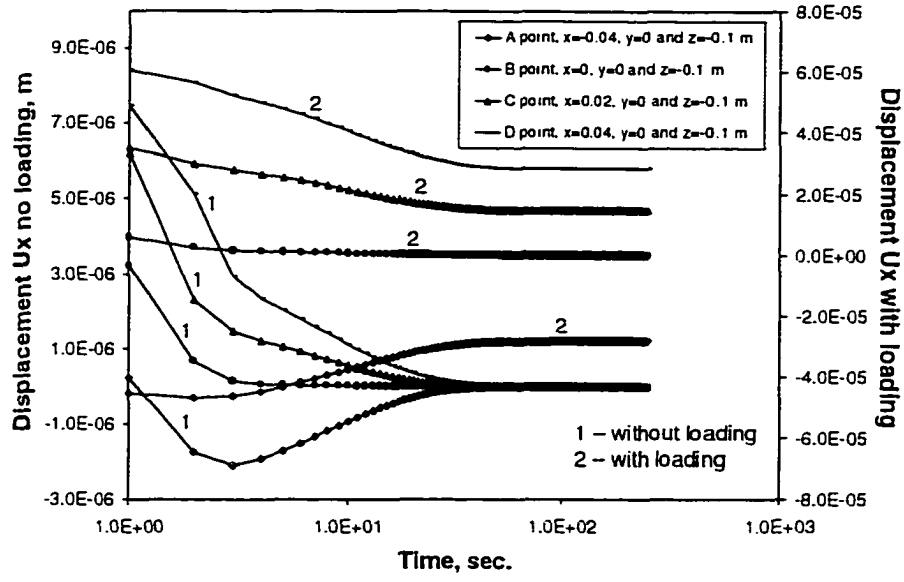

Figure 6.83: Displacements along x-axis with time in no-loading and loading cases.

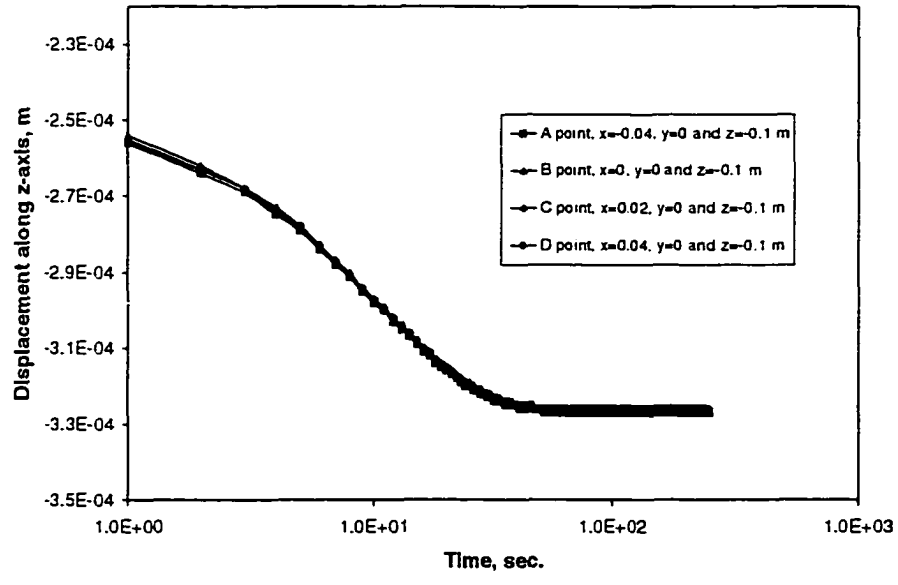

Figure 6.84: Displacements along z-axis with time in loading cases.

Chapter 7

Conclusions and Recommendations

7.1 Conclusions

This dissertation addressed the two-phase fluid flow problems in deformable naturally fractured reservoirs. Theoretical and numerical approaches were pursued. The dual-porosity system was used to describe the fractured porous medium in which different properties had been attributed to the rock matrix and the fractures. Theoretical and numerical efforts culminated in the developments of a fully coupled three-dimensional finite element code. It is believed that the developed numerical tool gives a more powerful means to solve different and difficult problems in petroleum engineering as well as in other engineering areas. The major conclusions and contributions of this study can be summarized as follows:

1. The derivations of the developed numerical model are based on the rigorous theory of the conservations of momentum and mass, rather than formulating the governing equations in a phenomenological background as shown in some current models. In comparison with the existing models for two-phase flow and solid deformation in fractured porous media, the present model offers more precise definition for the interactive responses between the matrix and

the fractures with respect to fluid flow.

2. A three-dimensional finite element code has been developed which properly simulates the coupled behaviors of the poroelastic solid and the two immiscible fluids in a deformable saturated fractured reservoir. The dual-porosity concept was applied to the fractured porous media, which means that the porous medium comprises fractures, with higher permeability and lower storage, as well as solid matrix, with lower permeability and higher storage.

3. The non-linear system of equations in the finite element model has been solved using the direct iteration method, in which each iteration is controlled by the error analyses of the unknowns. The elements of the matrix coefficients of the highly non-linear system are updated during each iteration in terms of the independent variables.

4. The performance of the developed numerical code has been extensively validated in three different categories. The first contains the simplest tests of the pure elasticity and the steady-state flow. The second simulates the consolidation problem for the coupled rock-fluid systems. Although those tests only involve single-phase flow and single-porosity they can, however, serve as a partial check for the present code. Finally, the problem of the two-phase flow in the deforming fractured porous medium was investigated. All the tested examples demonstrated the validity, stability and capability of the developed code.

5. The presented model gives more opportunities and choices to simulate different problems including uncoupled and coupled situations. The pure elastic problem and steady-state flow cases are typical examples of uncoupled problems. While several cases are involved in the coupled problems, for example

single-phase fluid flow in both single-porosity and dual-porosity media, and two-phase fluids flow also in both single-porosity and dual-porosity media.

6. The surface subsidence with dual-porosity presents more fast changes than the results obtained from single-porosity method. The fractured porous media behaviors depend on a large extent on the fracture properties. Two most important properties are the fracture permeability and fracture spacing which are negligible in single-porosity approach. Therefore, a dual-porosity model is more realistic in such cases than those with a conventional single-porosity model.

7. With increasing fracture permeability, both surface subsidences and fluid pressures change faster. Those behaviors demonstrate that if fracture permeability is higher, the fluid will flow faster in the fracture system which causes the fluid pressure to drop faster and subsidences increase faster. On the other hand, the smaller the fracture spacing is, the faster the subsidence occurs.

8. The studied examples in the parametric analysis show that for the fractured porous media the fluid pressures in the rock matrix are higher than the pressures in the fracture system, which may be explained as the fluid within the rock matrix is squeezed out into the fracture system due to the pressure difference. For the column problem, bigger difference between the rock matrix pressure and the fracture pressure is observed near the top surface than at the bottom of the column, which is attributed to the fact that the top surface is drained. In addition, the fluid interchange is also the functions of the fracture geometry.

9. For the two-phase flow in fractured porous media, the water saturations demonstrate larger changes in the fracture system than in the rock matrix. More oil

will flow into the fracture system so that the water saturation in the rock matrix will increase. From the fracture point of view, although oil flows into the fracture from the rock matrix, much more oil will move out from the drainage area leading to increase water saturation in the fractures. It is also noted that the capillary pressures will affect the saturation changes.

10. For all practical purposes, the developed model was used to simulate the behavior of laboratory rock samples. Several cases were studied which including combinations of horizontal injection, vertical injection, single-phase, two-phase, single-porosity, dual-porosity, no-loading and loading situations. Those simulations may be used for the future studies in stress-dependent permeability.

11. The developed model will be of great utility in simulating two-phase flow in deformable saturated oil reservoir. One typical example is waterflood. It also gives the opportunities to study the problems including single-phase fluid flow, reservoir subsidence, reservoir heterogeneity, groundwater flow and unsaturated zone problem in soil mechanics, and contaminant transport pollution in environment area.

7.2 Recommendations

The rigorous theoretical formulations and the finite element numerical scheme have been demonstrated through this dissertation. Yet only a few case studies were carried out. The followings are some implementation issues that need further research and developments:

1. additional material balance checks are needed after the convergence has been checked so that the model conserves mass at all times. This balance check

requires that the rate of fluid accumulation minus the divergence of velocity must be equal to the net flow of the reservoir system, i.e. total flow from any external source minus the total outflow from the reservoir;

2. the influence of choosing different element sizes needs further study, especially in the case of non-linear problems;

3. the convergence criterion may be influenced by the choice of the method to solve the non-linear equations, such as direct method, successive overrelaxation (SOR) and Newton-Raphson methods. Hence, this convergence criterion might probably be further optimized;

4. in the simulation, the value of Δt is assumed to be 1.0 second. In such case, the changes of the unknowns in the period of 0 to 1 second need to be further investigated. One method to deal with this problem is to take smaller value of Δt, such as 0.1 second and see how it influences the various pressure and displacement graphs;

5. conduct more case analyses for the actual fractured reservoir production problems;

6. extend the current model to simulate three-phase fluid flow problems;

7. examine the fracture properties, such as the effect of non-Darcy flow;

8. extend the presented theory to elastoplastic model to solve other problems like sanding control and borehole stability;

9. enable the model to study the stress-dependent permeability; and,

10. improve the code interface.

Nomenclature

$\mathbf{B}$	=	strain displacement matrix
C	=	compressibility
C_{ijkl}	=	elasticity compliance matrices (i, j, k, l=1, ... 3)
D_{ijkl}	=	elasticity matrices (i, j, k, l=1, ... 3)
E	=	Young's modulus
F_i	=	body force vector
J	=	Jacobian matrix
K	=	stiffness
K_t	=	bulk moduli of the solid skeleton
K_t^*	=	bulk moduli of the fractured media
K_s	=	bulk moduli of the solid grain
K_n	=	fracture normal stiffness
K_{sh}	=	fracture shear stiffness
K_1	=	fluid bulk moduli of rock matrix
K_2	=	fluid bulk moduli of fracture
K_{1w}	=	water bulk moduli of rock matrix
K_{1o}	=	oil bulk moduli of rock matrix
K_{2w}	=	water bulk moduli of fracture
K_{2o}	=	oil bulk moduli of fracture
k_{1ro}	=	oil relative permeability of rock matrix

k_{2ro} = oil relative permeability of fracture

k_{1rw} = water relative permeability of rock matrix

k_{2rw} = water relative permeability of fracture

L = differential operator

M = mass

N_i = interpolation functions or shape functions

n = number of normal set of fractures

P_1 = average pressure in rock matrix

P_2 = average pressure in fracture

P_{1o} = oil pressure in rock matrix

P_{2o} = oil pressure in fracture

P_{1w} = water pressure in rock matrix

P_{2w} = water pressure in fracture

P_c = capillary pressure

P_{1c} = capillary pressure of rock matrix

P_{2c} = capillary pressure of fracture

R = error

S_{1o} = oil saturation of rock matrix

S_{2o} = oil saturation of fracture

S_{1w} = water saturation of rock matrix

S_{2w} = water saturation of fracture

s = fracture spacing

t = time

u = velocity

u_{1w} = Darcy water velocity in rock matrix

u_{2w} = Darcy water velocity in fracture

u_{1o} = Darcy oil velocity in rock matrix

u_{2o} = Darcy oil velocity in fracture

U_{1w} = intrinsic water velocity in rock matrix

U_{2w} = intrinsic water velocity in fracture

U_{1o} = intrinsic oil velocity in rock matrix

U_{2o} = intrinsic oil velocity in fracture

V = total volume of the fractured porous medium

V_s = solid volume of the fractured porous medium

V_1 = pore volume of the fractured porous medium

V_2 = fracture volume of the fractured porous medium

V_p = total pore volume

W = weighting function

x, y, z = x, y, z directions in a cartesian coordinate system

Greeks

ε = strain

ε_{ij} = strain tensor (i, j=1, . . . , 3)

ε_{ij}^{I} = strain component I

ε_{ij}^{II} = strain component II

ε_{ij}^{III} = strain component III

ε_{kk} = volume strain

ν = Poisson's ration

ξ, η, ζ = ξ, η, ζ directions in a local coordinate system

ϕ_1 = rock matrix porosity

ϕ_2 = fracture matrix porosity

ϕ_s = solid matrix porosity

ρ_s = density of solid

ρ_{1w} = density of water in rock matrix

ρ_{1o} = density of oil in rock matrix

ρ_{2w} = density of water in fracture

ρ_{2o} = density of oil in fracture

Γ_w = rate of water transferred between the rock matrix and the fracture per unit volume

Γ_o = rate of oil transferred between the rock matrix and the fracture per unit volume

μ_{1w} = water viscosity in rock matrix

μ_{2w} = water viscosity in fracture

μ_{1o} = oil viscosity in rock matrix

μ_{2o} = oil viscosity in fracture

ϵ = convergence limit value

σ = stress

σ_{ij} = stress tensor (i, j=1, ..., 3)

σ'_{ij} = effective stress tensor (i, j=1, ..., 3)

$\bar{\sigma}$ = mean stress

α = Biot's constant

δ = Kronecker Delta

Ω = domain

Φ_i = unknown values at the nodes

Δt = time-step

∇ = Laplace operator

Subscripts

1 = rock matrix system

2 = fracture system

b	=	boundary domain
v	=	volume domain
s	=	solid system
w	=	water
o	=	oil
η	=	1 for rock matrix and 2 for fracture
π	=	w for water and o for oil

Superscripts

0	=	initial values
-1	=	inverse
k	=	iteration level
T	=	transpose
n	=	time

References

1. Aifantis E.C., Introducing a Multi-Porous Medium. *Developments in Mechanics*. Vol.8. p.209-211. 1977.

2. Aifantis E.C., On the Problem of Diffusion in Solids. *Acta Mechanica*. Vol.37. p.265-296. 1980.

3. Al-Dhahir Z.A. and Tan D.C., A Note on One-dimensional Constant-head Permeability Tests. *Geotechn.*, Vol.18. p.499-505. 1968.

4. Allen D.R., Physical Changes of Reservoir Properties Caused by Subsidence and Repressurizing Operations. Wilmington Field. California. *JPT*. p.23-29. 1968.

5. Aziz K. and Settari A., *Petroleum Reservoir Simulation*. Elsevier Applied Science Publishers. New York. 1979.

6. Bai M., Elsworth D. and Roegiers J.-C., Multi-Porosity/Multi-Permeability Approach to the Simulation of Naturally Fractured Reservoirs. *Water Resour. Res.*, Vol.29. No.6, p.1621-1633, 1993.

7. Bai M., Ma Q. and Roegiers J.-C., A Nonlinear Dual-Porosity Model, *Appl. Math. Modelling*, Vol. 18, p.602-610, 1994.

8. Bai M. and Meng F.H., Study of Naturally-Fractured Reservoirs Using Three-Dimensional Finite Elements, *Report for the Rock Mechanics Research Insti-*

tute. The University of Oklahoma. Nov., 1994.

9. Bai M. and Roegiers J.-C., On the Correlation of Nonlinear Flow and Linear Transport with Application to Dual-Porosity Modeling, *J. Pet. Sci. Eng.*, Vol.11, p.63-72, 1994.

10. Bai M., Elsworth D., Roegiers J.-C. and Meng F.H., A Three-Dimensional Dual-Porosity Poroelastic Model, *International Symposium on mining Technology: Rock Mechanics and Strata Control in Mining and Geological Engineering*, Beijing, China, 1995.

11. Bai M., Roegiers J.-C. and Elsworth D., Poromechanical Response of Fractured-Porous Rock Masses, *Journal of Petroleum Science and Engineering* , Vol.13, p.155-168, 1995.

12. Bai M. and Roegiers J.-C., Modeling of Heat Flow and Solute Transport in Fractured Rock Masses, *Proc. 8th Int. Congress Rock Mechanics*, Japan, 1995.

13. Barenblatt G.I., Zheltov I.P. and Kochina I.N., Basic Concepts in the Theory of Seepage of Homogeneous Liquids in Fissured Rocks, *Prikl. Mat. Mekh.*, Vol.24, No.5, p.852-864, 1960.

14. Bear J., *Dynamics of Fluids in Porous Media*, Dover Publications, Inc., New York, 1988.

15. Biot M.A., General Theory of Three-Dimensional Consolidation, *J. Appl. Phys.*, Vol.12, p.155-164, 1941.

16. Biot M.A., Theory of Elasticity and Consolidation for a Porous Anisotropic Media, *J. Appl. Phys.*, Vol.26, p.182-185, 1955.

17. Bossie-Codreanu D., Bia P.R. and Sabathier J.C., The "Checker Model " Improvement in Modeling Naturally Fractured Reservoirs with a Tridimensional, Triphasic, Black-Oil Numerical Model. *Soc. Pet. Eng. J.*, p.743-756, 1985.

18. Brace W.F., Walsh J.B. and Frangos W.T., Permeability of Granite under High Pressure. *J. Geophys. Res.*, Vol.73, p.2225-2236, 1968.

19. Braester C., Simultaneous Flow of Immiscible Liquids Through Porous Media. *Soc. Pet. Eng. J.*, p.297-305, 1972.

20. Bruce G.H., Peaceman D.W. and Rachford H.H., Calculation of Unsteady-State Gas Flow Through Porous Media. *Petrol. Trans. AIME 198.* p.74-92, 1953.

21. Charlez P.A., Rock Mechanics. *Volume 1, Theoretical Fundamentals.* Editions Technip, Paris, 1991.

22. Chin L.Y. and Prévost J.H., Three-Dimensional Computer Modeling of Coupled Geomechanics and Multiphase Flow. *Computer Methods and Advances in Geomechanics.* p.1171-1176, Balkema, Rotterdam, 1997.

23. Committee on Fracture Characterization and Fluid Flow. *Rock Fractures and Fluid Flow - Contemporary Understanding and Applications.* National Academy Press, Washington, D.C., 1996.

24. Dagger M.A.S., A Fully-Coupled Two-Phase Flow and Rock Deformation Model for Reservoir Rock, *Ph.D dissertation*, the University of Oklahoma, 1997.

25. Detournay E. and Cheng A.H-D., Poroelastic Response of a Borehole in a Non-Hydrostatic Stress Field, *Int. J. Rock Mech. Min. Sci. Geomech. Abstr.*, Vol.25, No.3, p.171-182, 1988.

26. Detournay E. and Cheng A.H-D., Fundamental of Poroelasticity, Ch.5 in *Comprehensive Rock Engineering*, Vol.2, Editor, Fairhurst C., Pergamon Press, 1993.

27. Duguid J.O. and Abel J., Finite Element Galerkin Method for Flow in Fractured Porous Media, in Finite Element Methods in Flow Problems, Oden J.T., Zienkiewicz O.C., Gallagher R.H. and Taylor C., eds., p.599-615, University of Alabama Press, Huntsville, 1974.

28. Duguid J.O. and Lee P.C.Y., Flow in Fractured Porous Media, *Water Resources Research*, Vol.13, No.3, p.558, 1977.

29. Elsworth D. and Bai M., Flow-Deformation Response of Dual-Porosity Media, *Journal of Geotechnical Engineering*, Vol.118, No.1, Jan. 1992.

30. Evans R.D., A Proposed Model for Multiphase Flow Through Naturally Fractured Reservoirs, *SPE Paper*, No. 9940, SPE-AIME, Dallas, TX, 1981.

31. Finol A. and Farouq Ali M., Numerical Simulation of Oil Production with Simultaneous Ground Subsidence, *SPEJ*, Vol.15, p.411-424, 1975.

32. Freeze R.A. and Witherspoon P.A., Theoretical Analysis of Regional Groundwater Flow: 1. Analytical and Numerical Solutions to the Mathematical Model, *Water Resour. Res.*, Vol.2, p.641-656, 1966.

33. Gambolati G., Gatto P. and Freeze R.A., Mathematical Simulation of the Subsidence of Venice, 2, Results, *Water Resour. Res.*, Vol.9, p.721-733, 1973.

34. Gawin D., Simoni L. and Schrefler B.A., Numerical Model for Hydro-Mechanical Behaviour in Deformable Porous Media: A Benchmark Problem, p.1171-1176, Balkema, Rotterdam, 1997.

35. Ghafouri H.R. and Lewis R.W., A Finite Element Double Porosity Model for Heterogeneous Deformable Porous Media. *Int. J. Analytic. Numer. Meth. Geomech.*, Vol.20, p.831-844, 1996.

36. Gilman J.R., An efficient Difference Method for Simulating Phase Segregation in the Matrix Blocks in Double-Porosity Reservoirs. *Soc. Pet. Eng. J.*, p.403-413, July, 1986.

37. Gilman J.R. and Kazemi H., Improved Calculations for Viscous and Gravity Displacement in Matrix Blocks in Dual-Porosity Simulators. *J. Pet. Tech.*, p.60-70, Jan., 1988.

38. Gupta S.K. and Tanki K.K., A Three-Dimensional Galerkin Finite Element Solution of Flow Through Multiaquifers in Sutter Basin, California. *Water Resour. Res.*, Vol.12, No.2, p.155-162, 1976.

39. Hill A.C. and Thomas G.W., A New Approach for Simulating Complex Fractured Reservoirs. *SPE Paper*, No. 13537. SPE-AIME, Dallas, TX, 1985.

40. Istok J., *Groundwater Modeling by the Finite Element Method*. Water Resources Monograph 13, American Geophysical Union, 1989.

41. Jaeger J.C. and Cook N.G.W., *Fundamentals of Rock Mechanics*. Chapman and Hall, 1979.

42. Javandel I. and Witherspoon P.A., Application of the Finite Element Method to Transient Flow in Porous Media, *Society of Petroleum Engineers Journal*, Vol.8, No.3, p.241-252, 1968.

43. Kazemi H., Seth M.S. and Thomas G.W., The Interpretation of Interference Tests in Naturally Fractured Reservoirs with Uniform Fracture Distribution, *Soc. Pet. Eng. J.*, 9, p.463-472, 1969a.

44. Kazemi H., Pressure Transient Analysis of Naturally Fractured Reservoirs with Uniform Fracture Distribution, *Soc. Pet. Eng. J.*, 9, p.451-462, 1969b.

45. Kazemi H. and Gilman J.R., Multiphase Flow in Fractured Petroleum Reservoirs, *Flow and Contaminant Transport in Fractured Rock*, p.267-270, Academic Press, Inc., 1993.

46. Kazemi H., Merril L.S. Jr., Porterfield K.L. and Zeman P.R., Numerical Simulation of Water-Oil Flow in Naturally Fractured Reservoirs, *Soc. Pet. Eng. J.*, 16, p.317-326, 1975.

47. Khaled M.Y., Beskos D.E. and Aifantis E.C., On the Theory of Consolidation with Double Porosity - III A Finite Element Formulation, *Int. J. Analytic. Numer. Meth. Geomech.*, Vol.8, p.101-123, 1984.

48. Klubertanz G., Laloui L. and Vulliet L., Numerical Modeling of Unsaturated Porous Media as a Two and Three Phase Medium: A Comparison, *Computer Methods and Advances in Geomechanics*, p.1171-1176, Balkema, Rotterdam, 1997.

49. Lewis R.W. and Ghafouri H.R., A Novel Finite Element Double Porosity Model for Multiphase Flow Through Deformable Fractured Porous Media, *Int. J. Analytic. Numer. Meth. Geomech.*, Vol.21, p.789-816, 1997.

50. Lewis R.W. and Schrefler B.A., The Finite Element Method in the Deformation and Consolidation of Porous Media, *Wiley, Chichester*, 1987.

51. Lewis R.W. and Sukirman Y., Finite Element Modeling of Three-Phase Flow in Deforming Saturated Oil Reservoirs, *Int. J. Analytic. Numer. Meth. Geomech.*, Vol.17, p.577-598, 1993a.

52. Lewis R.W. and Sukirman Y., Finite Element Modeling for Simulating the Surface Subsidence above a Compacting Hydrocarbon Reservoir. *Int. J. Analytic. Numer. Meth. Geomech.*, Vol.18, p.619-639, 1993b.

53. Li X. and Fan Y., Finite Element Analysis of Transient Deformation and Seepage Process in Unsaturated Soils. *Computer Methods and Advances in Geomechanics*, p.1171-1176, Balkema, Rotterdam, 1997.

54. Li X. and Zienkiewicz O.C., Multiphase Flow in Deforming Porous Media and Finite Element Solutions, *Computer & Structures*, Vol.45, No.2, p.211-227, 1992.

55. Li X., Zienkiewicz O.C. and Xie Y.M., A Numerical Model for Immiscible Two-Phase Fluid Flow in a Porous Medium and Its Time Domain Solution, *Int. J. for Numer. Meth. in Eng.*, Vol.30, p.1195-1212, 1990.

56. Marius J.M., Ekofisk Reservoir Voidage and Seabed Subsidence, *JPT*, p.1434-1438, 1990.

57. Mattax C.C. and Dalton R.L., Reservoir Simulation, *SPE Monograph*, Vol.13, 1990.

58. Mattax C.C. and Kyte J.R., Imbibition Oil Recovery from Fractured, Water-Drive Reservoirs, *Soc. Pet. Eng. J., Trans.*, AIME, Vol.225, p.177-184, 1962.

59. Matthews C.S. and Russell D.G., Pressure Buildup and Flow Tests in Wells, *SPE Monograph*, Vol.1, 1967.

60. Merle H.A., The Bachaquero-Study: A Composite Analysis of the Behavior of a Compaction Drive/Solution Gas Drive Reservoir, *JPT*, p.1107-1114, 1976.

61. Morin R.H. and Olsen H.W., Theoretical Analysis of the Transient Pressure Response from a Constant Flow Rate Hydraulic Conductivity Test. *Water Resources Res.*, Vol.23, p.1461-1470, 1987.

62. Nakornthap K. and Evans R.D., Numerical Simulation and Reservoir Characterization of Multiphase Fluid Flow in Naturally Fractured Formations. *SPE 15130*, 1986.

63. Neumann S.P. and Witherspoon P.A., Finite Element Method of Analyzing Steady Seepage With a Free Surface. *Water Resour. Res.*, Vol.6, No.3, p.889-897, 1970.

64. Noorishad J., Ayatollahi M.S. and Witherspoon P.A., A Finite Element Method for Coupled Stress and Fluid Flow Analysis in Fractured Rock Masses. *Int. J. Rock Mech. Min. Sci. & Geomech. Abstr.*, Vol.19, p.185-192, 1982.

65. Nur A. and Byerlee J.D., An Exact Effective Stress Law for Elastic Deformation of Rock with Fluids. *J. Geophys. Res.*, Vol.76, No.26, p.6414-6419, 1971.

66. Odeh A.S., Unsteady-state Behavior of Naturally Fractured Reservoirs. *Soc. Pet. Eng. J.*, 5, p.60-66, 1965.

67. Peter S.H. and Geogre F.P., *Computational Methods in Subsurface Flow*, Academic Press, Inc., New York, 1983.

68. Pinder G.F. and Bredehoeft J.D., Application of the Digital Computer for Aquifer Evaluation, *Water Resour. Res.*, Vol.4, p.1069-1093, 1968.

69. Pinder G.F. and Frind E.O., Application of Galerkin's Procedure to Aquifer Analysis, *Water Resour. Res.*, Vol.8, No.1, p.108-120, 1972.

70. Price H.S., Cavendish J.C. and Varga R.A., Numerical Methods of Higher Order Accuracy for Diffusion Convection Equations. *Society of Petroleum Engineers Journal*, p.293-303, 1968.

71. Pruess K. and Tsang Y.W., On Two-Phase Relative Permeability and Capillary Pressure of Rough-Walled Rock Fractures. *Water Resources Research*, Vol.26, No.9, p.1915-1926, Sept., 1990.

72. Reiss L.H., Bossie-Codreanu D. and Lefebvre du Prey E.J., Flow in Fissured Reservoir. *SPE Paper*, No.4343, London, 1973.

73. Rossen R.J., Simulation of Naturally Fractured Reservoirs with Semi-Implicit Source Terms. *Soc. Pet. Eng. J.*, 17, p.201-210, 1977.

74. Settari A. and Aziz K., Treatment of Nonlinear Terms in the Numerical Solution of Partial Differential Equations for Multiphase Flow in Porous Media. *Int. J. Multiphase Flow*, Vol.1, p.817-844, Pergamon/Elsevier, 1975.

75. Schoonbeek J.B., Land Subsidence as a Result of Natural Gas Extraction in the Province of Groningen, *SPE Paper*, No.5751, 1976, p.23-29, 1968.

76. Schrefler B.A. and Zhan X., A Fully Coupled Model for Water Flow and Airflow in Deformable Porous Media, *Water Resour. Res.*, Vol.29, No.1, p.155-167, 1993.

77. Shu Z.Y., Personal Communication, 1998.

78. Skempton A.W., The Pore-Pressure Coefficients A and B, *Geotechnique*, Vol.4, p.143-147, 1954.

79. Sun Y., Sakajo S. and Nishigaki M., Application Research on a Numerical

Model of Two-Phase Flows in Deformation Porous Medium, *Computer Methods and Advances in Geomechanics*, p.1171-1176, Balkema, Rotterdam, 1997.

80. Swann A., Analytical Solutions for Determining Naturally Fractured Reservoir Properties by Well Testing, *Soc. Pet. Eng. J.*, 6, p.117-122, 1976.

81. Swann A., Theory of Waterflooding in Fractured Reservoirs, *Soc. Pet. Eng. J.*, 4, p.117-122, 1978.

82. Terzaghi K., *Theory Soil Mechanics*, John Wiley & Sons, New York, N.Y., 1943.

83. Thomas L.K., Dixon T.N. and Pierson R.G., Fractured Reservoir Simulation, *Soc. Pet. Eng. J.*, p.42-54, 1983.

84. Trescott P.C. and Larson S.P., Comparison of Iterative Methods for Solving Two-dimensional Groundwater Flow Equations, *Water Resour. Res.*, Vol.13, No.1, p.125-136, 1977.

85. Walsh J.B., Effect of Pore Pressure and Confining Pressure on Fracture Permeability, *Int. J. Rock Mech. Min. Sci. Geomech. Abstr.*, Vol.18, No.3, p.429-435, 1981.

86. Warren J.E. and Root P.J., The Behavior of Naturally Fractured Reservoirs, *Soc. Pet. Eng. J., Trans.*, AIME, Vol.228, p.245-255, 1963.

87. Williams J.L., The Influence of Induced Vertical Fractures on Overall Reservoir Performance, *SPE Paper*, No.6381, Midland, TX, March, 1977.

88. Wilson R.K. and Aifantis E.C., On the Theory of Consolidation with Double Porosity, *Int. J. Eng. Sci.*, Vol.20, No.9, p.1009-1035, 1982.

89. Wu Y.S. and Pruess K., A Multiple-Porosity Method for Simulation of Naturally Fractured Petroleum Reservoirs, *SPE Reservoir Engineering*, p.327-336, 1988.

90. Zaman M., Gopalasingam A. and Laguros J.G., Consolidation Settlement of Bridge Approach Foundation, Journal of Geotechnical Engineering, Vol. 117, No.2, p.219-240, 1991.

91. Zienkiewicz O.C. and Parekh C.J., Transient Field Problems: Two-Dimensional and Three-Dimensional Analysis by Isoparametric Finite Elements, *International Journal of Numerical Methods in Engineering*, Vol.2, p.61-71, 1970.

92. Zienkiewicz O.C., *The Finite Element Method*, McGraw-Hill, 3rd edition, New York, 1977.

Appendix A

Derivations of Volume Changes

These basic derivations are based on Charlez's book (1991).

A.1 Decomposition of the State of Stress

The constitutive law of the equivalent material can be determined easily by decomposing the actual state of stress into three elementary components according to Figure A.1.

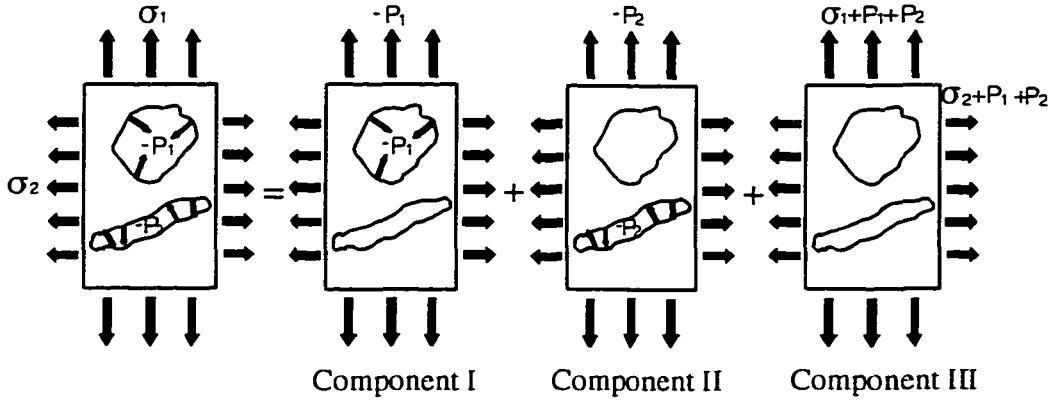

Figure A.1: Decomposition of the stress state.

Hooke's law is written as:

$$\varepsilon_{ij} = \frac{1+\nu}{E}\sigma_{ij} - \frac{\nu}{E}\sigma_{kk}\delta_{ij} \tag{A.1}$$

where E is Young's modulus; ν is Poisson's ratio; $\sigma_{kk} = \sigma_{xx} + \sigma_{yy} + \sigma_{zz}$ for the three-dimensional stress conditions and δ_{ij} is *the Kronecker delta.*

- Component I corresponds to the hydrostatic loading of the matrix and leads to a deformation state ε_{ij}^{I} :

$$\varepsilon_{ij}^{I} = -\frac{P_1}{3K_s}\delta_{ij} \tag{A.2}$$

  where K_s is the bulk modulus of the solid grain.

- Component II corresponds to the hydrostatic loading of the fracture and leads to a deformation state ε_{ij}^{II} :

$$\varepsilon_{ij}^{II} = -\frac{P_2}{3K_n s}\delta_{ij} \tag{A.3}$$

  where $3K_n$ is the fracture stiffness and s is the fracture spacing.

- Component III corresponds to the loading of the dry equivalent material and leads to a deformation state ε_{ij}^{III} :

$$\varepsilon_{ij}^{III} = \frac{1+\nu}{E}\left(\sigma_{ij} + P_1\delta_{ij} + P_2\delta_{ij}\right) - \frac{\nu}{E}\left(\sigma_{kk} + 3P_1 + 3P_2\right)\delta_{ij} \tag{A.4}$$

The overall strain is obtained by adding Equations (A.2), (A.3) and (A.4) which leads to:

$$\varepsilon_{ij} = \frac{1+\nu}{E}\sigma_{ij} - \frac{\nu}{E}\sigma_{kk}\delta_{ij} + \left(\frac{1}{K_t} - \frac{1}{K_s}\right)\frac{P_1}{3}\delta_{ij} + \left(\frac{1}{K_t} - \frac{1}{K_n s}\right)\frac{P_2}{3}\delta_{ij} \tag{A.5}$$

where K_t is the bulk modulus of the equivalent dry material.

The effective stress can be written as (Nur and Byerlee, 1971):

$$\sigma_{ij}^{'} = \sigma_{ij} + \alpha_1 P_1\delta_{ij} + \alpha_2 P_2\delta_{ij} \tag{A.6}$$

with,

$$\begin{cases} \alpha_1 = 1 - \dfrac{K_t}{K_s} \\ \alpha_2 = 1 - \dfrac{K_t}{K_n s} \end{cases} \tag{A.7}$$

$$\sigma'_{kk} = \sigma_{kk} + 3\alpha_1 P_1 + 3\alpha_2 P_2 \tag{A.8}$$

Substituting Equations (A.6), (A.7) and (A.8) into Equation (A.5), it follows:

$$\varepsilon_{ij} = \frac{1+\nu}{E}\sigma'_{ij} - \frac{\nu}{E}\sigma'_{kk}\delta_{ij} \tag{A.9}$$

It shows that the effective stresses and not the total stresses govern the strain of a fractured porous elastic material.

A.2 Bulk Volume Variations

The bulk volume variations can easily be obtained from Hooke's law (Equation (A.5)). The volume strain ε_{kk} is such that:

$$\varepsilon_{kk} = \frac{\Delta V}{V} = \frac{1}{K_t}\left(\frac{\sigma_{kk}}{3} + P_1 + P_2\right) - \frac{P_1}{K_s} - \frac{P_2}{K_{ns}} \tag{A.10}$$

A.3 Variation in Total Pore Volume

It is clear that the variation of total pore volume is generated by normal stress components. The normal total stress can be decomposed into two parts with $\overline{\sigma} = \frac{\sigma_{kk}}{3}$:

$$\sigma_{ij} = \overline{\sigma}\delta_{ij} + (\sigma_{ij} - \overline{\sigma}\delta_{ij}) \tag{A.11}$$

The analysis of the variations in total pore volume also can be divided into two parts:

1. the pore volume variations due to mean stresses and pressures, i.e. $\overline{\sigma}$, P_1 and P_2; and,

2. the pore volume variations due to deviatoric stresses, i.e. $\sigma_{ij} - \overline{\sigma}\delta_{ij}$.

A.3.1 Pore Volume Change Due to Mean Stresses and Pressures

The total pore volume is the sum of the matrix pore volume and the fracture volume, *i.e.* $V_p = V_1 + V_2$. The total pore volume and the bulk volume are assumed to be a function of the mean stress $\overline{\sigma}$ and pressures P_1 and P_2. The relative variations in total pore volume will, therefore, be such that:

$$\frac{dV_p}{V_p} = \frac{1}{V_p}\left(\frac{\partial V_p}{\partial \overline{\sigma}}\right) d\overline{\sigma} + \frac{1}{V_p}\left(\frac{\partial V_p}{\partial P_1}\right) dP_1 + \frac{1}{V_p}\left(\frac{\partial V_p}{\partial P_2}\right) dP_2 \tag{A.12}$$

To eliminate $\left(\frac{\partial V_p}{\partial \overline{\sigma}}\right)$ from Equation (A.12), consider the stress path $d\overline{\sigma} = -dP_1 - dP_2$. Then Equations (A.2), (A.3) and (A.10) lead to:

$$\frac{dV}{V} = -\frac{dP_1}{K_s} - \frac{dP_2}{K_n s} = \varepsilon_{kk}^{I} + \varepsilon_{kk}^{II} = \frac{dV_s}{V_s} \tag{A.13}$$

Since $dV_p = dV - dV_s$, taking account of Equation (A.13) one gets:

$$dV_p = -\left(\frac{dP_1}{K_s} + \frac{dP_2}{K_n s}\right)(V - V_s) = -\left(\frac{dP_1}{K_s} + \frac{dP_2}{K_n s}\right) V_p \tag{A.14}$$

Equations (A.13) and (A.14) lead to the identity with $d\overline{\sigma} = -dP_1 - dP_2$:

$$\frac{dV}{V} = \frac{dV_s}{V_s} = \frac{dV_p}{V_p} = -\frac{dP_1}{K_s} - \frac{dP_2}{K_n s} \tag{A.15}$$

Since $d\overline{\sigma} = -dP_1 - dP_2$, Equation (A.12) will be written by taking account of Equation (A.15) as:

$$-\frac{dP_1}{K_s} - \frac{dP_2}{K_n s} = -\frac{1}{V_p}\left(\frac{\partial V_p}{\partial \overline{\sigma}}\right) dP_1 - \frac{1}{V_p}\left(\frac{\partial V_p}{\partial \overline{\sigma}}\right) dP_2 + \frac{1}{V_p}\left(\frac{\partial V_p}{\partial P_1}\right) dP_1 + \frac{1}{V_p}\left(\frac{\partial V_p}{\partial P_2}\right) dP_2 \tag{A.16}$$

By eliminating $\frac{\partial V_p}{\partial P_1}$ and $\frac{\partial V_p}{\partial P_2}$ between Equations (A.12) and (A.16), the following equation is obtained:

$$\frac{dV_p}{V_p} = -\left(\frac{dP_1}{K_s} + \frac{dP_2}{K_n s}\right) + \frac{1}{V_p}\left(\frac{\partial V_p}{\partial \overline{\sigma}}\right)(d\overline{\sigma} + dP_1 + dP_2\ ) \tag{A.17}$$

A.3.2 Betty's Reciprocity Theorem

The final expression of the variation in total pore volume for a material subjected to an increment $d\overline{\sigma}$ of mean total stress and to the variations dP_1 and dP_2 of pressures, is obtained by applying Betty's reciprocity theorem to two transformations: on one hand the case in which the mean total stress varies between $\overline{\sigma}$ and $\overline{\sigma} + d\overline{\sigma}$ whereas the pressures remain constant and, on the other, that in which $\overline{\sigma}$ remains constant whereas the pressures vary from $(P_1 + P_2)$ to $(P_1 + dP_1 + P_2 + dP_2)$. Betty's reciprocity theorem will be written as:

$$\left(\frac{\partial V_p}{\partial \overline{\sigma}}\right) d\overline{\sigma} \times (dP_1 + dP_2) = \left[\frac{\partial V}{\partial (dP_1 + dP_2)}\right] d(dP_1 + dP_2) \times d\overline{\sigma} \tag{A.18}$$

Also Equation (A.18) may be written:

$$\frac{\partial P_1 + \partial P_2}{\partial V} = \frac{\partial \overline{\sigma}}{\partial V_p} \tag{A.19}$$

Taking account of Equation (A.10), the left side of above equation can be expressed as:

$$\frac{\partial P_1}{\partial V} + \frac{\partial P_2}{\partial V} = \frac{1}{V\left(\frac{1}{K_t} - \frac{1}{K_s}\right)} + \frac{1}{V\left(\frac{1}{K_t} - \frac{1}{K_n s}\right)} = \frac{K_t}{V}\left(\frac{1}{\alpha_1} + \frac{1}{\alpha_2}\right) \tag{A.20}$$

The right side of Equation (A.19), therefore, can be written as:

$$\frac{\partial V_p}{\partial \overline{\sigma}} = \frac{V}{K_t} \frac{\alpha_1 \alpha_2}{\alpha_1 + \alpha_2} \tag{A.21}$$

The final expression of the relative variation of total pore volume, Equation (A.17), will be in the following form:

$$\frac{dV_p}{V_p} = -\left(\frac{dP_1}{K_s} + \frac{dP_2}{K_n s}\right) + \frac{1}{\phi}\left(\frac{1}{K_t} \frac{\alpha_1 \alpha_2}{\alpha_1 + \alpha_2}\right)(d\overline{\sigma} + dP_1 + dP_2) \tag{A.22}$$

A.3.3 Pore Volume Change Due to Deviatoric Stresses

The same reasoning with the deviatoric components of Equation (A.11) leads to the expression:

$$\frac{dV_p}{V_p} = \frac{1}{\phi}\left(\frac{1}{K_t}\frac{\alpha_1\alpha_2}{\alpha_1+\alpha_2}\right)(d\sigma_{ij}\delta_{ij} - d\overline{\sigma}) = 0 \tag{A.23}$$

From the above derivation, it is clear that the total pore volume variations are caused by mean stresses and pressures, not by deviatoric stresses. Equation (A.22) remains valid in the general case for the pore volume change.

A.4 Variation in Solid Volume

The relative solid volume change can be expressed as:

$$\frac{dV_s}{V_s} = \frac{d(V-V_p)}{V-V_p} = \frac{dV}{V-V_p} - \frac{dV_p}{V-V_p} = \frac{1}{1-\phi}\frac{dV}{V} - \frac{\phi}{1-\phi}\frac{dV_p}{V_p} \tag{A.24}$$

Substituting Equations (A.10) and (A.22) into Equation (A.24) leads to:

$$\frac{dV_s}{V_s} = \frac{1}{1-\phi}\frac{\frac{d\sigma_{kk}}{3} + dP_1 + dP_2}{K_t}(1-\alpha_3) - \frac{dP_1}{K_s} - \frac{dP_2}{K_n s} \tag{A.25}$$

where $\alpha_3 = \dfrac{\alpha_1\alpha_2}{\alpha_1+\alpha_2}$.

After considering Equation (A.10), $\dfrac{d\sigma_{kk}}{3} + dP_1 + dP_2 = d\varepsilon_{kk}K_t + \dfrac{K_t dP_1}{K_s} + \dfrac{K_t dP_2}{K_n s}$.

the variation of relative solid density can be written as:

$$\frac{d\rho_s}{\rho_s} = -\frac{dV_s}{V_s} = \frac{1}{1-\phi}\left[\frac{\alpha_3-\phi}{K_s}dP_1 + \frac{\alpha_3-\phi}{K_n s}dP_2 - (1-\alpha_3)\,u_{si,i}\right] \tag{A.26}$$

Appendix B

Terms in Finite Element Matrices

$$\mathbf{K}_l = \int_V \mathbf{B}^T \mathbf{D} \mathbf{B} dV$$

$$\mathbf{L}_{lw} = -\int_V \alpha_l \mathbf{B}^T \mathbf{m} \mathbf{N} \left(S_{lw} + P_{lc} \frac{\partial S_{lw}}{\partial P_{lc}} \right) dV$$

$$\mathbf{L}_{lo} = -\int_V \alpha_l \mathbf{B}^T \mathbf{m} \mathbf{N} \left(1 - S_{lw} - P_{lc} \frac{\partial S_{lw}}{\partial P_{lc}} \right) dV$$

$$\mathbf{L}_{2w} = -\int_V \alpha_2 \mathbf{B}^T \mathbf{m} \mathbf{N} \left(S_{2w} + P_{2c} \frac{\partial S_{2w}}{\partial P_{2c}} \right) dV$$

$$\mathbf{L}_{2o} = -\int_V \alpha_2 \mathbf{B}^T \mathbf{m} \mathbf{N} \left(1 - S_{2w} - P_{2c} \frac{\partial S_{2w}}{\partial P_{2c}} \right) dV$$

$$\mathbf{K}_{lw} = \int_V \mathbf{N}^T (1-\phi_2) \alpha_3 S_{lw} \rho_{lw} \mathbf{m}^T \mathbf{B} dV$$

$$\mathbf{W}_{lw} = -\int_V \nabla \mathbf{N}^T \frac{\mathbf{k}_l k_{rlw}}{\mu_{lw}} \rho_{lw} \nabla \mathbf{N} dV$$

$$\mathbf{E}_w = -\int_V \mathbf{N}^T \frac{\mathbf{k}_l k_{rlw}}{\mu_{lw}} \rho_{lw} \Psi \mathbf{N} dV$$

$$\mathbf{W}_{ll} = \int_V \mathbf{N}^T \phi_l S_{lw} \frac{\rho_{lw}}{K_{lw}} \mathbf{N} dV - \int_V \mathbf{N}^T \phi_l \rho_{lw} \frac{\partial S_{lw}}{\partial P_{lc}} \mathbf{N} dV + \int_V \mathbf{N}^T (1-\phi_2) \times$$

$$\times S_{lw} \rho_{lw} \frac{(\alpha_3 - \phi_1 - \phi_2)}{K_s} \left(S_{lw} + P_{lc} \frac{\partial S_{lw}}{\partial P_{lc}} \right) \mathbf{N} dV -$$

$$- \int_V \mathbf{N}^T \frac{S_{1w}\rho_{1w}\phi_1\phi_2}{S_{1w}K_{1w} + S_{1o}K_{1o}} \left(S_{1w} + P_{1c}\frac{\partial S_{1w}}{\partial P_{1c}} \right) \mathbf{N} dV$$

$$\mathbf{W}_{12} = \int_V \mathbf{N}^T \phi_1 \frac{\partial S_{1w}}{\partial P_{1c}} \rho_{1w}\, \mathbf{N} dV + \int_V \mathbf{N}^T (1-\phi_2) S_{1w}\rho_{1w} \frac{(\alpha_3 - \phi_1 - \phi_2)}{K_s} \times$$

$$\times \left(1 - S_{1w} - P_{1c}\frac{\partial S_{1w}}{\partial P_{1c}} \right) \mathbf{N} dV - \int_V \mathbf{N}^T \frac{S_{1w}\rho_{1w}\phi_1\phi_2}{S_{1w}K_{1w} + S_{1o}K_{1o}} \times$$

$$\times \left(1 - S_{1w} - P_{1c}\frac{\partial S_{1w}}{\partial P_{1c}} \right) \mathbf{N} dV$$

$$\mathbf{W}_{13} = \int_V \mathbf{N}^T (1-\phi_2) S_{1w}\rho_{1w} \frac{(\alpha_3 - \phi_1 - \phi_2)}{K_n s} \left(S_{2w} + P_{2c}\frac{\partial S_{2w}}{\partial P_{2c}} \right) \mathbf{N} dV +$$

$$+ \int_V \mathbf{N}^T \frac{S_{1w}\rho_{1w}(1-\phi_2)\phi_2}{S_{2w}K_{2w} + S_{2o}K_{2o}} \left(S_{2w} + P_{2c}\frac{\partial S_{2w}}{\partial P_{2c}} \right) \mathbf{N} dV$$

$$\mathbf{W}_{14} = \int_V \mathbf{N}^T (1-\phi_2) S_{1w}\rho_{1w} \frac{(\alpha_3 - \phi_1 - \phi_2)}{K_n s} \left(1 - S_{2w} - P_{2c}\frac{\partial S_{2w}}{\partial P_{2c}} \right) \mathbf{N} dV +$$

$$+ \int_V \mathbf{N}^T \frac{S_{1w}\rho_{1w}(1-\phi_2)\phi_2}{S_{2w}K_{2w} + S_{2o}K_{2o}} \left(1 - S_{2w} - P_{2c}\frac{\partial S_{2w}}{\partial P_{2c}} \right) \mathbf{N} dV$$

$$\mathbf{K}_{1o} = \int_V \mathbf{N}^T (1-\phi_2) \alpha_3 \left(1 - S_{1w}\right) \rho_{1o} \mathbf{m}^T \mathbf{B} dV$$

$$\mathbf{W}_{1o} = - \int_V \nabla \mathbf{N}^T \frac{\mathbf{k}_1 k_{r1o}}{\mu_{1o}} \rho_{1o} \nabla \mathbf{N} dV$$

$$\mathbf{E}_o = - \int_V \mathbf{N}^T \frac{\mathbf{k}_1 k_{r1o}}{\mu_{1o}} \rho_{1o} \Psi \mathbf{N} dV$$

$$\mathbf{W}_{21} = \int_V \mathbf{N}^T \phi_1 \frac{\partial S_{1w}}{\partial P_{1c}} \rho_{1o}\, \mathbf{N} dV + \int_V \mathbf{N}^T (1-\phi_2) S_{1o}\rho_{1o} \frac{(\alpha_3 - \phi_1 - \phi_2)}{K_s} \times$$

$$\times \left(S_{1w} + P_{1c}\frac{\partial S_{1w}}{\partial P_{1c}} \right) \mathbf{N} dV - \int_V \mathbf{N}^T \frac{S_{1o}\rho_{1o}\phi_1\phi_2}{S_{1w}K_{1w} + S_{1o}K_{1o}} \times$$

$$\times \left(S_{1w} + P_{1c}\frac{\partial S_{1w}}{\partial P_{1c}} \right) \mathbf{N} dV$$

$$\mathbf{W}_{22} = \int_V \mathbf{N}^T \phi_1 S_{1o} \frac{\rho_{1o}}{K_{1o}} \mathbf{N} dV - \int_V \mathbf{N}^T \phi_1 \frac{\partial S_{1w}}{\partial P_{1c}} \rho_{1o} \mathbf{N} dV + \int_V \mathbf{N}^T (1-\phi_2) \times$$

$$\times S_{1o} \rho_{1o} \frac{(\alpha_3 - \phi_1 - \phi_2)}{K_s} \left(1 - S_{1w} - P_{1c} \frac{\partial S_{1w}}{\partial P_{1c}}\right) \mathbf{N} dV -$$

$$- \int_V \mathbf{N}^T \frac{S_{1o} \rho_{1o} \phi_1 \phi_2}{S_{1w} K_{1w} + S_{1o} K_{1o}} \left(1 - S_{1w} - P_{1c} \frac{\partial S_{1w}}{\partial P_{1c}}\right) \mathbf{N} dV$$

$$\mathbf{W}_{23} = \int_V \mathbf{N}^T (1-\phi_2) S_{1o} \rho_{1o} \frac{(\alpha_3 - \phi_1 - \phi_2)}{K_n s} \left(S_{2w} + P_{2c} \frac{\partial S_{2w}}{\partial P_{2c}}\right) \mathbf{N} dV +$$

$$+ \int_V \mathbf{N}^T \frac{S_{1o} \rho_{1o} (1-\phi_2) \phi_2}{S_{2w} K_{2w} + S_{2o} K_{2o}} \left(S_{2w} + P_{2c} \frac{\partial S_{2w}}{\partial P_{2c}}\right) \mathbf{N} dV$$

$$\mathbf{W}_{24} = \int_V \mathbf{N}^T (1-\phi_2) S_{1o} \rho_{1o} \frac{(\alpha_3 - \phi_1 - \phi_2)}{K_n s} \left(1 - S_{2w} - P_{2c} \frac{\partial S_{2w}}{\partial P_{2c}}\right) \mathbf{N} dV +$$

$$+ \int_V \mathbf{N}^T \frac{S_{1o} \rho_{1o} (1-\phi_2) \phi_2}{S_{2w} K_{2w} + S_{2o} K_{2o}} \left(1 - S_{2w} - P_{2c} \frac{\partial S_{2w}}{\partial P_{2c}}\right) \mathbf{N} dV$$

$$\mathbf{K}_{2w} = \int_V \mathbf{N}^T (1-\phi_1) \alpha_3 S_{2w} \rho_{2w} \mathbf{m}^T \mathbf{B} dV$$

$$\mathbf{W}_{2w} = - \int_V \nabla \mathbf{N}^T \frac{\mathbf{k}_2 k_{r2w}}{\mu_{2w}} \rho_{2w} \nabla \mathbf{N} dV$$

$$\mathbf{W}_{31} = \int_V \mathbf{N}^T (1-\phi_1) S_{2w} \rho_{2w} \frac{(\alpha_3 - \phi_1 - \phi_2)}{K_s} \left(S_{1w} + P_{1c} \frac{\partial S_{1w}}{\partial P_{1c}}\right) \mathbf{N} dV +$$

$$+ \int_V \mathbf{N}^T \frac{S_{2w} \rho_{2w} (1-\phi_1) \phi_1}{S_{1w} K_{1w} + S_{1o} K_{1o}} \left(S_{1w} + P_{1c} \frac{\partial S_{1w}}{\partial P_{1c}}\right) \mathbf{N} dV$$

$$\mathbf{W}_{32} = \int_V \mathbf{N}^T (1-\phi_1) S_{2w} \rho_{2w} \frac{(\alpha_3 - \phi_1 - \phi_2)}{K_s} \left(1 - S_{1w} - P_{1c} \frac{\partial S_{1w}}{\partial P_{1c}}\right) \mathbf{N} dV +$$

$$+ \int_V \mathbf{N}^T \frac{S_{2w} \rho_{2w} (1-\phi_1) \phi_1}{S_{1w} K_{1w} + S_{1o} K_{1o}} \left(1 - S_{1w} - P_{1c} \frac{\partial S_{1w}}{\partial P_{1c}}\right) \mathbf{N} dV$$

$$\mathbf{W}_{33} = \int_V \mathbf{N}^T \phi_2 S_{2w} \frac{\rho_{2w}}{K_{2w}} \mathbf{N} dV - \int_V \mathbf{N}^T \phi_2 \frac{\partial S_{2w}}{\partial P_{2c}} \rho_{2w} \mathbf{N} dV + \int_V \mathbf{N}^T (1-\phi_1) \times$$

$$\times S_{2w}\rho_{2w}\frac{(\alpha_3-\phi_1-\phi_2)}{K_n s}\left(S_{2w}+P_{2c}\frac{\partial S_{2w}}{\partial P_{2c}}\right)\mathbf{N}dV-$$

$$-\int_V \mathbf{N}^T\frac{S_{2w}\rho_{2w}\phi_1\phi_2}{S_{2w}K_{2w}+S_{2o}K_{2o}}\left(S_{2w}+P_{2c}\frac{\partial S_{2w}}{\partial P_{2c}}\right)\mathbf{N}dV$$

$$\mathbf{W}_{34}=\int_V \mathbf{N}^T\phi_2\frac{\partial S_{2w}}{\partial P_{2c}}\rho_{2w}\ \mathbf{N}dV+\int_V \mathbf{N}^T(1-\phi_1)S_{2w}\rho_{2w}\frac{(\alpha_3-\phi_1-\phi_2)}{K_n s}\times$$

$$\left(1-S_{2w}-P_{2c}\frac{\partial S_{2w}}{\partial P_{2c}}\right)\mathbf{N}dV-\int_V \mathbf{N}^T\frac{S_{2w}\rho_{2w}\phi_1\phi_2}{S_{2w}K_{2w}+S_{2o}K_{2o}}\times$$

$$\times\left(1-S_{2w}-P_{2c}\frac{\partial S_{2w}}{\partial P_{2c}}\right)\mathbf{N}dV$$

$$\mathbf{K}_{2o}=\int_V \mathbf{N}^T(1-\phi_1)\alpha_3 S_{2o}\rho_{2o}\mathbf{m}^T\mathbf{B}dV$$

$$\mathbf{W}_{2o}=-\int_V \nabla\mathbf{N}^T\frac{\mathbf{k}_2 k_{r2o}}{\mu_{2o}}\rho_{2o}\nabla\mathbf{N}dV$$

$$\mathbf{W}_{41}=\int_V \mathbf{N}^T(1-\phi_1)S_{2o}\rho_{2o}\frac{(\alpha_3-\phi_1-\phi_2)}{K_s}\left(S_{1w}+P_{1c}\frac{\partial S_{1w}}{\partial P_{1c}}\right)\mathbf{N}dV+$$

$$+\int_V \mathbf{N}^T\frac{S_{2o}\rho_{2o}(1-\phi_1)\phi_1}{S_{1w}K_{1w}+S_{1o}K_{1o}}\left(S_{1w}+P_{1c}\frac{\partial S_{1w}}{\partial P_{1c}}\right)\mathbf{N}dV$$

$$\mathbf{W}_{42}=\int_V \mathbf{N}^T(1-\phi_1)S_{2o}\rho_{2o}\frac{(\alpha_3-\phi_1-\phi_2)}{K_s}\left(1-S_{1w}-P_{1c}\frac{\partial S_{1w}}{\partial P_{1c}}\right)\mathbf{N}dV+$$

$$+\int_V \mathbf{N}^T\frac{S_{2o}\rho_{2o}(1-\phi_1)\phi_1}{S_{1w}K_{1w}+S_{1o}K_{1o}}\left(1-S_{1w}-P_{1c}\frac{\partial S_{1w}}{\partial P_{1c}}\right)\mathbf{N}dV$$

$$\mathbf{W}_{43}=\int_V \mathbf{N}^T\phi_2\frac{\partial S_{2w}}{\partial P_{2c}}\rho_{2o}\ \mathbf{N}dV+\int_V \mathbf{N}^T(1-\phi_1)S_{2o}\rho_{2o}\frac{(\alpha_3-\phi_1-\phi_2)}{K_n s}\times$$

$$\left(S_{2w}+P_{2c}\frac{\partial S_{2w}}{\partial P_{2c}}\right)\mathbf{N}dV-\int_V \mathbf{N}^T\frac{S_{2o}\rho_{2o}\phi_1\phi_2}{S_{2w}K_{2w}+S_{2o}K_{2o}}\times$$

$$\times\left(S_{2w}+P_{2c}\frac{\partial S_{2w}}{\partial P_{2c}}\right)\mathbf{N}dV$$

$$\mathbf{W}_{44} = \int_V \mathbf{N}^T \phi_2 S_{2o} \frac{\rho_{2o}}{K_{2o}} \mathbf{N} dV - \int_V \mathbf{N}^T \phi_2 \frac{\partial S_{2w}}{\partial P_{2c}} \rho_{2o} \mathbf{N} dV + \int_V \mathbf{N}^T (1-\phi_1) \times$$

$$\times S_{2o} \rho_{2o} \frac{(\alpha_3 - \phi_1 - \phi_2)}{K_n s} \left(1 - S_{2w} - P_{2c} \frac{\partial S_{2w}}{\partial P_{2c}}\right) \mathbf{N} dV -$$

$$- \int_V \mathbf{N}^T \frac{S_{2o} \rho_{2o} \phi_1 \phi_2}{S_{2w} K_{2w} + S_{2o} K_{2o}} \left(1 - S_{2w} - P_{2c} \frac{\partial S_{2w}}{\partial P_{2c}}\right) \mathbf{N} dV$$

IMAGE EVALUATION
TEST TARGET (QA-3)

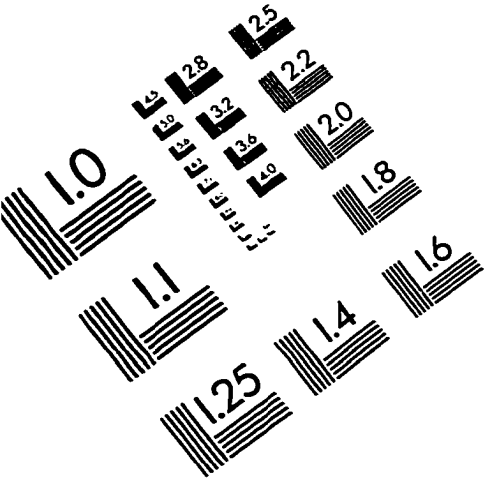

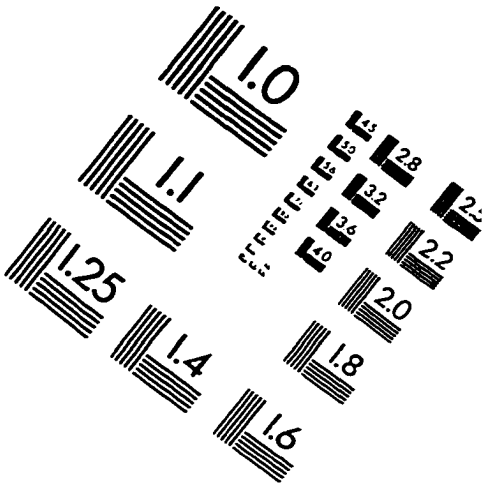

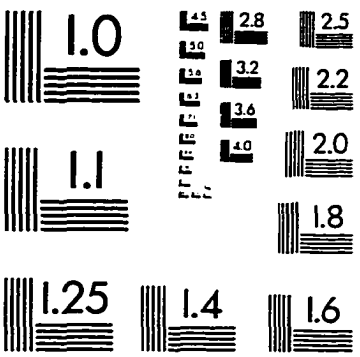

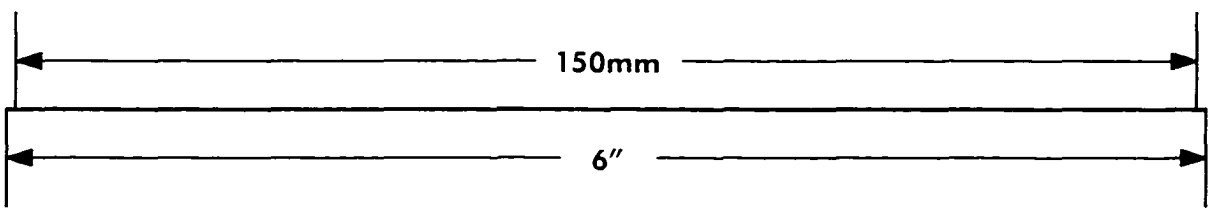

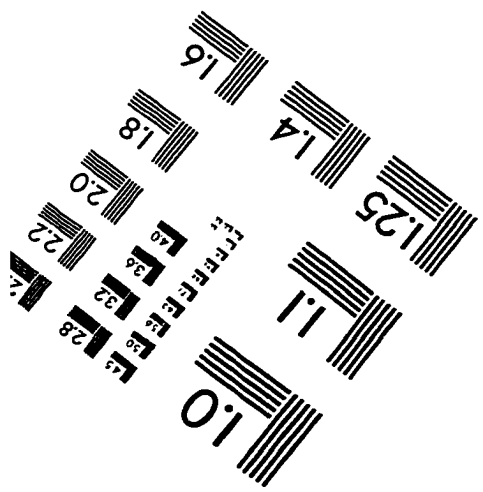

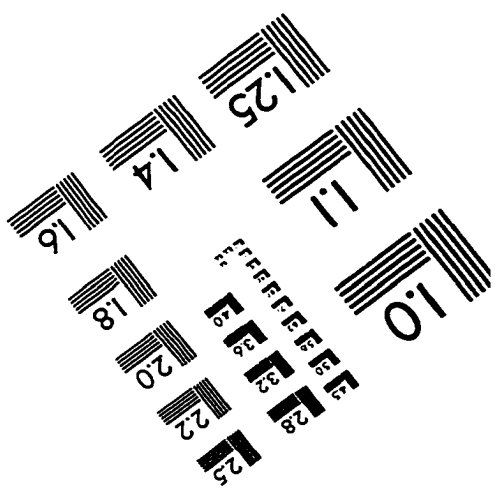

APPLIED IMAGE, Inc
1653 East Main Street
Rochester, NY 14609 USA
Phone: 716/482-0300
Fax: 716/288-5989